NANOCOMPOSITE MEMBRANES FOR COMPLEX SEPARATIONS

A Dissertation

by

SEUNG UK YEU

Submitted to the Office of Graduate Studies of
Texas A&M University
in partial fulfillment of the requirements for the degree of

DOCTOR OF PHILOSOPHY

August 2009

Major Subject: Chemical Engineering

NANOCOMPOSITE MEMBRANES FOR COMPLEX SEPARATIONS

A Dissertation

by

SEUNG UK YEU

Submitted to the Office of Graduate Studies of
Texas A&M University
in partial fulfillment of the requirements for the degree of

DOCTOR OF PHILOSOPHY

Approved by:

Chair of Committee,	Daniel F. Shantz
Committee Members,	Zivko Nikolov
	Hae-Kwon Jeong
	Tahir Cagin
Head of Department,	Michael Pishko

August 2009

Major Subject: Chemical Engineering

ABSTRACT

Nanocomposite Membranes for Complex Separations. (August 2009)

Seung Uk Yeu, B.S., Seoul National University;

M.S., Seoul National University

Chair of Advisory Committee: Dr. Daniel F. Shantz

Over the past few decades there has been great interest in exploring alternatives to conventional separation methods due to their high cost and energy requirements. Membranes offer a potentially attractive alternative as they potentially address both of these points. The overarching theme of this dissertation is to design nanocomposite membranes for processes where existing separation schemes are inadequate. This dissertation focuses on three challenges: 1) designing organic-inorganic hybrid membranes for reverse-selective removal of alkanes from light gases, 2) defect-free inorganic nanocomposite membranes that have uniform pores, and 3) nanocomposite membranes for minimizing protein fouling in microfiltration applications.

Reverse-selective gas separations that preferentially permeate larger/heavier molecular species based on their greater solubility have attracted considerable recent attention due to both economic and environmental concerns. In this study, dendrimer-ceramic hybrid membranes showed exceptionally high propane/nitrogen selectivities. This result was ascribed to the presence of stable residual solvent that affects the solubility of hydrocarbon species.

Mesoporous silica-ceramic nanocomposite membranes have been fabricated to provide defectless mesoporous membranes. As mesoporous silica is iteratively synthesized in the ceramic macropores, the coating method and the surfactant removal step significantly affected permeance and selectivity. It was also shown that support layers can cause a lower selectivity than Knudsen limit.

Membrane fouling which results from deposition and nonspecific adsorption of proteins on the membrane surface is irreversible in nature, and results in a significant decrease in the membrane performance. To address this problem, two approaches were explored: 1) control of the surface chemistry tethering alumina membranes with organic components and 2) development of a novel photocatalytic membrane that exhibits hydrophilicity and can be easily regenerated. Both approaches can offer a viable route to the synthesis of attractive membranes, in that 1) the density of protein-resistant organic groups such as PEG is controllable by changing scaffolds or synthesis conditions and 2) the photocatalytic nanocomposite membranes can open the way for a new regeneration method that is environmentally benign.

ACKNOWLEDGEMENTS

I am a very lucky person because I have many good people around me. Indeed, I could not have accomplished my doctoral study without their help and support. So, I cannot finish this dissertation without acknowledging their help and effort.

First of all, I would like to express my deepest regard and appreciation to my advisor, Dr. Shantz, for his inspiring and encouraging way of guiding me to a deeper understanding of knowledge. I also owe my academic achievements to my committee members: Dr. Nikolov, Dr. Jeong, and Dr. Cagin. Their valuable comments and suggestions have been dissolved in this dissertation to make better scientific work. I cannot forget the discussions with Dr. Ford and Dr. Simanek, by which I could take one more step forward.

I am deeply grateful to my colleagues. I thank Dr. Yoo, Jon, Tahmina, and Heydi for a fruitful collaboration on our work. It was a wonderful experience working with them. I also thank my colleagues in the Shantz group and all my friends here.

My last acknowledgement is saved for my family. How can I ever express my love and thanks to my wife, Jung, and our lovely kids, Tai-yoon and Taimin, for their support and love? Without them, it could be 'the long and winding road'. I also give thanks to my beloved family in Korea. They are my parents, my brother and sister, Jung's parents, and all other family members. Especially, I would like to express my deepest appreciation to my father and mother for their infinite love and support for me. I dedicate this dissertation to all my family.

TABLE OF CONTENTS

CHAPTER Page

LIST OF FIGURES

FIGURE Page

FIGURE Page

FIGURE Page

LIST OF TABLES

CHAPTER I

INTRODUCTION

1.1 Overview

Membrane-based separations are emerging as a viable technology in a wide variety of industrial applications from petrochemical to pharmaceutical since membrane processes generally have low capital investment, low energy consumption and potential ease of operation [1, 2]. Membrane processes typically involve transport of components from an upstream (feed) to a downstream (filtrate, permeate), which is caused by diverse driving forces such as pressure, temperature, concentration, or electric potential. Among them, pressure difference is used as a driving force source in many membrane types such as microfiltration (size range of entities: 100 - 20,000 nm), ultrafiltration (1 - 10 nm), and gas separations (0.2 - 0.5 nm) [3]. While microfiltration is generally used for sterilization of pharmaceutical and medical products [4, 5], ultrafiltration is used to concentrate macromolecules such as proteins [4, 6], and gas separation membranes are used commercially in applications including hydrogen recovery, enrichment of refinery gas, and olefin/paraffin separations [7].

Despite the strong potential of membrane processes, there are still several hurdles to overcome such as development of high-efficiency modules and creation of advanced

---

This dissertation follows the style and format of the Journal of Membrane Science.

materials with tunable capabilities to enhance separation efficiency [3]. To date, several studies focused on finding satisfactory membrane materials from polymers to inorganic materials such as glasses, zeolites and ceramics [3, 8-12]. Polymers in general can offer processability and flexibility while lacking rigidity to ensure high free volume. On the contrary, inorganic materials tend to be brittle and it is difficult to control their surface properties. For this reason, hybrid or composite materials are potentially attractive to overcome limitations of any specific material. However, less work has been performed on hybrid membranes with the notable exception of a few hybrids containing thin film zeolite or fumed silica dispersed phases in polymer matrix [3, 9, 13]. Thus, more exploration of composite materials is necessary to meet the demanding requirements of membrane performance.

The overarching theme of this dissertation is to design nanocomposite membranes for processes where existing materials are inadequate. My dissertation focused on two problems: 1) organic-inorganic hybrid membranes for reverse-selective separation of heavy hydrocarbons from light gases, and 2) designing nanocomposite membranes for minimizing protein fouling in microfiltration. These problems, while seemingly different, were approached in a similar way. The main underlying theme is that by judiciously modifying the ceramic membrane surface with organic groups superior materials are obtained.

1.2 Gas Separation

Application of membranes for gas separation is one of the techniques that is expected to replace conventional separation methods [7], and membranes have found a few commercial applications in gas separations (e.g. hydrogen purification) [8, 14]. Since traditional separation methods such as distillation and/or absorption are highly energy-intensive, membrane-based separation processes are attractive on the basis of their inherent advantages such as low energy requirement and operating cost [7].

1.2.1 Gas Transport Mechanism

Gases can transport through membranes via diverse mechanisms depending on the properties of the gas (viscosity, molecular weight, compressibility, and solubility etc.) and membrane (pore size and its distribution, porosity, and surface property etc.).

The permeability, the inherent ability of membrane for gas transport, is defined from Darcy's law at steady state [2, 7]:

$$\mathrm{P} = \frac{J}{\left(\frac{\Delta p}{l}\right)} \tag{1-1}$$

where J is the gas flux through the membrane, Δp is the transmembrane pressure drop, and l is the thickness of the membrane. The 'Barrer' (1 Barrer = 10^{-10} cm^3 (STP)·cm/(cm^2·s·cmHg)) is often used as the unit of gas permeability for convenience. Along with the permeability, the permeance is also conveniently used to express the

membrane performance when the thickness of the active layer of membrane is not accurately known:

$$P = \frac{\mathrm{P}}{l} = \frac{J}{\Delta p} \tag{1-2}$$

Transport of gases through porous membranes is known to occur by Poiseuille flow (viscous flow), Knudsen flow, surface diffusion, or capillary condensation. The occurrence of Poiseuille flow or Knudsen flow is generally determined by the pore size because the transport mechanism depends on whether molecule-molecule or wall-molecules collisions occur more frequently. The mean free path of the gas molecules, as given by λ in Eq. (1-3), can be compared to the pore radius as a guideline to predict which flow mechanism should be dominant [15]:

$$\lambda = \frac{3\eta}{2p}\sqrt{\frac{\pi RT}{2M}} \tag{1-3}$$

where η is the gas viscosity, p is the pressure, R is the universal gas constant (8.314 J mol^{-1} K^{-1}), T is the temperature, and M is the molecular weight of a gas. For membranes with pores large enough that the mean free path is much smaller than the pore radius, gas molecules will collide with each other more frequently than with the pore walls. In this case, the flow is governed by Poiseuille behavior [2, 16]:

$$J_v = \left(\frac{\varepsilon}{\tau}\right)\frac{r^2(p_0^2 - p_l^2)}{8\eta l RT} \tag{1-4}$$

where J_v is the flux, ε is the membrane porosity, τ is the pore tortuosity that is assumed as unity in parallel and uniform capillaries, r is the pore radius, p_0 is the pressure of the

feed side, and p_l is the pressure of the permeate side. If the pressure of the feed side is much higher than that of the permeate side, $p_0^2 - p_l^2 \approx \Delta p^2$. Then from Eq. (1-1) and (1-4), the permeability can be given as:

$$P_v = \left(\frac{\varepsilon}{\tau}\right)\frac{r^2 \Delta p}{8\eta RT} \tag{1-5}$$

When the pores are small compared to the mean free path, most of the collisions will be made between the gas molecules and the pore walls. This flow mode is called Knudsen diffusion, and the flux and the permeability of this regime are given by [2, 15]:

$$J_K = \frac{2r}{3}\left(\frac{\varepsilon}{\tau}\right)\sqrt{\frac{8RT}{\pi M}}\,\frac{\Delta p}{lRT} \tag{1-6}$$

$$P_K = \frac{2r}{3}\left(\frac{\varepsilon}{\tau}\right)\sqrt{\frac{8}{\pi MRT}} \tag{1-7}$$

Fig. 1-1 [15] shows the change of the permeability from Knudsen flow to Poiseuille flow with an increase of ratio of the pore radius to the mean free path of gas molecules. Typically membranes with pore sizes of hundreds of nanometers ($r/\lambda > 5$) have strong characteristics of Poiseuille flow whereas Knudsen flow is observed in the membranes with pore sizes less than tens of nanometers ($r/\lambda < 0.5$). For this reason, the slope of the permeability (or permeance) as a function of pressure is often regarded as an evidence of the presence of defects in mesoporous membranes, as Poiseuille flow shows a pressure dependence while Knudsen flow is independent of pressure as given in Eq. (1-5) and (1-7).

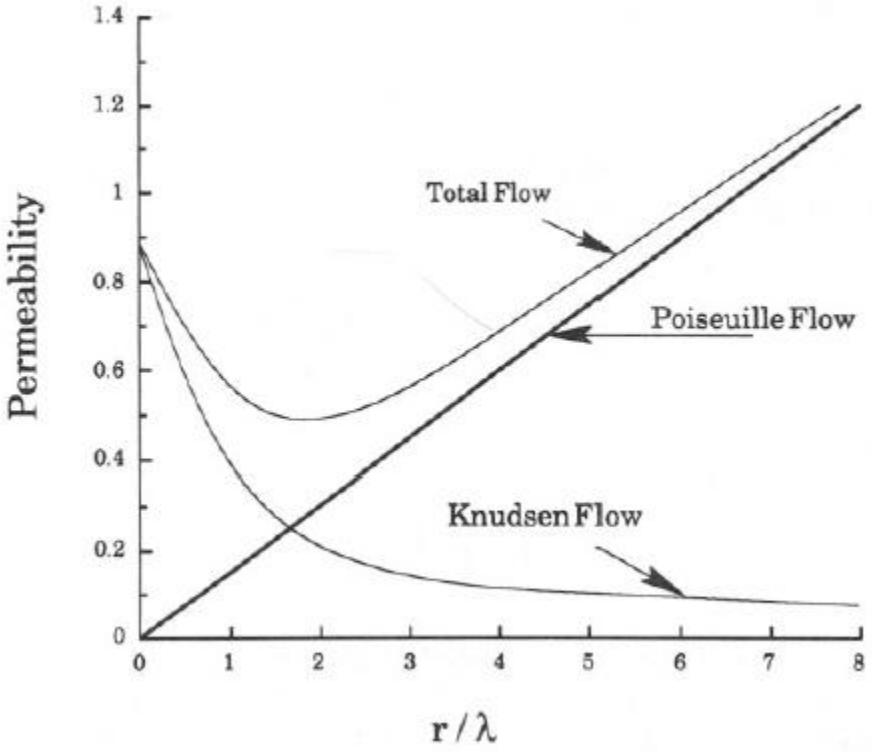

Fig. 1-1. Contributions of Poiseuille flow and Knudsen flow to total flow as a function of the ratio of the pore radius to the mean free path of gas molecules [15].

Surface diffusion can occur when the gas molecules have a strong affinity for the membrane surface so that they adsorb to the pore walls. The driving force in this mechanism is the surface concentration gradient along the pore walls. The flux of the adsorbed molecules may be described by Fick's law [17]:

$$J_s = -\mu D_s \frac{dq}{dz} \tag{1-8}$$

where μ is a geometric coefficient and related with porosity and tortuosity, D_s is the Fickian surface diffusivity, q is the surface concentration of adsorbed molecules, and z is the distance. If the Fickian surface diffusivity is constant, the permeability may be given as:

$$\mathrm{P}_s = \mu D_s \frac{dq}{dp} \tag{1-9}$$

where p is the pressure and the term dq/dp can be obtained from the adsorption isotherm. The actual mechanism, however, is rather complicated because the Fickian surface diffusivity in general is not constant with the surface concentration of adsorbed molecules due to the interactions between the adsorbates. The general expression of the Fickian surface diffusivity can be given by Darken's equation, which is derived from the assumption that the chemical potential gradient is the driving force for transport of the adsorbed gases [18]:

$$D_s = D_c \Gamma = D_c \frac{\partial \ln p}{\partial \ln q} \tag{1-10}$$

where D_s is the Fickian surface diffusivity, D_c is the corrected diffusivity, and Γ is the thermodynamic factor. It has been observed experimentally that the corrected diffusivity is generally independent of the surface concentration with some exceptions [19]. The sorption of non-condensable gases such as nitrogen may follow Henry's regime at low pressures [20]:

$$q = K_H p \tag{1-11}$$

where K_H is the Henry constant. From Eq. (1-8), (1-10), and (1-11), J_s can be calculated as:

$$J_s = \frac{\mu D_c K_H}{l} \Delta p \tag{1-12}$$

Thus, the permeability by surface diffusion in Henry's regime is given as:

$$\mathrm{P}_s = \mu D_c K_H \tag{1-13}$$

If the sorption of gas is well described by a Langmuir isotherm, the surface concentration and the flux may be expressed as [20, 21]:

$$q = \frac{q_s K_L p}{1 + K_L p} \tag{1-14}$$

$$J_s = \frac{\mu q_s D_c}{l} \ln\left(\frac{1 + K_L p_0}{1 + K_L p_l}\right) \tag{1-15}$$

where q_s is the saturated surface concentration, K_L is the Langmuir sorption constant, p_0 is the feed pressure, and p_l is the permeate pressure. For mesoporous membranes, the total flux may be the sum of the Knudsen flow and surface diffusion [22].

Capillary condensation is an extreme form of surface flow that may take place during the transport of condensable gases. When the gas pressure exceeds a certain critical point, the pores may be completely filled with the condensed gas, as given by the Kelvin equation:

$$p = p^* \exp(\frac{2\gamma}{r}\frac{M}{RT\rho_l}) \tag{1-16}$$

where p is the equilibrium vapor pressure of a liquid when it is dispersed as droplets of radius r, p^* is the equilibrium vapor pressure over a plane surface, γ is the surface tension of the liquid, ρ_l is the densities of liquid, M is the molecular weight, R is the universal gas constant, and T is the temperature. The driving force of this mechanism is the capillary pressure difference caused by the formation of menisci at pore ends. In theory, capillary condensation can be a route to achieve high selectivity, as the condensed gas will block the pores and prevent the flow of the non-condensable gases.

As the pore size becomes comparable to the molecular size as in microporous zeolite membranes and carbon molecular sieves, a molecule begins feeling the potential field of the wall. Thus diffusion in this mechanism is an activated process and is referred to as gas translational diffusion or activated Knudsen model [19]. When the pore size is almost the same as the molecular size, permeation behavior shows strong

similarities with that based on solid state diffusion, which is called configurational diffusion [21].

The gas transport mechanism through nonporous membrane is different from that of porous membrane. Typically, polymeric membranes fall into this category where the transport of gas is known to follow the solution-diffusion mechanism [23]. This model can be derived from Fick's first law:

$$J = -D\left(\frac{dc}{dz}\right) \tag{1-17}$$

where J is the flux, D is the diffusion coefficient, and dc/dz is the concentration gradient of the gas across the membrane. From Eq. (1-1) and Eq. (1-17), the permeability can be given as:

$$\mathrm{P} = \int_0^l \frac{J}{\Delta p}\,dz = \int_{c_i(z=l)}^{c_i(z=0)} \left[\frac{D(c)}{\Delta c}\,dc\right]\left[\frac{\Delta c}{\Delta p}\right] = \overline{D}\cdot\overline{S} \tag{1-18}$$

where $\overline{D}$ is the average diffusion coefficient, and $\overline{S}$ is the average solubility coefficient of the gas species. For rubbery polymers, the sorption of low molecular penetrants is usually very low under moderate pressures. Thus, the concentration of a gas in the membrane may be expressed by Henry's law [15]:

$$c = K_D\,p \tag{1-19}$$

where K_D is the Henry's law solubility coefficient. If the diffusion coefficient is constant, the permeability is given as:

$$\mathrm{P} = DK_D \tag{1-20}$$

For glassy polymers where the solubility of a gas is not constant, the permeability can be described by the dual mode sorption theory [7], in which it is assumed that the sorption of gases occurs according to Henry's law and Langmuir isotherm simultaneously. The permeability in this theory is expressed by:

$$\mathrm{P} = K_D D_D \left(1 + \frac{FK}{1+bp}\right) \tag{1-21}$$

where D_D is the diffusion coefficient in the Henry's law regime, F is the ratio of diffusion coefficients (Langmuir/Henry), and b is the Langmuir affinity constant. Another approach to explain the deviation from an ideal permeability behavior is the free volume theory. This model assumes that the movement of molecules depends on the free volume in polymer and needs energy sufficient to overcome polymer-polymer attractive forces [7]. The flux in the theory is given as [24]:

$$J = -\frac{D}{1-\phi}\frac{d\phi}{dz} \tag{1-22}$$

where ϕ is the local volume fraction of penetrant in the polymeric membrane. The diffusion coefficient here is modeled as [9]:

$$D = A\exp\left(-B\frac{\nu}{V_f}\right) \tag{1-23}$$

where A and B are positive constants, v is the minimum volume required for a penetrant to execute a diffusion step and hence is a measure of penetrant size, and V_f is the average

polymer free volume. The free volume may change by the solubilization of the penetrants in polymer as well as the change of temperature and pressure, which is given by [24]:

$$V_f = V_{fs} + \Delta\alpha(T - T_s) - \Delta\beta(p - p_s) + \gamma\phi \tag{1-24}$$

where V_{fs} is the free volume of pure polymer at standard state, $\Delta\alpha$ is the thermal expansion coefficient, $\Delta\beta$ is the compressibility, γ is the concentration coefficient related with the ability to plasticize polymer, and T_s and p_s are the temperature and the pressure respectively at standard state.

1.2.2 Reverse-Selective Separation

In any membrane separation the selectivity of one component (*A*) over another (*B*), defined as the ratio of permeabilities, contains contributions from both diffusivity and solubility as shown by:

$$\alpha_{A/B} \equiv \frac{\mathrm{P}_A}{\mathrm{P}_B} = \frac{D_A}{D_B} \times \frac{S_A}{S_B} \tag{1-25}$$

In general, a gas that exhibits high diffusivity tends to have low solubility, which makes it difficult to achieve high selectivity. For example, gases with low molecular weight such as helium and nitrogen have very high diffusivity and low solubility, and vice versa for condensable gases such as propane and carbon dioxide. As to membranes, porous membranes such as zeolites typically show the separation ability based on the diffusivity difference of the gases (size sieving effect). In fact, most membrane separations are

currently based on diffusivity differences, which is the concept we usually have for the membrane separation. This diffusivity-based gas separation usually shows a trade-off relationship between the permeability and the selectivity, as shown in Fig. 1-2 [25]. To gain commercially attractive membrane performance, indeed, means overcoming of the Robeson's upper bound. Besides, another challenge with respect to the practical membrane system exists. Hydrogen recovery by membrane separation, for example, may require the recompression of the hydrogen after separation [8, 14]. Competing systems such as cryogenics generally deliver the purified hydrogen at high pressure [7]. However, the hydrogen product (permeate) from the diffusivity-based membrane process is at a pressure lower than that of the feed, which means that hydrogen must be recompressed before it can be reused. Moreover, hydrogen content in the feed can reach up to 80 mol% with C1 – C5 as the balance in some cases such as hydrogen recovery from refinery waste gases, and the volume of hydrogen can even represent 20 – 30% more because of its small molecular weight [26, 27], which potentially makes the membrane system less efficient. This problem cannot be overcome by conventional diffusivity-based separation.

Reverse-selective gas separations (or solubility-based gas separations), which preferentially permeate larger/heavier molecular species based on their greater solubility, have attracted considerable recent attention due to both economic and environmental concerns [28]. This mode is particularly attractive in applications where the heavier species are present in dilute concentrations, such as the removal of volatile compounds (VOCs) from effluent streams [26, 29] or the removal of higher hydrocarbons from

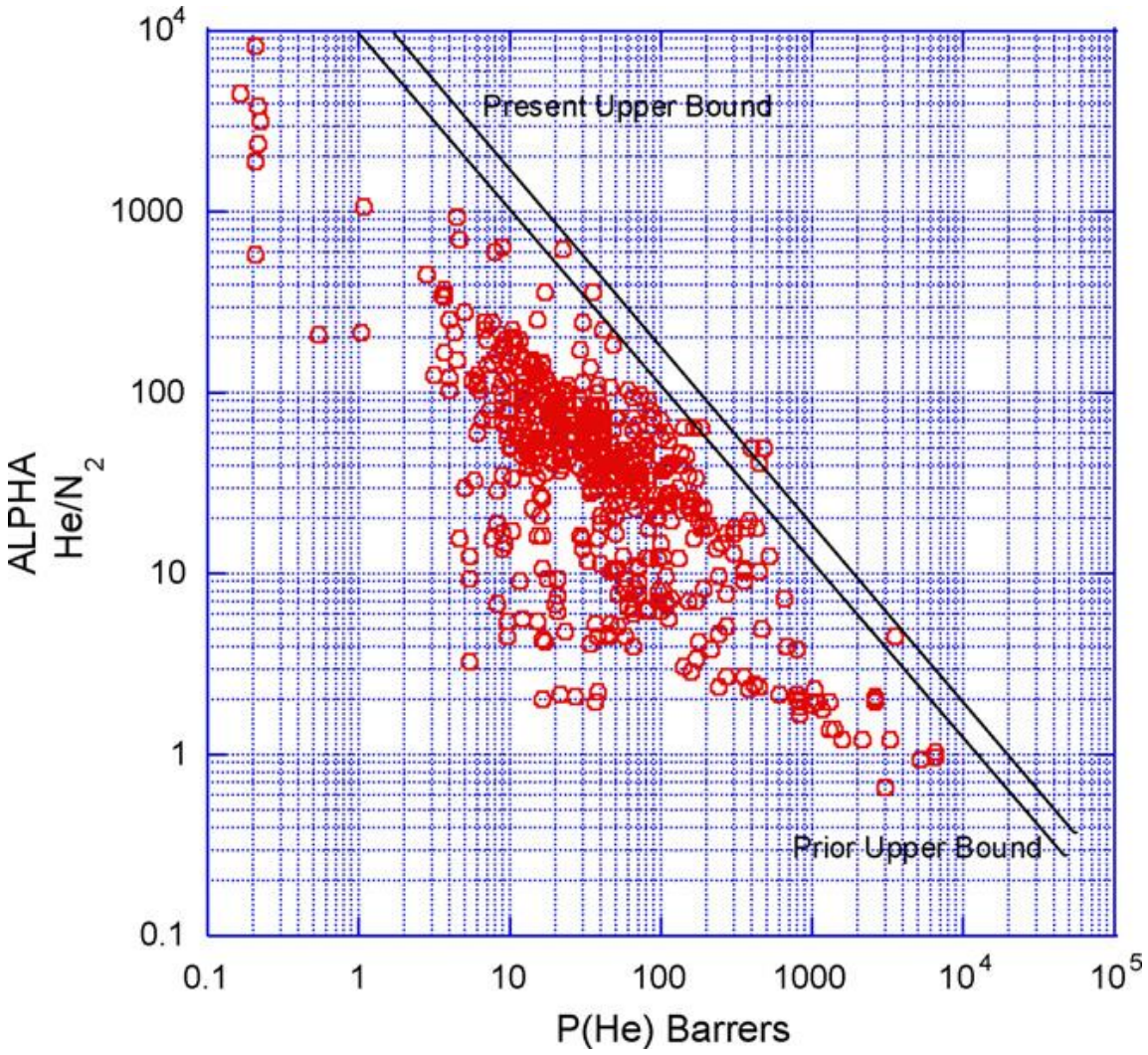

Fig. 1-2. Robeson's plot and upper bound for He/N_2 separation [25].

natural gas or hydrogen [27]. Reverse-selective membranes would have great advantages over diffusivity-based membranes in that they can be designed to permeate the hydrocarbons and leave purified hydrogen on the high pressure (retentate) side, which will significantly reduce the recompression cost and enhance the membrane efficiency.

Freeman and Pinnau [28] point out that to achieve solubility-based separation, the membrane needs not only a high solubility ratio but also a large free volume to drive the diffusivity ratio of the permeating species as close to unity as possible:

$$\alpha_{A/B} = \frac{D_A}{D_B} \times \frac{S_A}{S_B} \approx \frac{S_A}{S_B} \tag{1-26}$$

Such a membrane will be reverse-selective, preferentially permeating the larger and more condensable species than light gases. Solubility-selective materials can enable a positive correlation between permeability and selectivity, which is in contrast to the conventional Robeson trade-off rule [25, 30] that suggests an upper bound in diffusivity-based separations.

Polymeric membranes are commercially dominant in this application mainly due to low cost and ease of fabrication as well as their high solubility-selectivity. Polysulfone, polyimine, polyimide, cellulose acetate, silicone rubber, and polydimethylsiloxane (PDMS) are examples for this category. Polymeric membranes, however, have significant problems not only with plasticization when exposed to adverse conditions such as high pressure and temperature, but also with fouling by highly sorbing components [14]. Moreover, the permeabilities of most of polymeric

membranes are significantly lower as compared to inorganic membranes. Inorganic porous membranes generally exhibit high permeabilities, and even very high selectivities in some cases. However, their transport mechanisms such as surface diffusion and/or capillary condensation are often sensitive to process variables. Thus it is difficult to obtain consistent separation performance from inorganic porous membranes. In these respects, nanocomposites may be a viable route to improved membrane materials for solubility-selective separations.

1.3 Protein Microfiltration

Effectively separating biomacromolecules is essential for modern biotechnology, due in part to the costs of attaining high purity materials [1, 4]. It is widely accepted that protein purification involves three operations: biomacromolecular capture (concentration), separation (fractionation), and polishing [4]. Even though membrane filtration plays an important role in the concentration step, packed-bed chromatography has long dominated purification processes despite several limitations, including high cost, high pressure drop, low throughput and complex scale-up [1, 31]. In recent years, a great deal of attention has been paid to micro/ultrafiltration for protein purification [5, 32-41] because it is expected to ultimately have lower cost, higher throughput, and, for ultrafiltration, size exclusion effects (generally proteins have effective particle sizes between about 2 to 15 nm). However, satisfactory throughput and resolution (or selectivity) have yet to be obtained mainly due to membrane fouling and the broad pore size distribution inherent in many membranes. Three issues are particularly crucial to

the success of membrane filtration. First, protein-membrane interactions significantly affect fouling, resolution, and protein stability [32, 33, 35, 36, 40, 42]. Second, membranes must be chemically and mechanically stable [43]. Third, membranes should possess narrow pore size distributions and the pore size should not change with filtration conditions [43, 44].

1.3.1 Fouling Models

Given the driving force in microfiltration is pressure difference, the membrane hydraulic permeability can be expressed as [32]:

$$L_p = \frac{\mu J}{\Delta p} \tag{1-27}$$

where J is the filtrate flux, μ is the solution viscosity, and Δp is the pressure drop. Since the resistance is defined as the reciprocal of hydraulic permeability, the volumetric flow rate is:

$$Q = JA = \frac{\Delta p}{\mu R_t} A \tag{1-28}$$

where J is the flux of the protein solution through the membrane, A is the surface area of the membrane, and R_t is the total resistance. Although the hydraulic permeability is useful for measuring the initial membrane performance, the flux decline by the fouling during filtration makes it difficult to use this concept for microfiltration evaluation.

Flux behavior during microfiltration has been discussed in many studies [45-48], which generally can be described by four classical fouling models: complete pore blocking, intermediate pore blocking, pore constriction (standard blocking), and cake filtration. The complete pore blocking model ascribes the flux decline to the decrease of the number of open pores or unblocked surface area, which is caused by the deposition of large particles or protein aggregates to the pore entrance. The governing equation of this model assumes that the decreasing rate of unblocked surface area (or the number of open pores) is proportional to the convective flow rate:

$$\frac{dA}{dt} = -\alpha Q C_b \tag{1-29}$$

where A is unblocked surface area, t is the filtration time, α is the pore blockage parameter that may be related to protein aggregates, Q is the volumetric flow rate, and C_b is the bulk concentration of the solution. The normalized flow rate can be calculated from Eq. (1-28) and (1-29):

$$\frac{Q}{Q_0} = \exp\left(-\alpha \frac{\Delta p}{\mu R_m} C_b t \right) \tag{1-30}$$

where Q_0 is the initial volumetric flow rate, and R_m is the resistance of the clean (unfouled) membrane.

In the intermediate pore-blocking model, the superposition of deposited particles is considered on the basis of the complete pore-blocking model. The governing equation and normalized flow rate are given by Eq. (1-31) and (1-32) respectively:

$$\frac{dA}{dt} = -\alpha' Q C_b \frac{A}{A_0} \tag{1-31}$$

$$\frac{Q}{Q_0} = \left(1 + \alpha' \frac{\Delta p}{\mu R_m} C_b t\right)^{-1} \tag{1-32}$$

where α' is the pore blockage parameter of this model, and A_0 is initial (unblocked) surface area of the membrane.

The pore constriction model is often called the standard model. The model assumes that pores are cylindrical and straight, and the flux declines as pore volume decreases due to the deposition of particles on the internal pores:

$$\frac{d(N_0 \pi r_p^2 \delta_m)}{dt} = -\beta Q C_b \tag{1-33}$$

$$\frac{Q}{Q_0} = \left(1 + \beta \frac{Q_0}{\pi r_0^2 \delta_m} C_b t\right)^{-2} \tag{1-34}$$

where N_0 is the number of membrane pores, r_p is the radius of membrane pores, δ_m is the membrane thickness, β is the pore constriction parameter, and r_0 is the initial radius of the membrane pores.

The cake filtration model describes protein cake formation on the front surface of the membrane and assumes that the resistance increases as a cake layer grows:

$$\frac{dR_p}{dt} = f' R' J C_b \tag{1-35}$$

$$\frac{Q}{Q_0} = \left(1 + f' R' \frac{2\Delta p}{\mu R_m^2} C_b t\right)^{-1/2} \tag{1-36}$$

where R_p is the resistance of the cake deposit, f' is the fraction of the proteins that contribute to the growth of the deposit, and R' is the specific protein layer resistance.

Although all of the fouling mechanism above mentioned could contribute to the flux decline during filtration, one or two fouling models may occur primarily depending on the sizes and the fraction of protein aggregates and the membrane properties such as electrostatic charge and hydrophilicity of the membrane surface as well as the sizes, distribution, and morphology of the pores. One of the common methods to determine which fouling mechanism is dominant during filtration is to plot the general governing equation [38, 49]:

$$\frac{d^2 t}{dV^2} = k\left(\frac{dt}{dV}\right)^n \tag{1-37}$$

where V is the total filtered volume, k is the constant, and the exponent n characterizes the fouling model, with $n = 0$ for cake filtration, $n = 1$ for intermediate blocking, $n = 1.5$ for standard blocking, and $n = 2$ for complete pore blocking. The required derivatives can be evaluated in terms of the filtrate flow rate (Q) and the rate of flux decline (K):

$$\frac{dt}{dV} = \frac{1}{Q} \tag{1-38}$$

$$\frac{d^2 t}{dV^2} = \frac{K}{Q^2} \tag{1-39}$$

where the rate of flux decline can be evaluated directly from the filtrate flux data as:

$$K = -\frac{1}{Q}\left(\frac{dQ}{dt}\right) \tag{1-40}$$

This analysis method has the merit of showing if the mechanism of fouling changes with time. However, the analysis often leads to some ambiguity in the value of *n* as compared to theory. Moreover, a quantitative description of the membrane performance is not directly obtained from this method.

An alternate approach is to plot the linear relationship of each model to determine the dominant mechanism. This represents analysis of the problem in terms of limiting cases. In the case where the fouling behavior is dominated by one mechanism, this analysis is straightforward and quite insightful. Table 1-1 shows the relationships for four classical fouling models [47]. This method should be approached carefully since oversimplifying may be misleading and sometimes disregard other fouling mechanisms that are not negligible.

In many cases, indeed, interpretation of fouling is not easy because the fouling behaviors described above may occur simultaneously during filtration. In fact, many studies [38, 46, 50] reported the transition of the fouling mechanism with time. Most of them showed that either a pore blocking or a pore constriction mechanism governs the initial flux decline whereas cake filtration can account for the flux behavior at long times. Thus, two or more fouling mechanisms are often employed to explain the flux data. For example, Tracey and Davis [46] showed that both the complete pore blocking model and the pore constriction model fit the flux data of bovine serum albumin (BSA)

Table 1-1. Linear equations for the various fouling models. Q is the volumetric flow rate, t is the filtration time, and V is the filtrate volume at t.

Model	**Equation**
Complete pore blocking	$\ln\left(\frac{Q_0}{Q}\right) = a_p t + b_p$
Intermediate pore blocking	$\frac{1}{Q} = a_i t + b_i$
Pore constriction (Standard blocking)	$\frac{t}{V} = a_s t + b_s$
Cake filtration	$\frac{t}{V} = a_c V + b_c$

depending on the protein concentration and the pore size of the membranes that were used, which was thought to be due to the presence of protein aggregates. In an effort to explain complicated flux behavior, Ho and Zydney [38] have developed a combined pore blockage and cake filtration model which accounts for the transition of fouling models during microfiltration:

$$\frac{Q}{Q_0} = \exp\left(-\frac{\alpha \Delta p C_b}{\mu R_m} t\right) + \frac{R_m}{R_m + R_p}\left[1 - \exp\left(-\frac{\alpha \Delta p C_b}{\mu R_m} t\right)\right] \tag{1-41}$$

$$R_p = (R_m + R_p)\sqrt{1 + \frac{2 f' R' \Delta p C_b}{\mu (R_m + R_p)^2} t} - R_m \tag{1-42}$$

This combined model showed very good agreement with the results of BSA filtration through 0.2 μm polycarbonate track-etched (PCTE) membranes. More recently a complicated model accounting for internal fouling as well as external fouling and cake filtration has been developed by Duclose-Orsello et al [51]. They suggested that the hydrophilicity of membrane may alter the fouling mechanism during filtration from the study of BSA filtration through 0.22 μm hydrophilic and hydrophobic Durapore membranes.

All the studies given here offer some perspective description of the fouling behavior. However, a simple but comprehensive model has not been developed yet possibly since the fouling behavior is not so simple and differs depending on the properties of proteins and membranes.

1.3.2 Membrane Materials

Proteins can bind to membrane surfaces by a variety of mechanisms including electrostatic attraction, hydrophobic interactions, hydrogen bonding, and van der Waals forces, which in turn result in membrane fouling. Many publications [6, 36, 42] have reported that the electrostatic repulsion between the protein and the membrane results in an increase in selectivity with decreased fouling. Besides electrostatic repulsion, hydrophilicity of the membrane plays a key role in reducing adsorption of proteins [52-54]. Salgin *et al.* [53], for instance, demonstrated by comparing hydrophilic cellulose membranes with hydrophobic polyethersulfone (PES) membranes under various conditions that hydrophobic forces were the determinative factor in protein adsorption on the membrane surfaces. Indeed, fouling is the biggest obstacle to commercialization of membranes because it significantly lowers throughput.

A wide variety of materials have been employed as membranes, from polymeric materials such as poly(vinylidene fluoride) (PVDF), polycarbonate, PES, and cellulose, to inorganic materials such as alumina [5, 32, 38, 42, 55]. However, since most membranes are not hydrophilic, surface modification has been shown to be a promising approach in membrane development [56]. Among the most promising low-protein-adsorbing materials, poly(ethylene glycol) (PEG) has shown extraordinary resistance to non-specific protein adsorption as demonstrated by a number of publications [57-60]. This property has been attributed to the steric repulsion, excluded volume, and hydrophilicity of PEG [61, 62]. Although previous studies have demonstrated the feasibility of performing protein purification using micro/ultrafiltration under certain

conditions, there has been no breakthrough with respect to the membrane itself, in that there has been no membrane that has excellent performance (low fouling and high resolution) as well as good stability. For example, even though cellulose and its derivatives, such as cellulose ester, result in less fouling and have excellent mechanical strength [5], they may swell in water and their pore size changes with temperature and pressure [43]. Moreover, polymeric membranes generally have a broad pore size distribution [55] with a few exceptions such as track-etched polycarbonate. In this respect, inorganic membranes may be an attractive alternative to polymers. The few literature reports of inorganic membranes for protein purification [42, 55, 63-65] have been limited to commercial alumina membranes. These alumina membranes exhibit more rapid fouling as compared to their polymeric counterparts. Thus, it seems one route forward would be to design hybrid membranes wherein the desirable features of both ceramic membranes (high pore size uniformity, resistance to swelling) and organic membranes (potential diversity in surface chemistry) could be retained.

1.4 Melamine-based Dendrimers

The dendritic polymers are a promising class of organic molecules for hybrid membranes due to their wide range of structural and chemical diversity [66, 67]. Dendrimers are a class of hyperbranched polymers that possess a core, repeating branching units (generation) and peripheral groups at the edges [68]. As mentioned in section 1.3.2, high permeabilities and selectivities can be achieved in solubility-based separations if a diffusivity-selectivity is close to unity while a solubility-selectivity is

kept high. Thus, well-defined hyperbranches of dendrimers are very attractive when applied for gas separations, in that they may offer large free volume. Also, the density and chemistry of peripheral groups can be controlled by changing dendrimer generations and functionality when dendrimers are used as a scaffold for further functionalization.

Melamine-based dendrimers have been developed by Dr. Simanek's laboratory [67]. Melamine is a 1,3,5-triazine substituted with three amines, and also known as cyanuramide or triaminotriazine. Melamine-based dendrimers are synthesized by using differential reactivity of triazines as shown in Fig. 1-3 [67]. High generation dendrimers are synthesized by the iterative synthesis of triazine ring and diamine linker molecules. The linker groups with different polarities, hydrophobicities, and rigidities may be employed for the particular applications. The different peripheral functional groups can be attached finally for the specific applications such as surface sorption or chemical reaction.

1.5 Ordered Mesoporous Silica

Porous materials can be categorized into three classes: microporous (< 2 nm), mesoporous (2 – 50 nm), and macroporous materials (> 50 nm) [69]. Since the discovery of MCM-41 by Mobil scientists in 1992 [70], surfactant-templated ordered mesoporous silica (OMS) has attracted much attention because of their potential applications in catalysis, separations, adsorption, and insulator materials [69]. Important features of OMS are : (1) their pore size and pore structure are controllable simply by

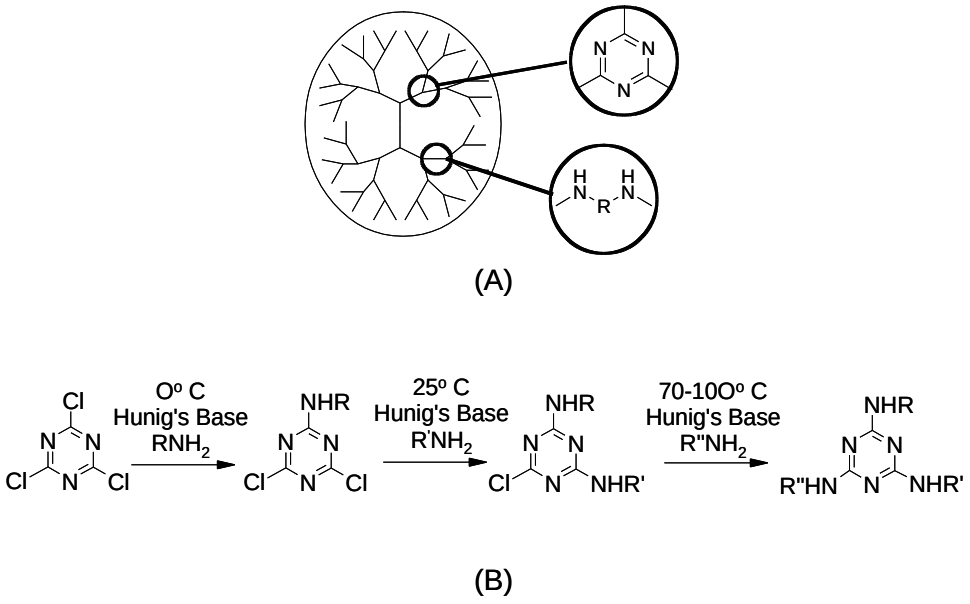

Fig. 1-3. Melamine-based dendrimers. (A) Structural diversity by the interconnection between triazine core and diamine linker. (B) Differential reactivity of triazine.

modifying surfactant concentration or reaction condition such as temperature, (2) their pore size distribution is very narrow, and (3) they can be synthesized as particles or films, which broadens their potential for diverse use.

The structures of OMS can be broadly classified into hexagonal, cubic, and lamella structure, which depends on the amounts and the type of surfactants, reaction temperature, ionic strength, acidity, aging temperature and time. The most common structure of OMS is the two-dimensional hexagonal phase with *P*6*mm* symmetry, consisting of close-packed hexagonal arrays of cylindrical surfactant micelles. This pore structure can be obtained from either cationic surfactants [70] or non-ionic block copolymer surfactants [71]. Various cubic phases have also been reported. For example, bicontinuous cubic gyroid phase with $Ia\bar{3}d$ symmetry can be made using Pluronic P123 (a non-ionic block copolymer) and *n*-butanol at low acid conditions [72]. The variation of phases may be predicted by the surfactant packing parameter [73]:

$$g \equiv \frac{V}{a_0 l_c} \tag{1-43}$$

where V is the effective volume of the hydrophobic chain, a_0 is the mean aggregate surface area per hydrophilic head group, and l_c is the kinetic hydrophobic chain length of a surfactant. The surfactant packing parameters and their expected structures are given as follows: (1) when g < 1/3, spherical micelles are favored, (2) when g = 1/3, cubic (*Pm3n*) phase appears, (3) when g = 1/2, infinite rod-like micelles (hexagonal phase, *P6*) are preferred, (4) when g = 1/2 – 2/3, cubic ($Ia\bar{3}d$) structure favored, and (5) at g = 1, lamellar structure becomes dominant. As the packing parameter increases, the

aggregates curvature becomes low [74]. Since a_0 can be affected by temperature, pH, and the concentration of surfactant and electrolytes, the mesoporous phase is a function of various synthesis parameters.

The formation mechanism of OMS has been studied in a number of works [75, 76]. It is generally accepted that the formation of mesoporous materials occurs in two steps [74]. The initial stage involves preferable adsorption of silicate ions at the micellar interface, which is driven by charge density matching or hydrogen bonding between the surfactant headgroups and silicate ions. As a second stage, two possibilities are proposed: (1) as silicates adsorb, thereby changing the surface energy, the rearrangement of micelles and condensation of silicates sequentially occur into ordered or disordered collapsed phases. This process is often referred to as cooperative self-assembly mechanism [77]. Otherwise, (2) instead of the rearrangement of micelles, aggregation into disordered phase initially occurs due to the reduction of the intermicellar repulsion as silicates adsorb to the surface of micelles, and then may be rearranged into ordered phase [78]. The schematic summary of the proposed formation mechanism of OMS is shown in Fig. 1-4.

Evaporation-induced self-assembly (EISA) [79, 80] is a useful technique for the synthesis of thin mesoporous films. In this method, a coating solution containing the solvent, surfactant and silica precursor is applied on substrates by dip-, spin-coating or film casting, followed by evaporating solvent at the conditions such that form desired OMS. As well as the composition of coating solution, humidity and temperature in the drying step are important factors because ordering and orientation of the OMS phase

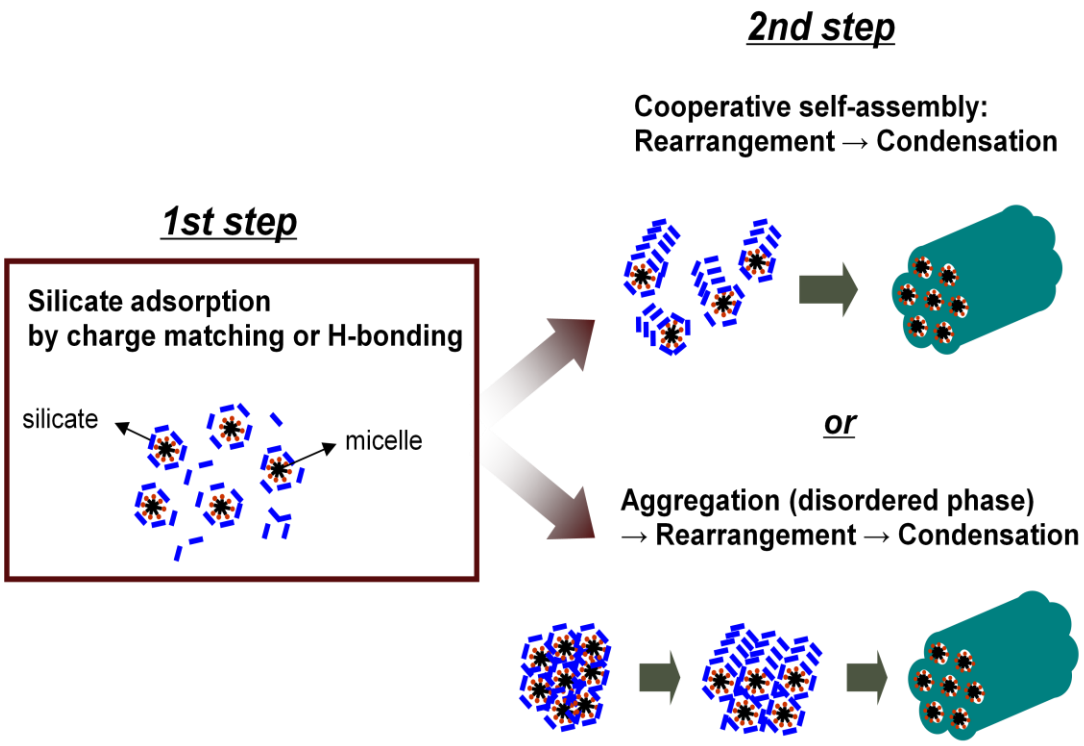

Fig. 1-4. Proposed formation mechanisms of ordered mesoporous silica.

may be significantly altered during condensation [81]. The formation of OMS thin films by EISA on porous substrates recently has been studied in many works [82-84] as a viable route to the synthesis of membranes with uniform pore size and controllable pore structure. This method, however, requires high temperature calcination or solvent extraction to remove surfactants inside the mesopores after forming OMS. These harsh treatments may cause a phase collapse or a pore shrinkage, which, in turn, can result in defect formation in the membranes. For this reason, multiple coatings can be applied to make the defect-free membranes [84].

1.6 Photocatalysis and Superhydrophilicity

Photocatalysts have been extensively studied for many applications including photodecomposition and photoantibacterial treatments for environmental purification, dye-sensitized films for solar cells, chemical sensing, and advanced batteries [85-89]. The photocatalytic activity typically takes place via oxidation by the valence-band holes, which, along with the excited electrons at the conduction band, are generated when the photons with energy matching or exceeding the bandgap energy of photocatalysts are absorbed. These photogenerated electrons and holes may avoid recombination and participate in redox reactions in the presence of available scavengers of electrons and holes. Oxidative hole-transfer is generally accepted to occur via surface-bound hydroxyl radicals, with some reports of direct transfer of the valence-band holes [90].

Titanium dioxide (TiO_2) is one of the most promising photocatalytic materials owing to its long-term stability, nontoxicity, high oxidative capacity, good compatibility

with various substrates [91-93], and the excellent film properties such as controllability of refractive index and high thermal stability [94]. The photocatalytic activity of TiO_2 is known to be strongly dependent on crystallinity and surface properties such as surface hydroxyl density and surface area [92]. As to the effect of crystal structure of TiO_2, anatase phase in general shows much higher photocatalytic activity than rutile form [95].

Another interesting property of TiO_2 is the photogeneration of surface amphiphilicity. Wang *et al.* [96, 97] discovered that the surface of a TiO_2 thin film becomes highly hydrophilic and highly oleophilic simultaneously by ultraviolet (UV) illumination regardless of photocatalytic activity, where the film showed a change in the water and glycerol trioleate contact angles from 72° to 0° and 10° to 0° after UV illumination, respectively. Such highly amphiphilic surfaces were attributed to the nano-scale separation between the hydrophilic and the oleophilic phases due to photogenerated Ti^{3+} defects, which are favorable for dissociative water adsorption. This unique property opened the way to the application of TiO_2 coating in antifogging and self-cleaning systems since under UV illumination both hydrophilic and oleophilic contaminants can be easily removed from TiO_2 surface [97-99].

While many studies on TiO_2 are still focusing on the applications either as a photocatalyst or as a self-cleaning material, a few works have found comprehensive utilization of the properties of TiO_2, that is, both photocatalytic activity and superhydrophilicity. One of these works is to use TiO_2 for the prevention of biofilm formation in which Ciston *et al.* [86] observed a significant reduction of bacterial attachment to a zirconia disc coated with Degussa P25 (80% anatase and 20% rutile)

particles under UV illumination. In the work of Rahimpour *et al.* [100], polyethersulfone ultrafiltration membranes modified with TiO_2 nanoparticles showed much less flux decline with UV irradiation than before modification. This concept has also been extended beyond TiO_2 particles to thin films. Choi *et al.* [101], using a sol-gel dip-coating process, synthesized a TiO_2 membrane with a hierarchical mesoporous multilayer structure for organic photodegradation and observed an anti-fouling effect. Zhang *et al.* [102] synthesized a TiO_2 nanotube membrane in an alumina support, which exhibited good photocatalytic activity on degradation of humic acid with less fouling. Also, Madaeni and Ghaemi [103] dispersed TiO_2 particles (P-25) on polymeric membranes for reverse osmosis application. All of these works have demonstrated that TiO_2 can be effectively used for diverse applications.

CHAPTER II

EXPERIMENTAL PROCEDURE

In this chapter, general information about the materials and the synthesis procedure for the nanocomposite membranes are described. More detailed or additional explanations are given in each chapter.

2.1 Synthesis of Reverse-Selective Nanocomposite Membranes

Dendrimer-ceramic hybrid membranes for gas separations were prepared by synthesizing melamine-based dendrimer in the mesopores of Membralox® membranes. The goal was to obtain composite membranes processing high reverse selectivities (i.e. for the heavy component) by controlling free volume and solubility by changing dendrimer generations and functionalizing the dendrimer surface.

2.1.1 Materials

Ethanol and toluene (ACS reagent grade) were purchased from EM Science. 3-aminopropyldimethyethoxysilane (APDMES, 99%) was purchased from Gelest Inc. Piperazine (P, 99%) and *N*,*N*-diisopropylethylamine (DIPEA, 99%) were purchased from Aldrich. Cyanuric chloride (CC, 99%) was purchased from ACROS. Tetrahydrofuran (THF), methanol, and dichloromethane (DCM) (all ACS reagent grade)

were purchased from EMD. All chemicals were used as received. Water was purified using a Barnstead EASYpure water purification system.

The membranes used in this research were Membralox® T1-70-25G, tubular alumina membranes obtained from Pall Co., DeLand, Florida (Part# S700-01227). This membrane is an asymmetric membrane that consists of an inner mesoporous γ-alumina layer deposited on the inside of a macroporous α-alumina support tube. The mesoporous layer of this membrane is reported to have a distribution of pore sizes between 2 and 5.5 nm, with a maximum near 4 nm, and a thickness of 3 - 5 μm [104]. The macroporous support has an outer diameter of 1.0 cm and an inner diameter of 0.7 cm. The original tube length was 25 cm. Fig. 2-1 shows a scanning electron micrograph (SEM) image of the membrane cross-section [105]. For our experiment, we cut the tubes into 1 in. pieces using a laboratory glass cutter. After cutting, the membranes were cleaned by soaking in 2:1 ethanol/water solution for 24 hours at ambient temperature. The membranes were then dried at 100 °C for at least 4 h, and stored in the laboratory environment until used for the RCA (Radio Corporation of America) treatment and hybrid synthesis. RCA treatment was performed just before amine functionalization using base and acid solutions. A base solution was prepared by mixing 11 ml of NH_4OH (28-30 wt% NH_3), 11 ml of H_2O_2 (30 wt%), and 53 ml of deionized water at room temperature. A membrane was added and this solution was kept in an oil bath at 70 °C for 15 minutes, followed by washing the membrane 5 times with 100 ml of de-ionized water, while gently rocking, for 5 minutes each. The acid rinse was performed using 10 ml of HCl (35 wt%), 10 ml of H_2O_2 (30 wt%) and 56 ml of deionized water. After final rinse,

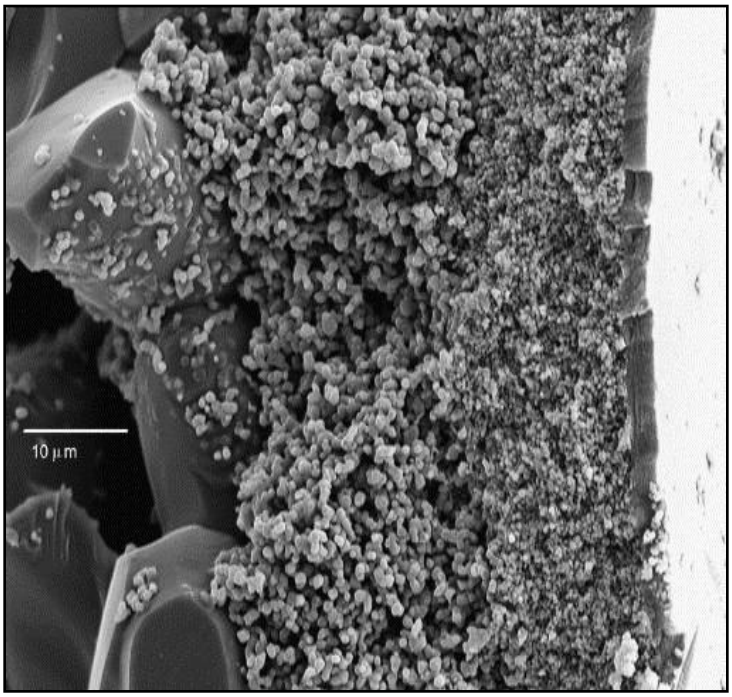

Fig. 2-1. Scanning electron micrograph image of a 5 nm Membralox® alumina membrane [105].

the membrane was placed in an oven at 100 °C for 4 h before amine functionalization.

2.1.2 Membrane Synthesis

Dendrimers were grown directly off the surface of mesoporous alumina membranes by the stepwise synthesis [106, 107]. First, 3-aminopropyldimethylethoxysilane (APDMES) was grafted to the support to provide an amine center from which the dendrimers can be grown. Amine functionalization was performed by immersing the RCA treated membrane for 24 h at 70 °C in a solution prepared by mixing 50 ml of toluene and 0.8 g of 3-aminopropyldimethylethoxysilane (0.1 M), followed by rinsing this membrane 3 times with 20 ml of toluene and 4 times with 20 ml of THF.

The surface amines were then reacted with cyanuric chloride (trichlorotriazine) to generate the dichlorotriazine intermediate. The dichlorotriazine was then allowed to react with either a monoamine or a diamine. The monoamine acted as a capping group that provided function to the membranes, while the diamine acted as a reactive spacer that continued the polymerization process. As an example, a silane treated membrane was inserted into a solution prepared by dissolving 1.4 g (7.5 mmol) of cyanuric chloride in 50 ml of THF (0.15 M) with 1 ml (6 mmol) of diisopropylethylamine, and the solution was slowly rocked (approx. 30 rpm) at room temperature for 10 h. The membrane was then rinsed 3 times with 20 ml of THF, 2 times with 20 ml of methanol, 2 times with 20 ml of dichloromethane, and 2 times with 20 ml of THF. The final THF rinse was

checked by TLC (Thin Layer Chromatography) for trace amounts of triazine and amine. Immediately after this treatment the diamine was reacted with the dichlorotriazine group. Piperazine was reacted with the dichlorotriazine by dissolving 1.3 g (15 mmol) of piperazine in 50 ml (0.3 M) of THF. A triazine treated membrane was submerged in the solution and the solution was kept at 60 °C for 14 h. The treated membrane was rinsed 3 times with 20 ml of THF, 2 times with 20 ml of methanol, 2 times with 20 ml of dichloromethane, and 2 times with 20 ml of THF. The final THF rinse was checked by TLC for trace amounts of triazine and amine. The treatment with triazine and diamine linker (piperazine) was repeated alternately to generate dendrimers of different generations.

In the final reaction step dodecylamine was attached to a triazine treated membrane to provide the specific chemical diversity. The dodecyl-functionalized membrane was synthesized by immersing a triazine treated membrane in a solution that was prepared by dissolving 1.8 g (10 mmol) of dodecylamine in 50 ml of THF (0.2 M) and keeping the solution at 60 °C for 14 h. The treated membrane was then rinsed 3 times with 20 ml of THF, 2 times with 20 ml of methanol, 2 times with 20 ml of dichloromethane, and 2 times with 20 ml of THF. The final THF rinse was checked by TLC for trace amounts of triazine and amine. The cleaned membranes were then dried in ambient condition for 12 h and stored in a vial until use.

In this manner, generation 1, 2 and 3 dendrons capped with dodecyl amine groups were produced as shown in Fig. 2-2. Previous work in the Shantz lab [106, 107]

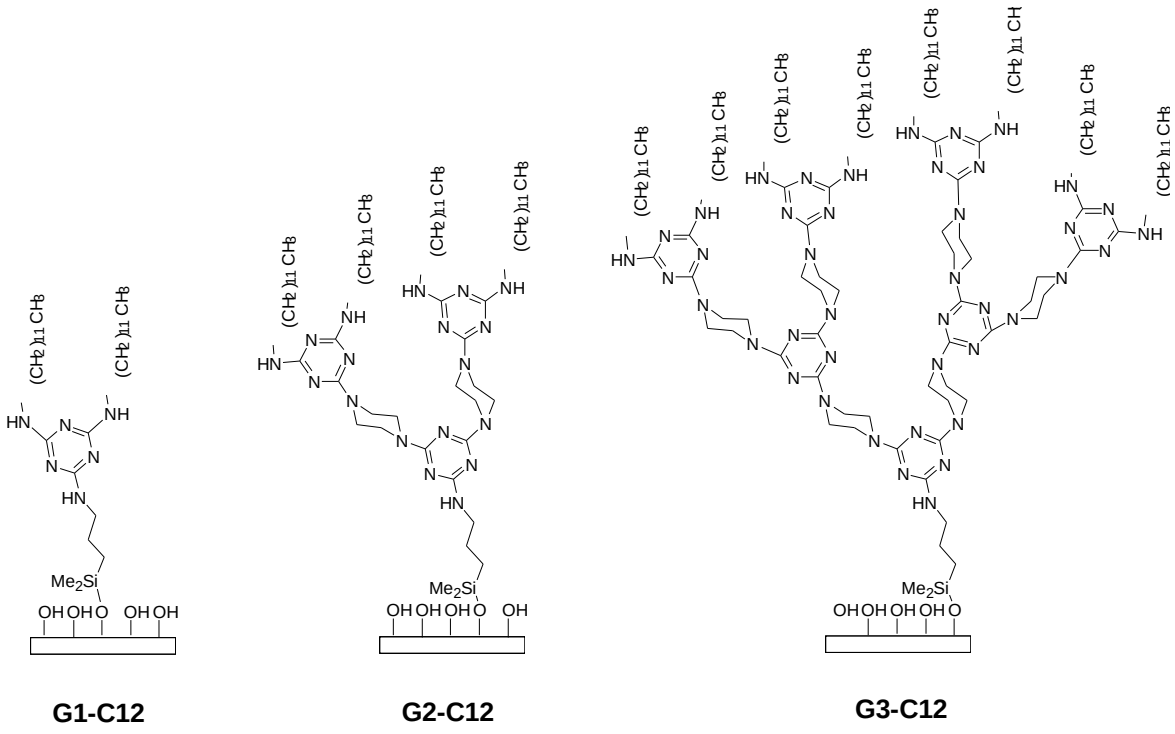

Fig. 2-2. Structures of dodecylamine-capped dendrimers of different generations.

has proved the feasibility of stepwise dendrimer synthesis via model studies of dendrimer/SBA-15 hybrids. Dodecyl chains are expected to increase the solubility for the target component, propane, to enhance propane/nitrogen gas separation. The organic molecule size is controlled based on dendrimer generation. The number of the functional groups per dendron doubles as the dendrimer generation increases. These rational modifications on the molecular architecture and chemistry by using the structural and chemical diversity of dendrimers finally lead to the development of a membrane that is customized for its application.

2.2 Synthesis of Mesoporous Silica-Ceramic Nanocomposite Membranes

In an effort to prepare for defect-free membranes, mesoporous silica (MS)-ceramic nanocomposite membranes were synthesized. For this, mesoporous silica was iteratively synthesized by evaporation-induced self-assembly (EISA) in the macropores of Membralox® membranes.

2.2.1 Materials

Brij-56 (polyethylene glycol hexadecyl ether, $C_{16}H_{33}(OCH_2CH_2)_nOH$, n ~ 10) and tetraethyl orthosilicate (TEOS, 98%) were purchased from Aldrich. HCl (Aldrich, 37 wt%) was diluted to 0.032 N stock solutions for subsequent use.

For a support material, Membralox® T1-70-25A was obtained from Pall Co., DeLand, Florida (Part# S700-01133). This tubular alumina membrane has an

asymmetric structure and the nominal pore size of the active layer is 200 nm. To use this membrane as a support for mesoporous silica synthesis, the membrane tube was cut into 1 in. pieces and cleaned by soaking in 2:1 ethanol/water solution for 24 hours at ambient temperature. The membrane pieces were then dried at 100 °C for at least 4 h, and stored in the laboratory environment until use.

2.2.2 Membrane Synthesis

Dip-coating was employed to synthesized nanocomposite membranes, and the precursor solution for coating was prepared based on previous work by Hayward and coworkers [108]: 1.15 g of Brij-56 was dissolved in 2.0 g of ethanol for 2 h. 3.0 g ethanol, 2.6 g TEOS, and 1.35 g of HCl (0.032 N) were mixed together for 20 min. The two solutions were then combined and mixed for 10 minutes. All the procedures were performed in ambient condition. Two different dip-coating methods were used as shown in Fig. 2-3.

2.2.2.1 Membrane Synthesis by Simple Dip-Coating

Cubic (*Ia3d*) mesoporous silica was synthesized in Membralox® by conventional dip-coating with evaporation induced self assembly (EISA) [80]. All the procedures are based on previous work in the Shantz lab [84]. A Membralox® membrane piece was immersed into the precursor coating solution for 5 min and then was drawn out slowly from the solution. The solution-swollen membrane piece was immediately transferred to

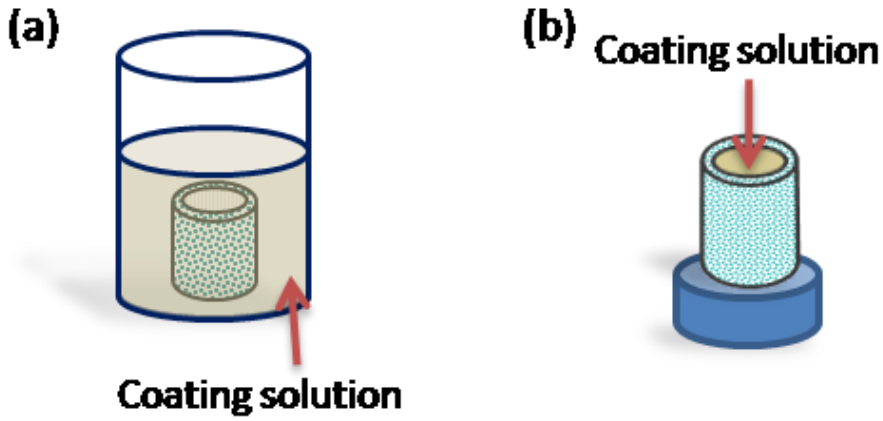

Fig. 2-3. Synthesis methods for forming OMS-ceramic nanocomposite membranes: (a) simple dip-coating, and (b) inside dip-coating.

an oven at 45 ºC and was kept at that temperature for 1 h for EISA. After cooling down to room temperature, Soxhlet extraction was performed with ethanol for 48 h to remove the surfactants from the inorganic matrix, followed by drying in ambient condition. Multiple dip-coating/surfactant extraction cycles were carried out to minimize the defects in the membrane.

2.2.2.2 Membrane Synthesis by Inside Dip-Coating

Another method was also used to incorporate mesoporous silica into Membralox® membrane supports rather than simple dip-coating. In this method, the precursor coating solution was poured inside the membrane tube that had been kept in the oven at 45 ºC at least for 30 min, and was left for 15 min in the oven at the same temperature. After the remaining coating solution was emptied out of the membrane, the membrane was kept in the oven for 1 h for drying. To remove surfactants, ethanol extraction for 48 h and/or calcinations at 500 ºC in air for 5 h (heating rate of 1 ºC/min) was performed. Inside dip-coating and surfactant removal step were repeated as needed.

2.3 Synthesis of Surface-Modified Anopore™ Membranes

In order to reduce the fouling of the protein microfiltration, Anopore™ alumina membranes were modified by the organic moieties that can endow the surface with electrostatic repulsion or hydrophilic property.

2.3.1 Materials

Anopore^{TM} membranes (25 mm diameter membranes with 200 nm cylindrical macropores) were purchased from Whatman and used as received without any cleaning. Tetraethylorthosilicate (TEOS, 99%) was purchased from Fluka. 3-aminopropyltriethoxysilane (APTES, 99%), piperazine (99%), N,N-diisopropylethylamine (DIPEA, 99%), and toluene (ACS reagent grade) were purchased from Aldrich. Cyanuric chloride (CC, 99%) was purchased from ACROS. Tetrahydrofuran (THF), methanol, ethanol, and dichloromethane (DCM) (all ACS reagent grade) were purchased from EMD. Octadecyltrichlorosilane (OTS, 98%) was purchased from Gelest. Pluronic F108 ($EO_{132}PO_{56}EO_{132}$) was obtained as a gift from BASF. Succinimidyl ester of methoxy poly(ethylene glycol) propionic acid (mPEG-SPA, 5kDa) was purchased from Nektar. Toluene was stored over activated molecular sieves; all other solvents and chemicals were used as received.

2.3.2 Membrane Synthesis

Three strategies were used to functionalize the membrane surface and are shown in Fig. 2-4.

2.3.2.1 Amine-Functionalized Membranes

Amine-functionalized membranes were synthesized by immersing a membrane into a solution of 440 mg of APTES in 200 mL toluene (10 mM) at room temperature for

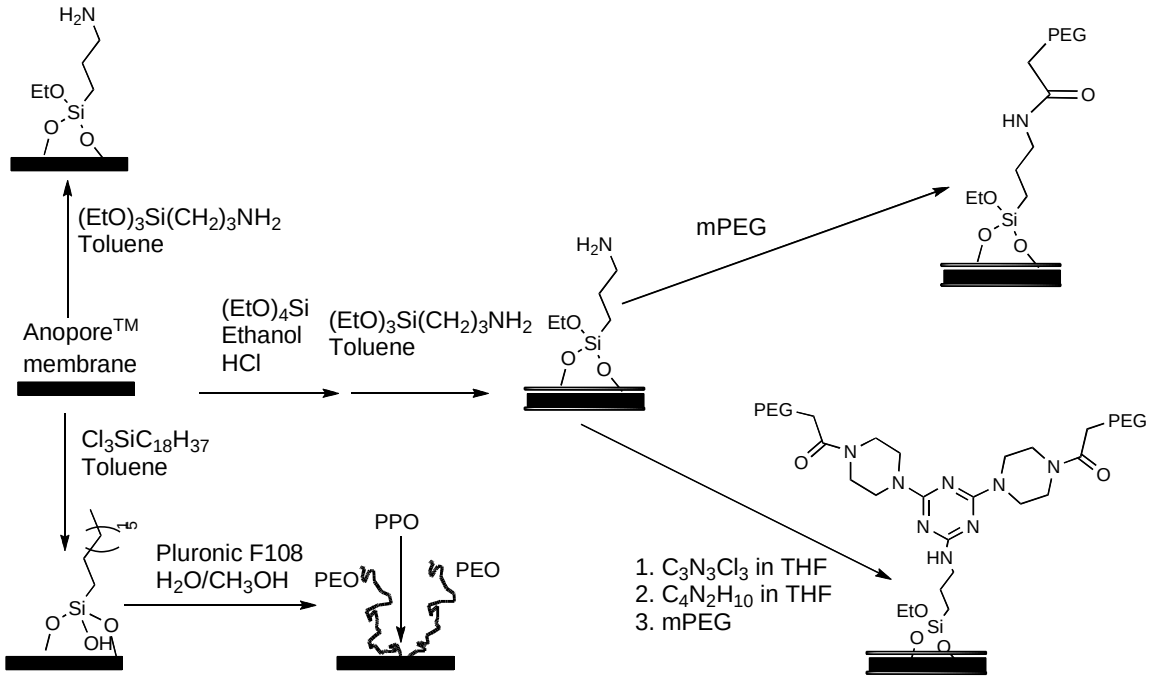

Fig. 2-4. Synthesis methods for forming hybrid membranes in the current work.

24h. The membrane was removed from the solution and repeatedly rinsed with toluene, THF, and water to remove excess APTES (samples denoted as AAM). Given that previous work has shown the difficulty of achieving high graft densities on alumina surfaces using this approach [109], amine-functionalized membranes were also prepared wherein prior to APTES grafting a silica layer was deposited on the surface of the Anopore^{TM} membrane [110] (samples denoted as ASM). The coating solution was prepared by mixing 100 mg of TEOS with 50 mL of ethanol (10 mM) that contains 1.3 mL of HCl (0.032 N). The silica layer was deposited by immersing a membrane in the solution at room temperature for 2 h, removed from the solution and dried at 95 °C for 15 min. After cooling the membrane to room temperature, amine functionalization was performed using the above procedure.

2.3.2.2 Pluronic-Functionalized Membranes

Membranes were also prepared with Pluronic F108 ($EO_{132}PO_{56}EO_{132}$) coatings. First, the bare membrane was reacted with an octadecyltrichlorosilane (OTS) solution prepared by mixing 780 mg of OTS with 200 mL toluene (10 mM) containing 3.1 mL DIPEA. The membrane was immersed in the OTS solution at room temperature for 10 h then rinsed with toluene, THF, and water. The OTS-functionalized membrane was then treated with a water/methanol solution of Pluronic (samples denoted as PCM). As a representative example, 200 mg of Pluronic were dissolved into 200 mL of a 1/1 (by volume) water/methanol mixture. The Anopore^{TM} membrane was then placed in this solution for 2 h, removed, and then dried at room temperature.

2.3.2.3 PEG-Functionalized Membranes

PEG functionalization was performed by covalently attaching mPEG-SPA to melamine-based dendrimers synthesized on the Anopore™ membranes (samples denoted as PDGxM). The dendrons were grown by first attaching APTES to the silica-coated membrane surface as described above (samples denoted as DGxM). The melamine-based dendrimer was synthesized with slight modifications to a previous protocol [107]. An amine-functionalized membrane was placed into a solution of 1.4 g of cyanuric chloride (CC) in 50 mL of THF (0.15M) with 1 mL of DIPEA. The solution was then slowly rocked (approx. 30 rpm) on a shake plate at room temperature for 10 h. The treated membrane was then rinsed three times with 20 mL of THF, two times with 20 mL of methanol, two times with 20 mL of DCM, and two times with 20 mL of THF. The membrane was then submerged in a solution of 1.3 g of piperazine in 50 mL (0.3 M) of THF. The solution was then heated to 60 °C for 14 h. This membrane was rinsed three times with 20 mL of THF, two times with 20 mL of methanol, two times with 20 mL of DCM, and two times with 20 mL of THF. The final THF rinse in both steps was checked by TLC (Thin Layer Chromatography) for trace amounts of triazine and amine. The membrane was subsequently immersed in a PEG solution (250 mg of mPEG-SPA in 50 mL of water (1 mM) or 500 mg of mPEG-SPA in 50 mL of water (2 mM)) for 2 h to react with mPEG-SPA. For comparison mPEG-SPA was also grafted to an amine-functionalized membrane (with silica deposition, denoted as APM). In this case, the amine-functionalized membrane was immersed in a 2 mM PEG solution at room temperature for 2 h.

2.4 Synthesis of UV-Regeneratable Hydrophilic Membranes

TiO_2 or TiO_2/SiO_2 layers were coated onto Anopore^{TM} alumina membranes to reduce the flux decline and regenerate the membranes by UV irradiation, without severe acidic or basic conditions.

2.4.1 Materials

Anopore^{TM} membranes (25 mm diameter with pore size of 200 nm) were used after overnight cleaning in ethanol. Tetraisopropylorthotitanate (TPOT, 98%) and hydrochloric acid (ACS reagent grade, 37%) were purchased from Aldich. Tetramethylorthosilicate (TMOS, 99%) and 2-propanol (ACS reagent grade, > 99.5%) were purchased from Fluka. All chemicals were used as received.

2.4.2 Membrane Synthesis

Sol-gel process was employed to form a thin layer of photocatalytic metal oxides on Anopore^{TM} membranes. A TiO_2 precursor solution (30 mM) was prepared by dissolving 450 µl of TPOT in 50 ml of 2-propanol containing 180 µl of hydrochloric acid while stirring. After the solution was stirred for 1 h in a capped Teflon container, an Anopore^{TM} membrane was immersed in the solution for 20 min and then was drawn out slowly from the solution. After dried in ambient condition for 1 h, the membrane was transferred to an oven at 120 ºC and was kept at that temperature for 6 h for annealing. For comparison, spin-coating was carried out using a spin rate of 2000 rpm

for 1 min solely (without dip-coating) or after the drying of the dip-coated sample for 1 h in ambient condition.

TiO_2-SiO_2 coated membranes were also synthesized following the same protocol as described above. For a precursor solution (30 mM), 45 µl of TMOS (0.3 mmol) was prehydrolyzed in 50 ml of 2-propanol containing 180 µl of hydrochloric acid for 2 h. Then, 360 µl of TPOT (1.2 mmol) was added to the TMOS solution while stirring. A membrane was first dip-coated and then spin-coated to achieve a uniform and defectless coating, and annealed at 120 ºC for 6 h.

2.5 Membrane Testing

2.5.1 Gas Permeation Test

Permeation measurements of the individual gases were performed using a home-built unit as shown in Fig. 2-5. Pure nitrogen (99.998%), helium (99.998%) and propane (99.5%) gases were used as received from Praxair Distribution, Inc. The ambient temperature ranged from 20 to 22 ºC. The pressure was ambient on the permeate side. The pressure on the feed side was regulated up to 90 psi by a pressure regulator. The volumetric flow rate was measured at several pressure differences ranging from 5 to 90 psi for reverse-selective membranes and 5 to 40 psi for OMS-ceramic membranes. The average value of the final four measurements at each pressure was taken in order to get the reported value for a permeate flow rate after it reached the steady state. We note that permeance typically required some time to reach steady state for propane. It usually

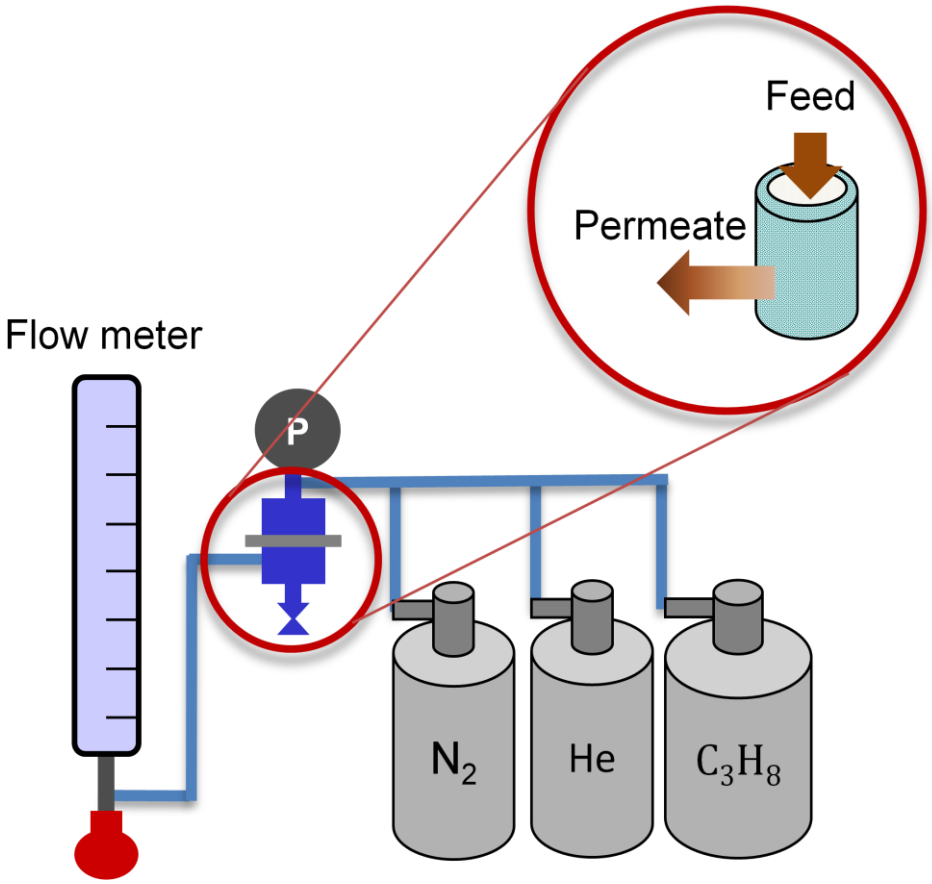

Fig. 2-5. Gas permeation test apparatus that was used for this study.

took a longer stabilization time, up to 1 – 2 days, for the organic treated membrane than for the bare membrane, which took around 15 min. This is not unusual for solubility-based separations with polymeric membranes and is attributed to conformational changes in the polymer over time [111, 112].

The gas permeance was calculated from the volumetric flow rate that was measured at different pressures:

$$P\left(\frac{mol}{m^2 \sec bar}\right) = \frac{J}{\Delta p} = Q \times \left(\frac{mol}{22.4l}\right) \times \left(\frac{T_0}{T}\right) \times \left(\frac{p}{p_0}\right) \Big/ A\Delta p \qquad (2\text{-}1)$$

where Q is the volumetric flow rate, T_0 = 273 K, p_0 = 1.01 bar, A is the surface area of the membrane, and T and p is the ambient temperature and pressure, respectively. Since the accurate thickness of active layer is hard to be measured for Membralox® membranes, permeance was used for comparison of the data instead of permeability.

2.5.2 Protein Filtration Test

Bovine serum albumin (BSA, Aldrich (A7906), Mw 67kD, pI 4.7) and lysozyme (LSZ, Aldrich (L6876), Mw 14kD, pI 11.0) were used as model proteins to investigate the membrane fouling behavior. The solutions of BSA and lysozyme were prepared by gently dissolving powdered protein without vortex for 2 h in phosphate buffered saline (PBS) pre-filtered through a 0.2 μm cellulose acetate membrane (VWR) (2 g/L, pH 7.4). Fig. 2-6 shows the apparatus for protein filtration test in this experiment. All filtration experiments were conducted with the protein solution within 2 h of preparation, and

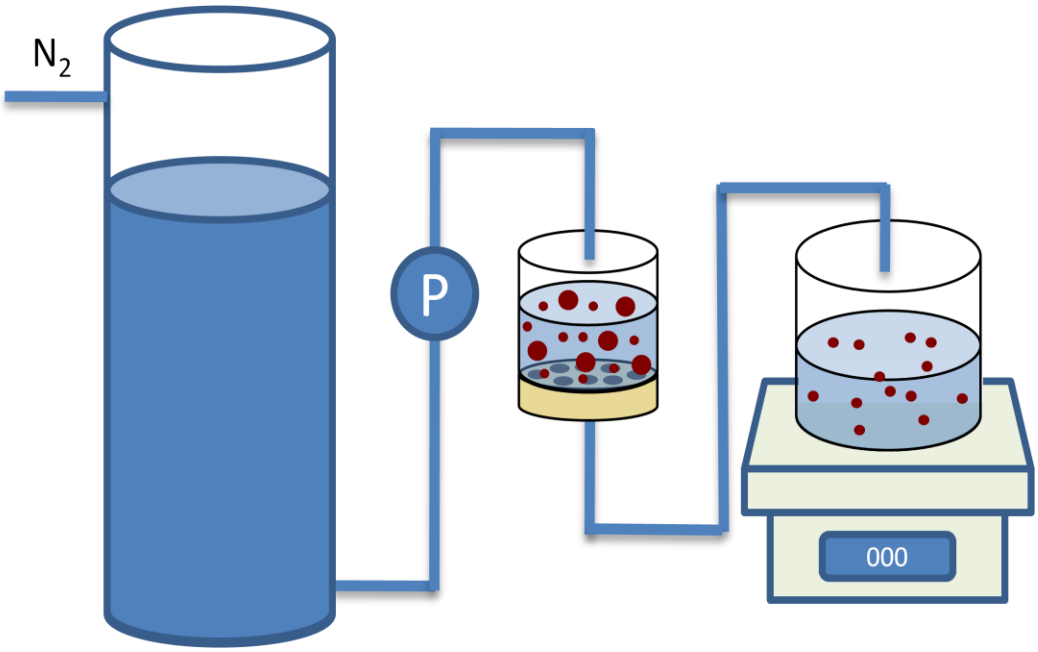

Fig. 2-6. Protein filtration test apparatus that was used for this study.

performed without stirring in a 25 mm diameter stirred cell (Model 8010, Amicon) connected to a N_2 pressurized solution reservoir (3 psi) at room temperature. The PBS flow rate was measured at constant pressure (3 psi) until steady state and was then replaced by protein solution to measure the protein flux. Filtration flow was measured by timed collection using a digital balance, which was employed to determine the fouling and the flux decline during filtration. Normalized flux plots were calculated by differentiating the permeate and normalizing them by the initial flux.

2.6 Analytical

Nanocomposite materials and membranes were characterized by several analytical methods.

Electron Microscopy

Field-Emission Scanning Electron Microscopy (FE-SEM) measurements were performed to determine the pore size and surface morphology of the membranes using a Zeiss Leo-1530 microscope operating at 1-10 kV. The microscope employs a GEMINI electron optical column with a Schottky-type field emitter, single condenser, crossover-free beam path, large specimen chamber with two chamber ports for EDS (Energy Dispersive X-ray Spectroscopy) adaptation, four accessory ports on the chamber and three on the door, fail-safe vacuum system, digital image store and processor. Shell transitions caused by the interaction of an electron beam and the atoms in the sample

result in a characteristic X-ray emission. EDS can provide qualitative and quantitative elemental information by detecting the energy of this emitted X-ray, and the available sample depth is generally several microns.

Transmission electron microscopy (TEM) produces a real space image of the mesoporous nature that can be used to examine the structural ordering, complementing PXRD or SAXS results. For this, JEOL 2010 microscope with a lanthanum hexaboride (LaB_6) filament and an excitation voltage of 200 kV was used. The samples were dispersed in ethanol (100%, Aldrich) and placed on a 400-mesh copper grid.

X-ray Photoelectron Spectroscopy

X-ray photoelectron spectroscopy (XPS) measurements were performed to determine the surface elemental composition using an Axis His 165 Ultra Kratos instrument with an Al Kα X-ray source. The scan rate was 300 sec per scan and the points were collected at every 0.5 eV.

Powder X-ray Diffraction

Powder X-ray diffraction (PXRD) was used to determine structural ordering of mesoporous silica or crystallinity of metal oxides, and was performed using a Bruker-AXS D8 powder diffractometer with Cu Kα radiation over a range of 0.8 to 5° 2θ. Peak intensities and 2θ values were determined using the Bruker program EVA. Powder X-ray diffraction measurements were also performed using a Bruker NanoSTAR 1070 mm

small angle X-ray scattering instrument with a rotating anode (FR591) and a copper target (1.5417 Å).

Adsorption (Porosimetry)

Porosimetry experiments give useful information about the pore size distribution, pore volume, and surface area of the materials. Nitrogen adsorption experiments were performed on a Micromeritics ASAP 2010 micropore system using approximately 0.1 g of sample. The samples were degassed under vacuum at room temperature for 2 h, then at 100 °C for 12 h before analysis. The micropore and mesopore volumes were determined using the α_s-method [113]. The mesoporous size distributions were calculated from the adsorption branch of the isotherm using the Barret-Joyner-Halenda (BJH) method [114] with a modified equation [115] for the statistical film thickness.

Thermal Gravimetric Analysis

Thermal gravimetric analysis (TGA) were performed using a TG 209C Iris Instrument from Netsch over a temperature range of 25 to 600 °C using oxygen and nitrogen as carrier gases and temperature ramping rate of 2 °C/min.

Infrared Spectroscopy

Infrared spectroscopy was performed on a Thermo Nicolet Nexus 670 FTIR. Background spectra were collected after 30 min of evacuation. The membrane samples were analyzed after 30 min of evacuation, and 64 scans were acquired per spectrum.

Anopore™ membranes (thickness 60 μm) were directly used for the measurement, without mixing KBr.

Light Scattering

Dynamic light scattering was performed to measure the particle sizes of proteins using a ZetaPALS from Brookhaven Instrument Corporation.

UV-Vis Spectrophotometer

Optical absorption spectra of the photocatalytic membranes were taken using the Hitachi U-4100 UV-Vis-NIR spectrophotometer with tungsten and deuterium lamps in diffuse reflectance mode. Scan speed was 120 nm/min and the sampling interval was 1 nm in the span between 200 and 500 nm.

CHAPTER III

REVERSE-SELECTIVE MEMBRANES FORMED BY DENDRIMERS ON MESOPOROUS CERAMIC SUPPORTS *

3.1 Introduction

Solubility-based separations are desired in many applications where heavier species need to be removed from lighter gases [27]. Moreover, this reverse-selective property often enables membranes to overcome the trade-off relationship between the permeability and the selectivity. Nanocomposite membranes have been studied as a viable route to improved membrane materials for reverse-selective separations. Polymers doped with inorganic nanoparticles are one way forward [9, 116-122]. For example, Merkel *et al.* doped poly(4-methyl-2-pentyne) with silica nanoparticles and studied the resulting composites for the separation of *n*-butane from methane [9]. With increasing weight percent silica, they observed simultaneous increases in *n*-butane permeability and *n*-butane / methane selectivity. The main reason was a change in the polymer packing, and thus the free volume distribution, due to the presence of nanoparticles.

---

* Reprinted with permission from "Reverse-selective membranes formed by dendrimers on mesoporous ceramic supports" by S. Yoo[1], S. Yeu[1], R. L. Sherman, E. E. Simanek, D. F. Shantz, and D. M. Ford, J. Membr. Sci. 334 (2009) 16-22. © 2009 by Elsevier B.V.

Another approach employs nanocomposites comprising organic moieties deposited onto a mesoporous ceramic framework. This approach allows one to design and build membranes that simultaneously deliver the desired chemistry and the desired free volume thereby making the membrane formation process quite versatile. This approach of forming organic-inorganic composites has shown great promise in creating materials for solubility-based separations [20, 105, 123-126]. Work in the Ford lab [105, 123-125] and that of J.D. Way [20, 127-129] has led to structure-property relationships for membranes comprising organosilanes attached to porous silica and alumina. This work demonstrated that it is possible to rationally modify permeation properties by choosing pore size, and type and amount of organic group deposited. The Martin group has used similar nanocomposites to carry out enantiomeric separations in the liquid phase [130].

Here we develop this concept of engineering the membrane nano-architecture by exploring a new type of organic phase, melamine-based dendrimers. In this study, we have achieved impressive reverse selectivities by engineering the organic phase and choosing an appropriate mesoporous substrate. Melamine-based dendrimers were chosen as a scaffold for functionalization in order to control free volume and solubility of the membranes. Also, the current work shows that a small residual amount of solvent, often present in the membranes even after drying, can have significant effects on the separation selectivity.

3.2 Experimental

Generation 1, 2 and 3 dendrimers were iteratively synthesized on mesoporous ceramic Membralox® supports and capped with dodecyl amine groups, as described in section 2.1. Membrane permeance was measured for nitrogen, helium and propane as shown in section 2.5.1. Unless otherwise noted, all data presented here were obtained using a pressure difference of 20 psi.

3.3 Results

Fig. 3-1 shows representative helium, nitrogen, and propane permeation data on the bare membranes. The data shows that typical helium/nitrogen selectivities fall in the range of 2.2 – 2.4, consistent with previous literature indicating that these membranes likely have some small number of pinhole defects [127]. The propane permeance exhibits an abrupt increase with pressure due to surface diffusion on the inorganic surface; the propane/nitrogen selectivities observed are low (~ 2.1 at 20 psi) and consistent with previous literature [125, 131].

Fig. 3-2 shows helium/nitrogen selectivity versus nitrogen permeance data for a membrane from bare to G3 functionalization. (Note that the dendrimers grown on these membranes were capped with piperazine, rather than the long C12 functionality shown in Fig. 2-2). The data clearly show a significant enhancement in permeance after RCA treatment, which could be caused by desorption of contaminants from the bare membranes, a nominal increase in the pore size due to the basic / acidic cleanings, or

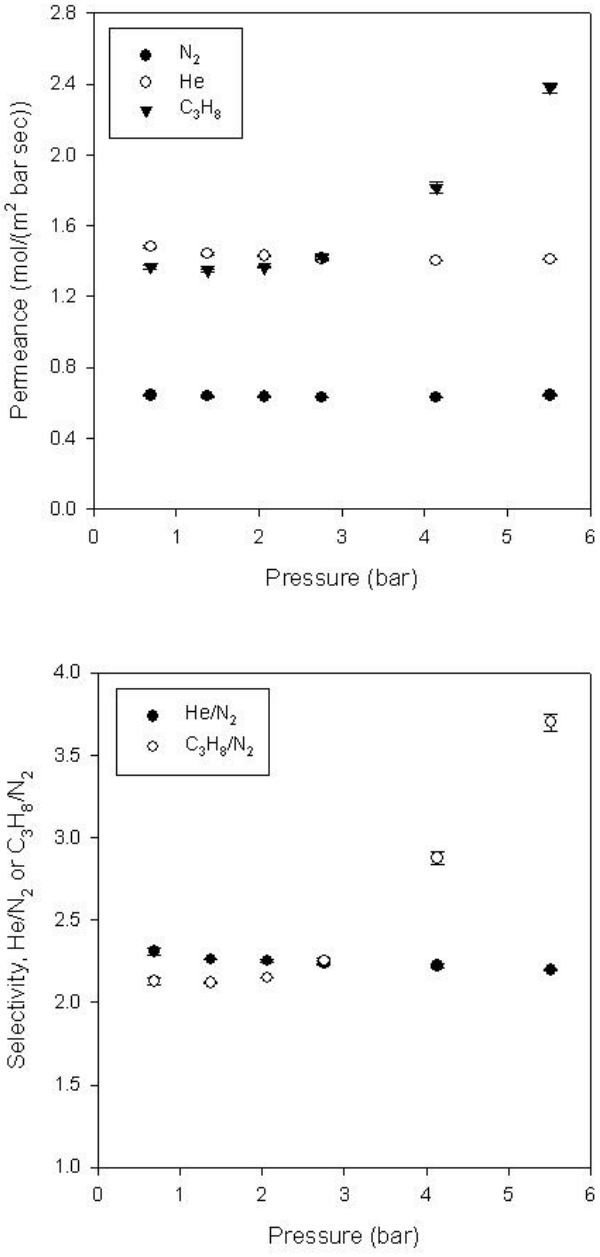

Fig. 3-1. Permeance (top) and selectivity (bottom) of a bare Membralox® membrane.

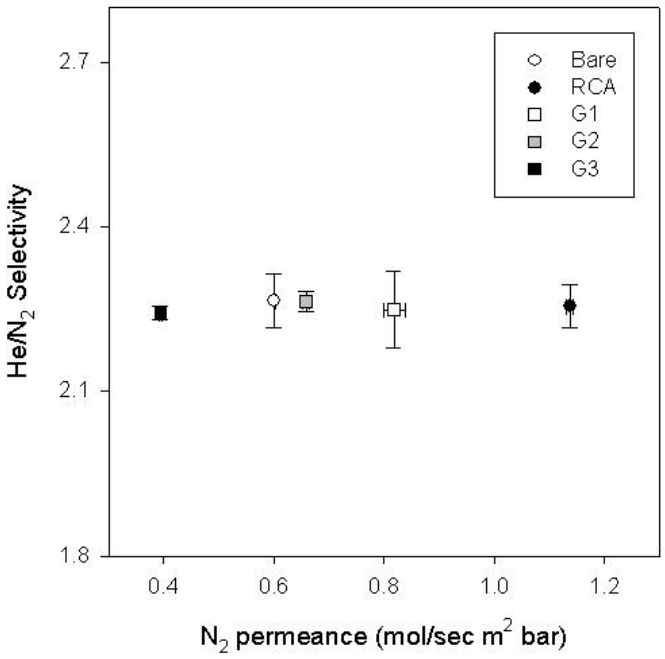

Fig. 3-2. Helium/nitrogen selectivity with nitrogen permeance for bare, RCA, and dendrimer attached membranes. Note that the dendrimers are not alkyl functionalized.

both. The permeance decreases as the dendrimer generation increases while the helium/nitrogen selectivity remains effectively constant over the different dendrimer generations shown in Fig. 3-2. The permeance decreases are not as large as those seen for C12-capped dendrimers, as presented next.

Fig. 3-3 shows the separation performance of our composite membranes in the usual form of selectivity *vs*. permeance (i.e. Robeson plot). The first-generation dendrimer, G1-C12, yields a slightly enhanced permeance with negligible change in selectivity relative to the untreated support. G1-C12 is too small to have much effect on transport through the mesopores, except near the pore surface where it may enhance adsorption and surface flow. The second-generation dendrimer, G2-C12, shows a reduction in permeance with a slight increase in selectivity. This larger molecule is starting to fill the pores, which has the simultaneous effects of reducing permeance and likely solubilizing the propane to enhance selectivity. Finally, the G3-C12 samples show dramatic increases of selectivity, with values ranging between 5 and 70. By contrast, a commonly used commercial polymer membrane, polydimethylsiloxane (PDMS), shows a selectivity of 18 [132]. One of our G3-C12 dendrimer-ceramic nanocomposite membranes thus shows a selectivity nearly 4 times higher than a standard industry benchmark, a remarkably promising result.

To view this from another perspective, we estimated the solubility-selectivity (last term on the right-hand-side of Eq. (1-25)) using correlations based on the vapor pressures of propane and nitrogen [133] and on the solubilities of these two gases fit across a wide range of liquids and polymers [134]; the results were 46 and 59

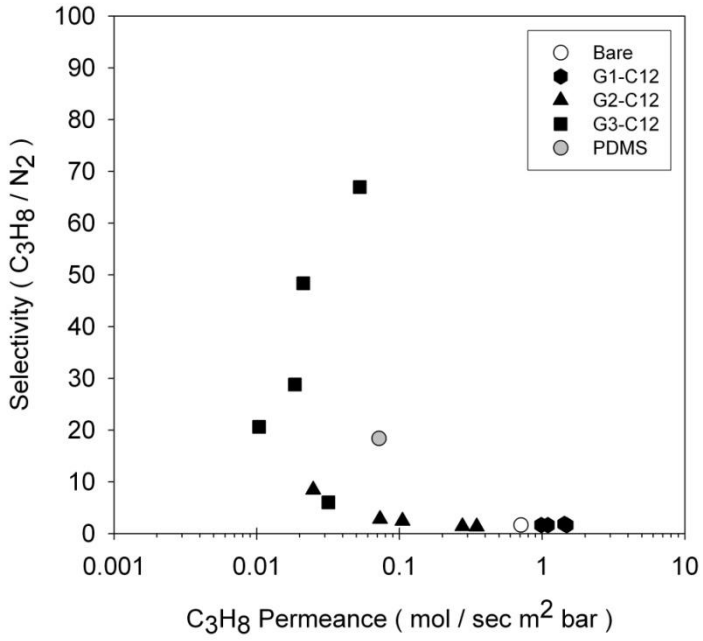

Fig. 3-3. Robeson plot of the propane/nitrogen separation performance of the nanocomposite membranes. Each individual point represents the results from one membrane piece. The PDMS value is from the literature [132].

respectively. Also, bulk polyethylene exhibits a propane/nitrogen solubility-selectivity of 55 for HDPE and 93 for LDPE [135]. Our best G3-C12 membranes are thus showing an overall performance at or near the upper limit of theoretical expectations; presumably the hyperbranched structure of the dendritic groups brings both high solubility-selectivity and a high enough free volume so that the ratio of diffusivities of the two species is driven close to unity.

While the high selectivities observed for some of the membranes in Fig. 3-3 is very exciting, the dramatic spread in the selectivities needs to be understood. Fig. 3-4 shows the data for the G3-C12 membranes in Fig. 3-3 as propane permeance versus nitrogen permeance. The diagonal in Fig. 3-4 now corresponds to a selectivity of one and the most selective membranes are the points that are farthest from the diagonal. The overall shape is now like a fishhook with the most selective G3-C12 membrane at the tip. Two possible conclusions can be drawn from this plot. First, the ability of the organic phase to reduce the light gas (nitrogen) flow appears to be key in making membranes that are selective for the heavy gas (propane). Only in the region where the nitrogen permeance drops most sharply does the selectivity become appreciable; furthermore, the trend of decreasing nitrogen permeance correlates with increasing physical size of the dendrimers employed. Second, once the light gas (nitrogen) flow is sufficiently restricted, the ability of the organic phase to solubilize the heavy gas (propane) appears to be key in creating the most selective membranes. Within the G3-C12 data on the far left in Fig. 3-3, differences in selectivity correlate more strongly with

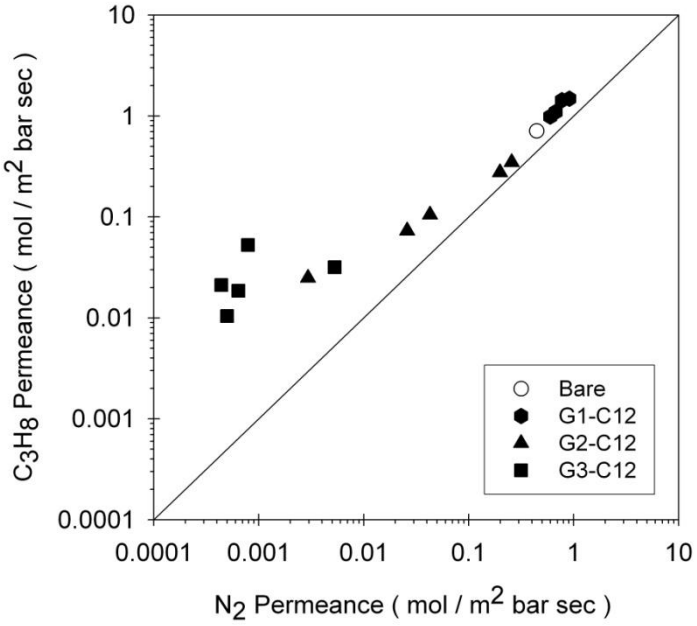

Fig. 3-4. Propane permeance versus nitrogen permeance of the data.

differences in propane permeance than nitrogen permeance; the underlying cause is most likely based on solubility effects.

This latter conclusion still begs the question of the mechanistic reason for the large range of selectivities across the G3-C12 group. Initial efforts to address this focused on the variability of the underlying support, careful examination of the amine functionalization, etc. Our best assessment, from that work, is that the inherent differences in the substrate do not cause the large variations in selectivity for the G3-C12 samples observed in Fig. 3-3 and 3-4. For example, even though helium/nitrogen selectivity and permeance for several membrane pieces did not show large difference from the behavior and the values in Fig. 3-1 and 3-2 (from bare to dendrimer attached membranes), the resulting alkyl functionalized membranes showed a wide range of propane/nitrogen selectivity (2 – 19) without noticeable correlation with membrane history. This implies that the inherent differences in membrane pieces such as defects may not be a critical factor in G3-C12 membranes since in all likelihood the selectivities observed are driven by differences in the solubility of the two molecules. Moreover, based on previous work from our labs the dendrimer synthesis proceeds cleanly on a variety of inorganic substrates and thus it seems unlikely that the differences are due to inherent variability in the dendrimer synthetic chemistry.

These conclusions led us to think about the effects of residual THF solvent in the membranes, as affected primarily by the details of the rinsing and drying steps in the synthesis process. We decided to test for solvent effects by taking existing membranes through a cycle of re-rinsing and heating, and we made several very important

observations. It was anticipated originally that heating would not be needed remove all the residual THF. Fig. 3-5 shows the propane/nitrogen selectivity for a membrane that displayed a very high selectivity (i.e. the point with a propane/nitrogen selectivity of 49 in Fig. 3-3) after a series of rinsing/drying treatments. In Fig. 3-5, *Initial* is the first measurement of permeance and the selectivity after synthesis (as shown in Fig. 3-3), *THF soaking* is the results measured after rinsing the membrane with THF for 30 min followed by 2 h drying in ambient condition, and *100°C drying* is the measurement after drying the membrane overnight in the oven at 100 °C. The results in this figure show the effect of THF on membrane performance. The first THF soaking test (*THF soaking I*) showed a decreased selectivity compared to the *initial* result, which could be ascribed to the adsorption of moisture in the membrane pores since this test was performed 2 years after the *initial* test. This conclusion seems reasonable in that Gallaher and Liu [104] demonstrated from their thermal treatment tests that the adsorption of moisture to Membralox membrane is very strong. By repeating experiments, the effect of moisture adsorbed in the pores may be reduced as shown in Fig. 3-5, that is, as drying at 100 °C and rinsing with THF repeated, the nitrogen and propane permeance after *100°C drying* gradually increased (compare *100°C drying I, II, and III*) whereas the nitrogen permeance decreased and the propane permeance increased after *THF soaking* (compare *THF soaking I, II, and III*). In terms of propane/nitrogen selectivity, while the results after *100°C drying* show low values, the selectivities after *THF soaking* significantly increased again even up to 80. This indicates that there is an effect caused by residual solvent (THF) in the membrane. To understand this solvent effect, the solubility

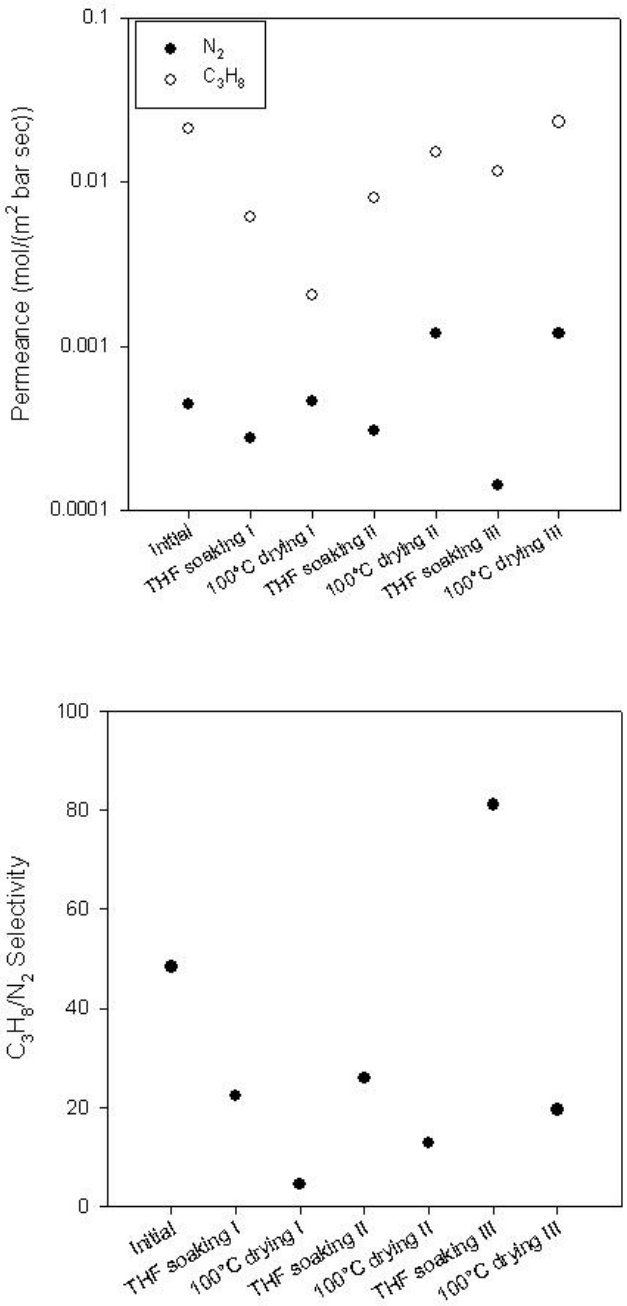

Fig. 3-5. Nitrogen and propane permeance (top) and propane/nitrogen selectivity (bottom) with successive rinsing/drying treatments for a G3-C12 membrane that showed a high (C_3H_8/N_2 = 49) selectivity.

coefficients of nitrogen and propane in THF were compared. Since, to the best of our knowledge, there are no reports on experimental comparison of solubility between nitrogen and propane in THF at room temperature, we calculated the solubility coefficient of propane in THF at 20 °C by extrapolating the solubility in Gibanel *et al.*'s results [136] as a function of Lennard-Jones constant [137]. This calculation was based on the relation that log x_2 (x_2 is the mole fraction of gas) is linearly proportional to Lennard-Jones constant for different gases in the same solvent, suggested by Jolley and Hildebrand [138]. Fig. 3-6 shows that Gibanel *et al.*'s data are in good agreement with the observation of Jolley and Hildebrand. The solubility coefficient of propane that was obtained from calculation is 525.6 mole/(m^2 bar), which means the ideal solubility-selectivity is 86 when using the experimental value [136] for the solubility coefficient of nitrogen. Therefore, some extraordinarily high selectivities could be attributed to residual THF in membranes provided the solubility difference is dominant compared to that of the diffusivity.

To attempt to further validate this conclusion, Fig. 3-7 shows the same set of experiments performed on a membrane that displayed a low propane/nitrogen selectivity (selectivity of 6 from G3-C12 membranes in Fig. 3-3). Although overall selectivities are lower than those in Fig. 3-5, the results show very similar behavior to the data of Fig. 3-5. As to G2-C12 membranes with higher permeance, high selectivities were not observed even after THF soaking, possibly because the retention of solvent is not as strong with the smaller organic functionality. Other possible explanations for the difference in absolute selectivities between Figs. 3-5 and 3-7 could be the variability of

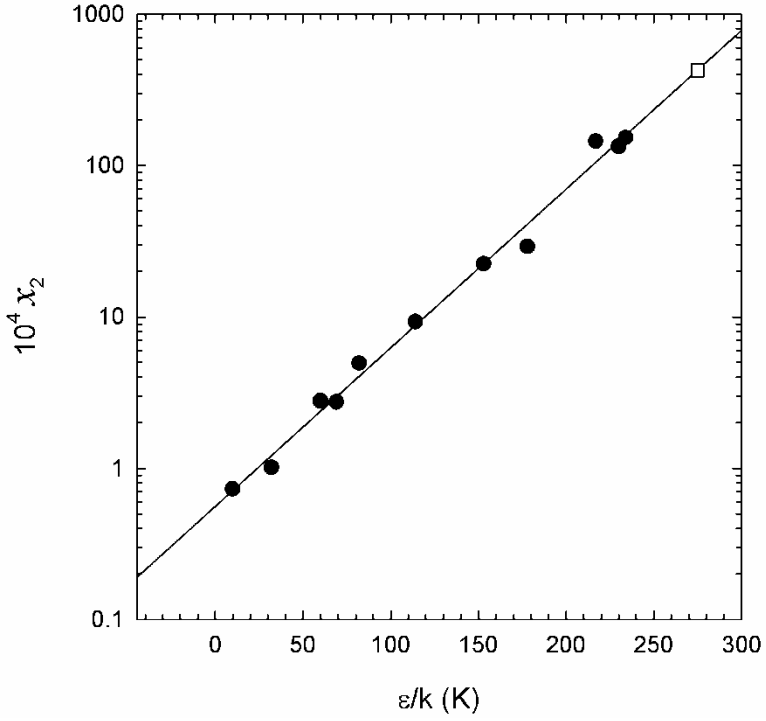

Fig. 3-6. Solubility coefficients of non-polar gases in THF at 20 °C and 1 bar [136] as a function of their Lennard-Jones constants [137]. Filled circles from left to right represent He, Ne, H_2, D_2, N_2, Ar, CH_4, Kr, C_2H_4, Xe, and C_2H_6. The solubility of C_3H_8 (blank square) was extrapolated from the regression.

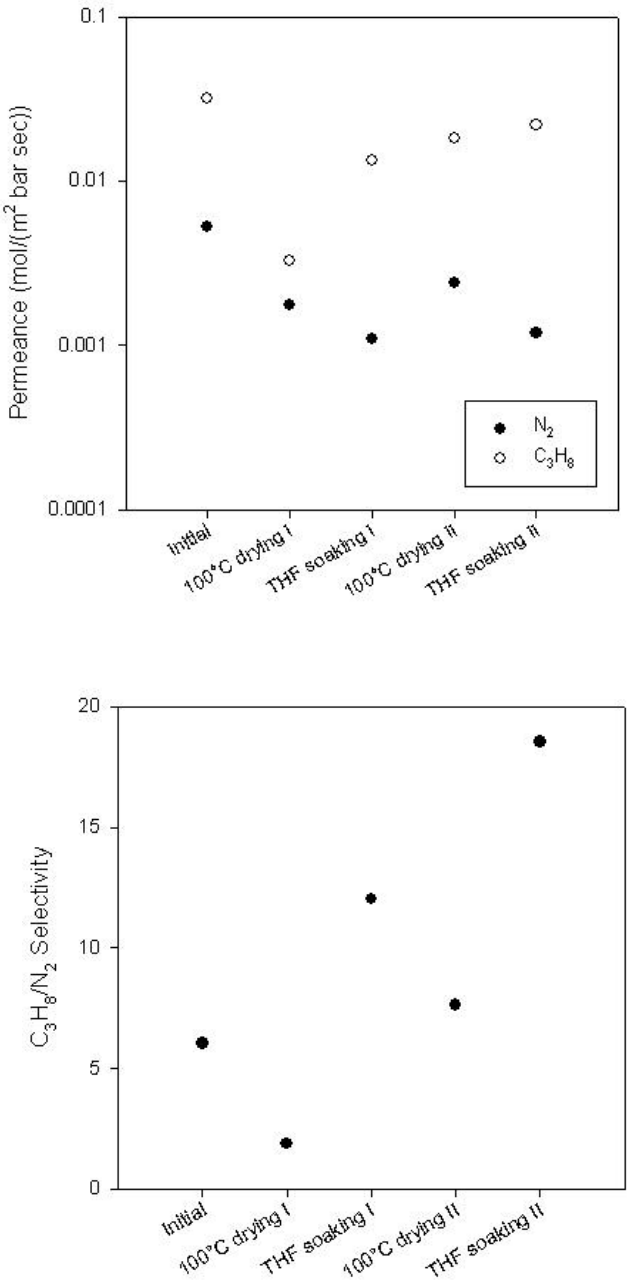

Fig. 3-7. Nitrogen and propane permeance (top) and propane/nitrogen selectivity (bottom) with successive rinsing/drying treatments for a G3-C12 membrane that exhibited a low (C_3H_8/N_2 = 6) selectivity.

the substrate, either in terms of surface hydration state or pore size distribution. Slightly smaller pores, for instance, would likely lead to inefficient capping of the dendrimers with C_{12} chains and presumably change both the propane and nitrogen permeability as well as the affinity of the residual THF to remain in the membrane.

While in some sense the results in Figs. 3-5 and 3-7 are not encouraging, some of the selectivities are extremely high and we now have a rational basis for explaining both the high selectivities and the scatter shown in Fig. 3-3. There is some inherent variability in the underlying membrane support (pore size, surface hydration, etc.) that affects the progress of the *in situ* dendrimer synthesis chemistry, resulting in variable dendrimer loading in the mesopores under the same reaction protocol. This variability in dendrimer loading probably accounts for some of the scatter in the permselectivity measurements for G3-C12 membranes in Figs. 3-3 and 3-4. However, it is also reasonable to assume that the amount of retained solvent is sensitive to the dendrimer loading. This provides an additional source of variability, and likely a significant one, since we have demonstrated that the membrane permselectivity properties can be tremendously sensitive to soaking/drying cycles with additional solvent. In some cases, re-solvating the membrane with THF resulted in selectivity higher than that seen in the original as-synthesized state.

Given the importance of residual solvent in the modified membranes, an issue of practical importance is the stability of that solvent and how the performance of these membranes will change with time on stream. Fig. 3-8 shows the nitrogen and propane permeances and selectivity at 20 psi as a function of time on stream for a G3-C12

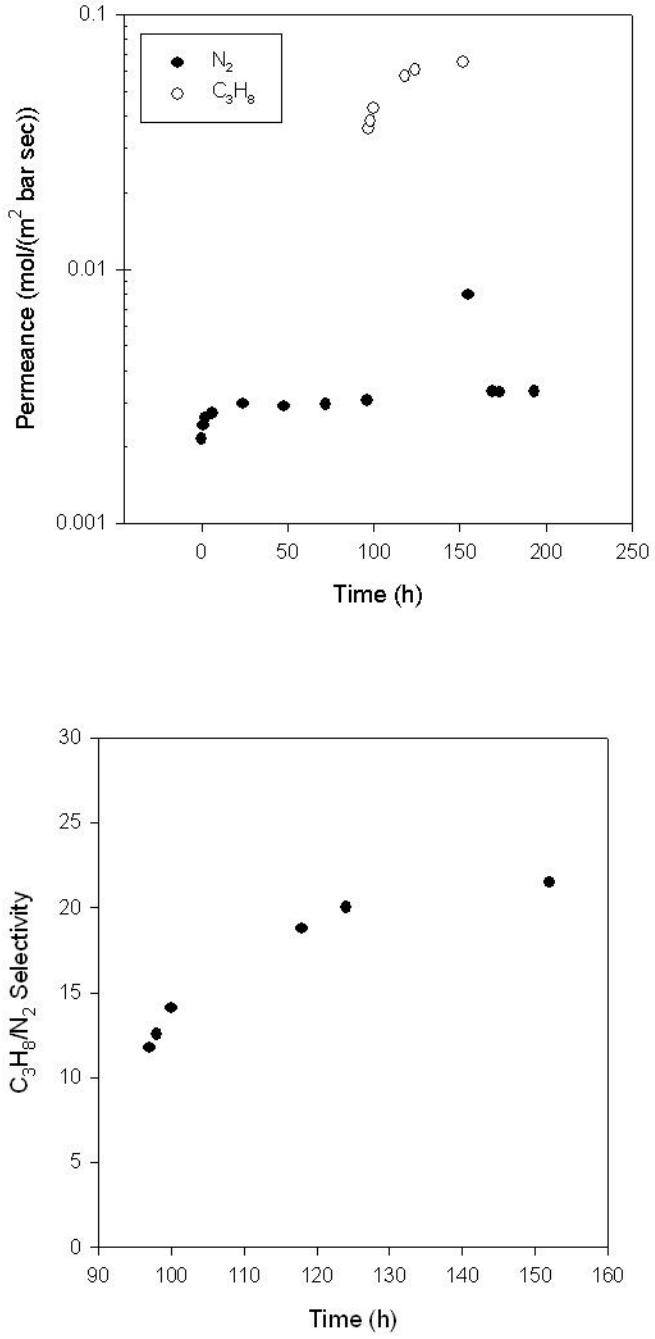

Fig. 3-8. Nitrogen and propane permeance (top) and propane/nitrogen selectivity change with time (bottom) for a G3-C12 membrane.

membrane. The membrane was dried at 100 °C overnight, followed by soaking in THF for 30 min and drying at room temperature for 30 min before the test. The nitrogen permeance increased by approximately 50% and then stabilized within 20 h, and propane also showed an increase in permeance after a nitrogen permeation test for 96 h. After a propane permeation test, the nitrogen permeance in second test almost recovered the initial value. Selectivity was calculated based on the nitrogen permeance at 100 h. This result indicates that the residual solvent is so stable in G3-C12 membranes that the stable selectivity can be obtained after an initial (likely partial) loss of solvent by gas flow.

3.4 Conclusions

We have created dendrimer-ceramic nanocomposite membranes that show exceptionally high selectivity for a small hydrocarbon species (propane) over a light gas (nitrogen) with a large scatter in selectivity. Through the repeated drying/rinsing treatments of the membranes, it was found that the residual solvent in membranes appeared to be critical to the membrane performance. Although the adsorbed solvent in membranes is removable at high temperature, the adsorption was strong enough not to cause the abrupt change of permeance and selectivity during the permeation test.

CHAPTER IV

ITERATIVE SYNTHESIS OF MESOPOROUS SILICA IN MACROPOROUS CERAMIC SUPPORTS

4.1 Introduction

Inorganic materials such as zeolites, silica, titania, and alumina have been widely investigated as porous membranes due to their excellent chemical and mechanical stability, which is often hard to achieve in polymeric membranes. One of the challenges of inorganic membranes, however, is to prepare defect-free membranes, and much effort has been expended toward this end [84, 139-141]. Uniform pore sizes are also highly desired to achieve high selectivities. For these reasons, ordered mesoporous silica (OMS) has attracted much interest as a membrane material. Reid *et al.* [142], for example, added MCM-41 in polysulfone membranes to increase gas permeability without losing selectivity. Also, hybrid membranes of OMS grown in macroporous alumina supports have been explored in an effort to develop membranes with narrow pore size distributions, which may offer more consistent framework for the synthesis of nanocomposite membranes. For example, Nishiyama *et al.* [143] deposited MCM-48 on a porous alumina support by hydrothermal treatment. McCool *et al.* [82] compared dip-coating with hydrothermal deposition for fabrication of a highly permeable, defect-free membrane. Brinker and coworkers synthesized a thin and uniform mesoporous silica film on ceramic supports by aerosol-assisted deposition [144], and recently reported the

synthesis of dual micro-/mesoporous silica-layered membranes exhibiting high permselectivity [12]. Yoo *et al.* [84] synthesized defect-free mesoporous silica-alumina membranes by repeating dip-coating cycles. Although these works have demonstrated that OMS can be a promising material for the porous membranes with uniform and defectless framework, more studies on defect and surfactant removal are necessary to meet the requirements of practical use, in that most of the works for OMS composite membranes have been made on flat disk-type supports without detailed study on surfactant removal. In this study, tubular mesoporous silica (MS)-ceramic membranes have been prepared via multiple dip-coating or inside dip-coating cycles, since currently most of the membrane modules for gas separations are hollow-fibers [8]. Also, the effect of the surfactant removal step on membrane performance was investigated.

4.2 Experimental

The membranes synthesized by simple dip-coating and ethanol extraction were denoted as SD-EtOH. The other membranes were synthesized by multiple cycles of inside dip-coating followed by ethanol extraction and/or calcination, and are denoted as ID-EtOH for the samples prepared by ethanol extraction, ID-Calcin for the samples that were calcined, and ID-EtOH-Calcin for the samples that were first extracted and then calcined. Detailed procedures are given in section 2.2.

To analyze the microstructure of the membrane, Scanning Electron Microscopy (SEM), Energy Dispersive X-ray Spectroscopy (EDS), Transmission Electron

Microscopy (TEM), powder X-ray diffraction (XRD) and nitrogen adsorption porosimetry were performed as described in section 2.6. All the measurements have been made after surfactant removal. Also, single gas permeability test was carried out in the apparatus described in section 2.5.1 using nitrogen, helium and propane in the transmembrane pressure range of 5 to 40 psi. Unless otherwise noted, all data presented here were obtained using a pressure difference of 10 psi.

4.3 Results

The characterization was made on the four-time coated ID-EtOH-Calcin samples to obtain information about the MS-ceramic composite membranes. Fig. 4-1 shows the SEM and EDS elemental images of cross-section view of a MS-ceramic membrane. The SEM image clearly shows the active (0.2 μm pore size) layer and the support layer of the alumina membrane. The EDS data indicate that the silicon is well dispersed throughout the membrane, suggesting that silica has been evenly incorporated into the active layer of the membrane after the four coating cycles.

Powder XRD was used to study the microstructure of the incorporated silica in the alumina support. Fig. 4-2 shows the powder XRD patterns of a four-time coated ID-EtOH-Calcin sample and a bare alumina membrane. Though the MS-ceramic membrane shows a weak and broad peak in the range of 1 – 2 ° 2θ, it was not possible to find an ordered mesopore phase from this data. This could be because the mesoporous silica is formed with a tortured orientation in the confined macropores of the support [145] or the

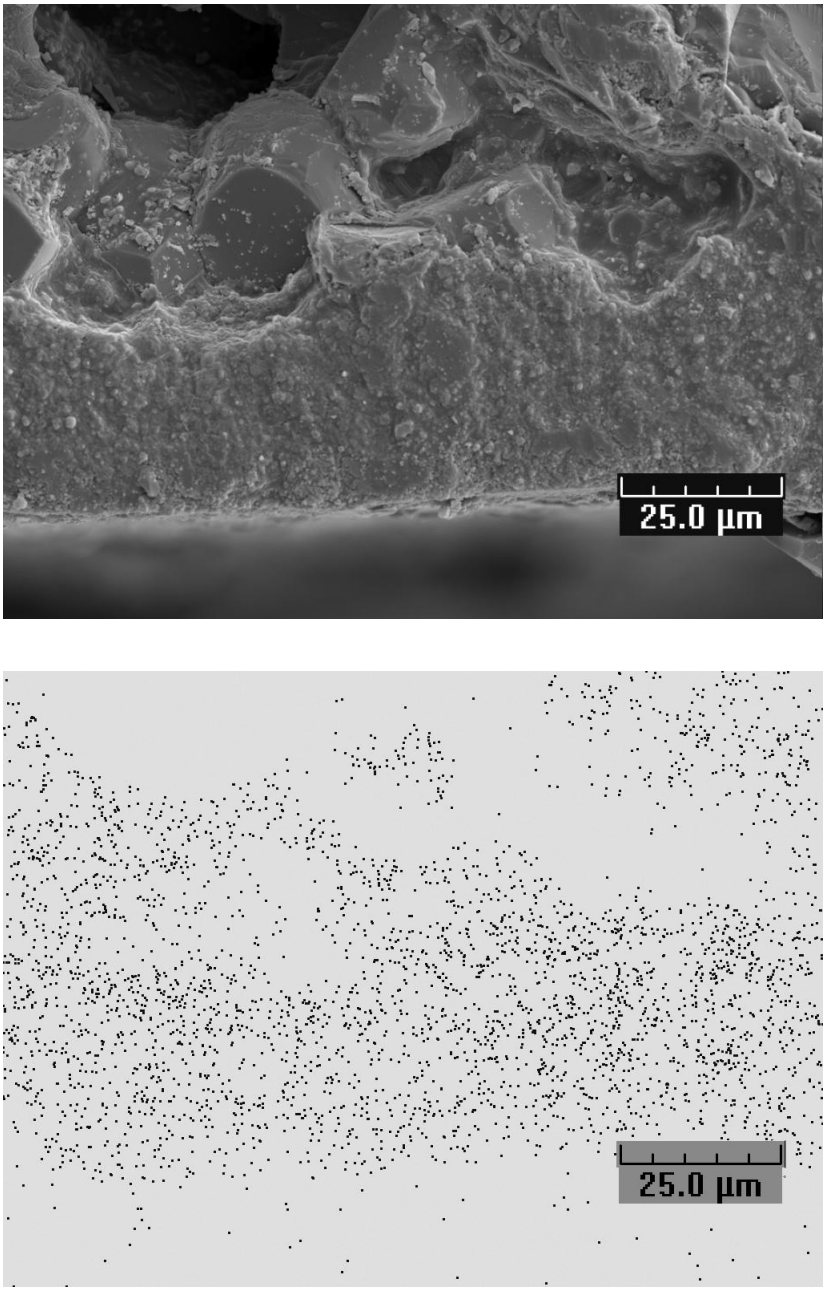

Fig. 4-1. SEM (top) and EDS (Si Kα) (bottom) images for the cross-section of a MS-ceramic membrane.

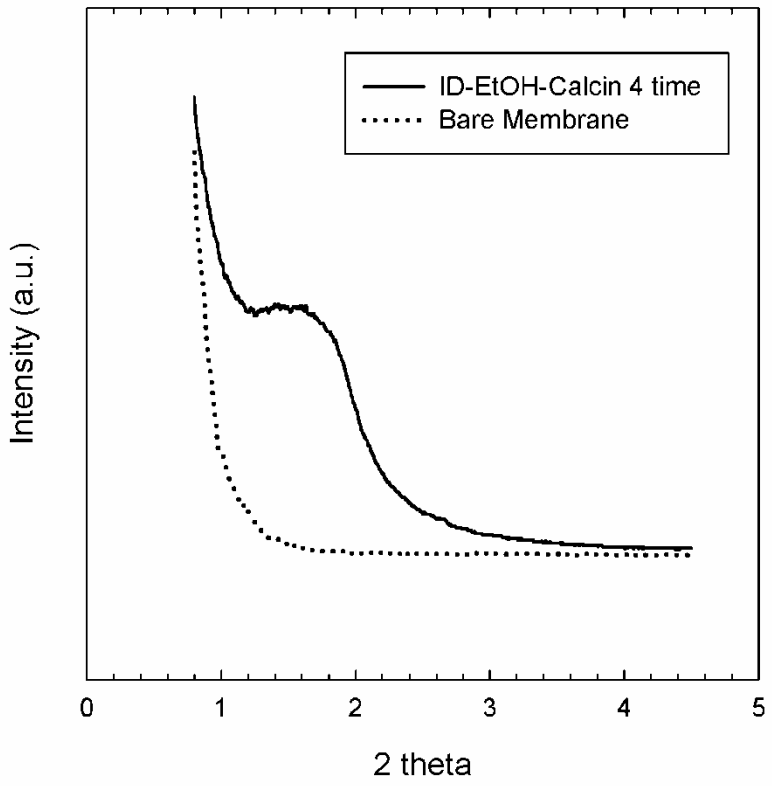

Fig. 4-2. Powder XRD patterns for MS-ceramic membrane and bare Membralox® membrane.

amount of silica phase is too small compared with the ceramic support. The diffraction data shown is qualitatively consistent with so-called 'wormhole' disordered silicas; these materials possess reasonably unifom pore sizes but have little longer range order. In a work by Xomeritakis *et al.* [144], the mesoporous silica films deposited on the alumina support did not exhibit any distinct peaks when regular XRD was employed, which was ascribed to the random orientation of the silica mesophases in the films. Yoo *et al.* [84] also did not obtain meaningful XRD peaks for OMS from composite membranes, even though the presence of ordered mesopores was evidenced by TEM and FFT (Fast Fourier Transform) processed TEM images. In this work, attempts to dissolve the alumina support and analyze the sole mesoporous silica phases have also been made by stirring membrane powders for a week in phosphoric acid or the mixture of hydrochloric acid and nitric acid, which, however, was unsuccessful due to the strong chemical stability of the Membralox® membrane.

TEM was employed for a four-time coated ID-EtOH-Calcin membrane to probe the presence of mesopores. Fig. 4-3 shows a representative TEM image of the nanocomposite. As can be seen the domains are disordered. The ordering of mesoporous silica synthesized from Brij-56 can be strongly affected by diverse factors such as the ratio of surfactant/silicate [146], acid concentration [147], and synthesis temperature [108, 148]. For example, Hayward *et al.* [108] observed a distorted 6-fold symmetric pattern in the silica phase at an aging temperature of 37 °C, cubic ($Ia\bar{3}d$) structure at 45 °C, and lamellar structure at 47 °C. Given that the mesoporous silica phases are formed in the macroporous supports that have a pore-size range of 0.2 – 10

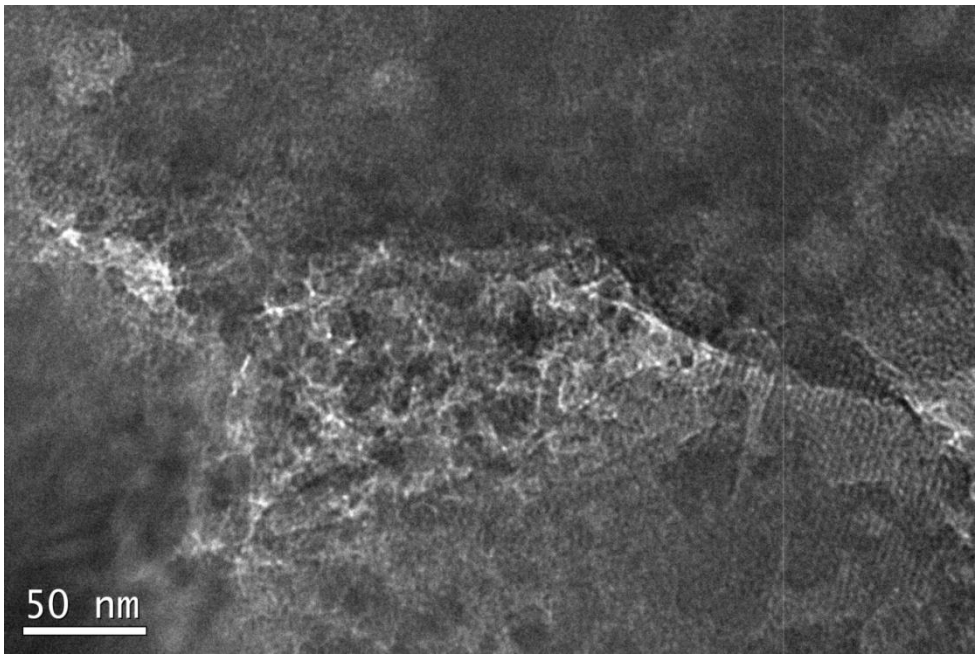

Fig. 4-3. TEM image of a MS-ceramic membrane.

μm and thickness of 1.5 mm, some inhomogeneity of the synthesis conditions during EISA may take place. Deviations from the uniform mesoporous structure have also been observed in the previous reports on OMS membranes templated by Brij-56 [84, 144, 149].

Fig. 4-4 shows a nitrogen adsorption/desorption isotherm and a pore size distribution determined by the Barrett-Joyner-Halenda (BJH) method for a four-time coated ID-EtOH-Calcin membrane. Although this isotherm exhibits a very low nitrogen adsorption, a sharp peak around 2 – 4 nm is clearly seen in the pore size distribution plot. The BET surface area and the BJH pore size of the MS-alumina membranes are about 20 m^2/g and 2.7 nm, respectively, and these values were reproducible. It should be noted that the nitrogen adsorption measurement for a bare Membralox® membrane showed the BET surface area of 0.52 m^2/g and no appreciable peak in the BJH pore size distribution. Though the silica pore sizes of 2 – 4 nm are well agreed with the previous studies on Brij-56 templated OMS [144, 146-148, 150, 151], the pore size of 2.7 nm is more or less smaller than an observation in the previous work [84] that has used the same coating solution and conditions but used only ethanol extraction to remove surfactants. This could be due to the shrinkage of mesoporous silica by high temperature calcination [149, 152], which may not occur to the solvent-extracted samples.

To check if the surface area of the MS-ceramic membrane is reasonable, the amount and the surface area of the incorporated mesoporous silica were estimated. First, OMS was synthesized and calcined without support under the same conditions as those for the MS-ceramic membranes to obtain the BET surface area of OMS (700 m^2/g).

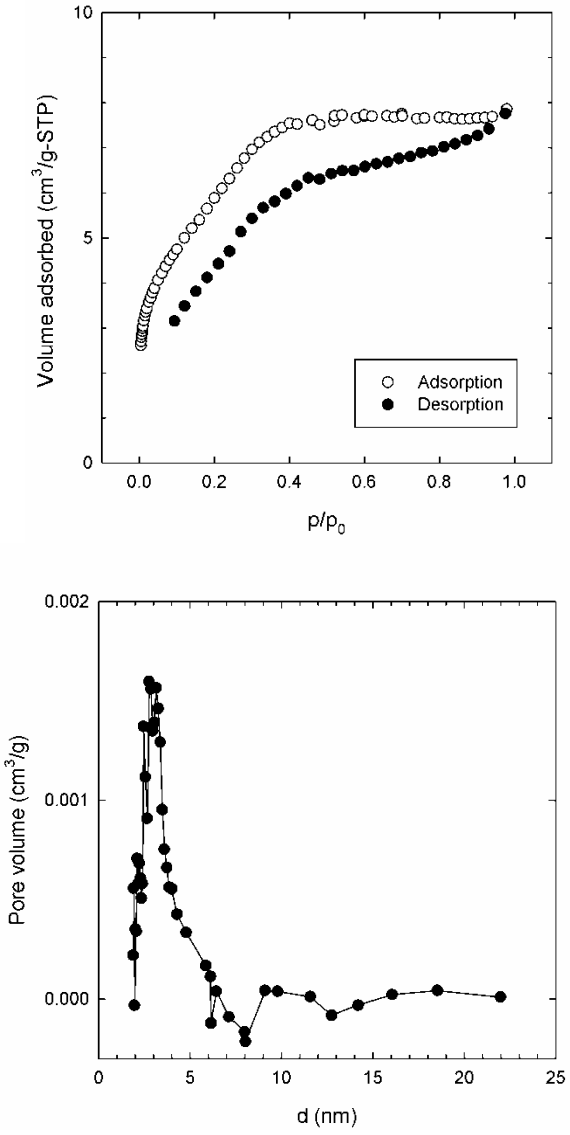

Fig. 4-4. Nitrogen adsorption/desorption isotherm (top) and BJH pore size distribution (bottom) of MS-ceramic membrane.

Next, the maximum silica loading was estimated to be 0.088 g-OMS/g-support assuming the density of the Brij-56 templated OMS and nonporous alumina as 1.1 g/cm^3 [153] and 3.92 g/cm^3, respectively. Then, the maximum surface area of the MS-ceramic membrane is calculated to be 57 m^2/g. Thus, the BET surface area of 20 m^2/g is about 35 % of the maximum surface area that can be obtained from our MS-ceramic membranes. This value is in very good agreement with the actual weight change: the weight of a membrane piece after the four coating cycles increased about 2.9 wt%, which corresponds to 33 % of the maximum silica loading. Therefore, it can be concluded that about 35 % of the pore volume of the alumina support is filled by mesoporous silica after the four coating cycles.

Fig. 4-5 shows that membrane performance depends on the methods of coating and surfactant removal. The 0.2 μm alumina support exhibits a He/N_2 selectivity of 1.94 ± 0.03 with a He permeance of 15.9 ± 0.9 mol/(sec·m^2·bar). This He/N_2 selectivity is much lower than the ideal Knudsen selectivity of 2.65, caused by the viscous flow contribution. The gas permeance in a porous layer may be given by Eq. (4-1):

$$P_m = s_1\left(\frac{4}{3}\right)\left(\frac{\varepsilon}{\tau}\right)\frac{r}{l}\sqrt{\frac{8}{\pi RT}}\frac{1}{\sqrt{M}} + \frac{1}{s_2}\left(\frac{\varepsilon}{\tau}\right)\left(\frac{r^2}{RTl}\right)\frac{1}{\eta} < p > \qquad (4\text{-}1)$$

where ε is the porosity, τ is the tortuosity, r is the mean hydraulic pore radius, l is the thickness, M is the molecular weight of a gas, η is the gas viscosity, $<p>$ is the mean pressure inside the membrane, and s_1 and s_2 are the shape factors. The first term and the second term of RHS in Eq. (4-1) account for Knudsen diffusion and viscous flow respectively. The shape factors are assumed to be $s_1 = 0.8$ and $s_2 = 2.5$ for consolidated

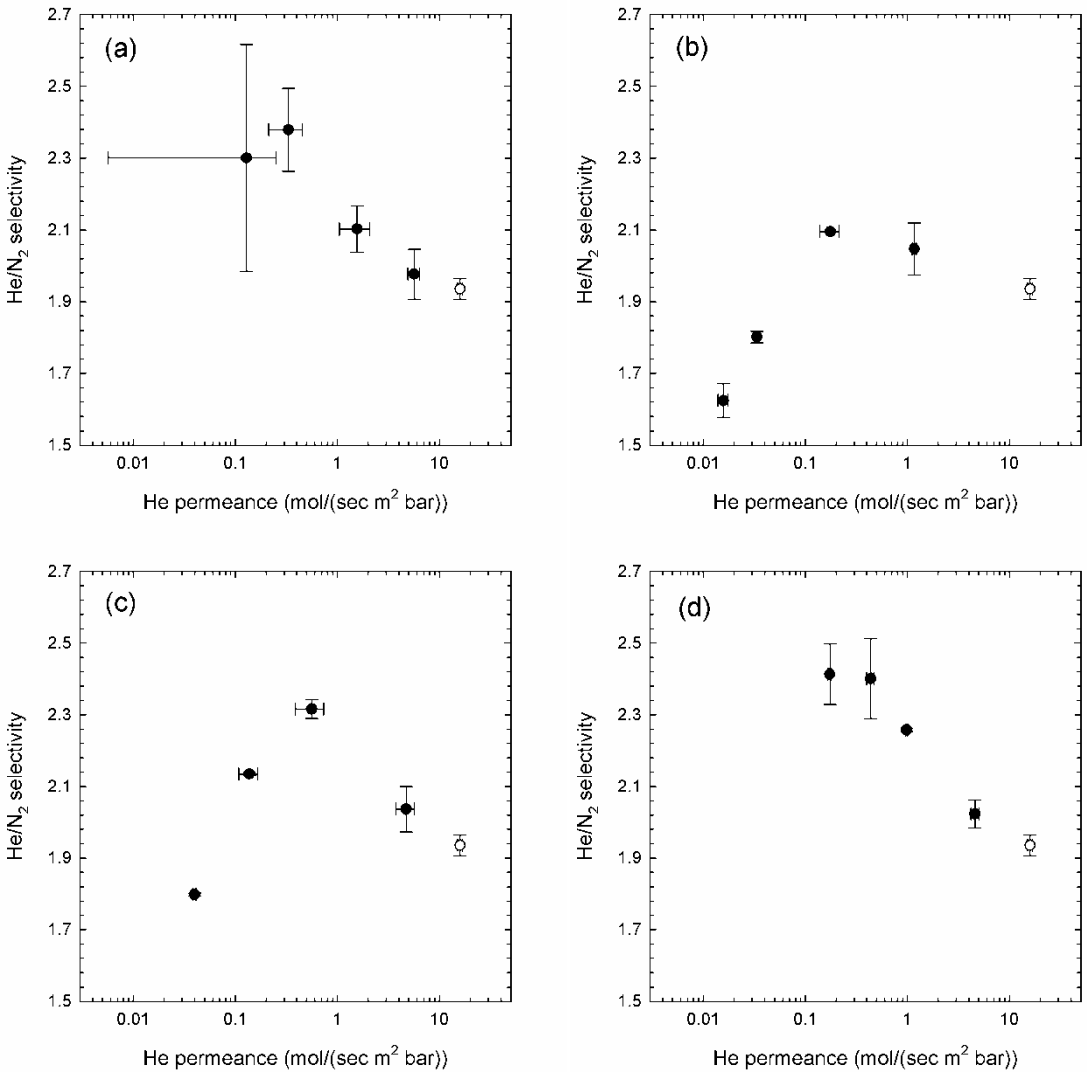

Fig. 4-5. Helium/nitrogen selectivity with nitrogen permeance for (a) SD-EtOH, (b) ID-EtOH, (c) ID-Calcin, and (d) ID-EtOH-Calcin. Blank circle and filled circles from right to left represent bare, one-, two-, three- and four-time coated membranes, respectively.

media, which have been used in many works [154, 155] since suggested by Carman [156]. The He permeance and the He/N_2 selectivity of the alumina support can be calculated from Eq. (4-1) to be 23.0 mol/(sec·m^2·bar) and 1.98 respectively, assuming ε = 0.35 [104], τ = 2.5 [157], r = 100 nm, and l = 40 μm (the active layer thickness estimated from the SEM images) at a pressure drop of 10 psi. The calculated values are in very good agreement with the experimental results, which shows that a reliable model can be obtained from Eq. (4-1) provided the parameters are reasonably assumed.

In case of mesoporous silica-coated membranes, a viscous flow contribution in Eq. (4-1) becomes negligible unless there are defects in the mesoporous silica layer. If the pore size is assumed 5 nm, Knudsen contribution reaches about 99.5 % and the He/N_2 selectivity approaches 2.62 from Eq. (4-1). However, it is observed in Fig. 4-5(a) that the He/N_2 selectivity of the SD-EtOH membranes is about 2.0 after the one dip-coating cycle. This could be understood as a result of a defective filling of the pores at the initial coating cycles [84] or by a partial loss of silica phases during ethanol extraction. The defects could be healed as the silica coating cycle is repeated, as shown in Fig. 4-5(a). The four-time coated membranes, however, show a slightly decreased selectivity with substantially large deviations in both permeance and selectivity, likely due to non-uniform filling of the pores or incomplete removal of surfactants. The selectivity drop after the multiple coatings has not been observed in the previous work [84] where anodic alumina disc membranes were used for support. This difference could be ascribed to the tortuous and interconnected pore morphology of the α-alumina membranes compared to the uniform and cylindrical pore structure of anodic alumina

membranes. Moreover, the Membralox® membrane has a very thick support layer (2 mm) while thickness of anodic alumina membranes is 60 μm, which could make the removal of surfactants from the MS-ceramic membranes more difficult.

To address this problem, inside dip-coating method was used to obtain a uniform coating layer in the 0.2 μm macropores. Fig. 4-5(b) shows the membrane performance of ID-EtOH samples. Surprisingly, the highest selectivity was obtained after the two-time coating, and after the three and four coating cycles selectivity dramatically dropped to levels even lower than that of the alumina support.

Two hypotheses have been suggested and examined to understand these results. First, defects could be responsible for this low selectivity. This looks plausible in that even small amounts of defects can have a significant effect on the selectivity when the permeance becomes very low. 0.7 μm-sized defects can cause the selectivity to drop to as low as 1.5 at a pressure drop of 10 psi. The effect of defects on permeance can be expressed by Eq. (4-2), where total permeance (P_T) is given as the sum of the permeance through the membrane (P_m) and the defects (P_d) [155]:

$$P_T = (1-\alpha)P_m + \alpha P_d \tag{4-2}$$

where α is the defect ratio (defect area/membrane area). The presence of defects results in an increase of permeance with pressure due to the viscous flow contribution. Eqs. (4-1) and (4-2) predict that for the He/N_2 selectivity of 1.6 the permeance should increase by 1.4 times for nitrogen and 1.2 times for helium as the pressure increases from 5 to 30 psi. Fig. 4-6(a) shows the normalized nitrogen permeance as a function of pressure (5 to

30 psi) for an ID-EtOH membrane. The one-time coated membrane shows a sharp increase of permeance with pressure due to the defective flow. But, for three- and four-time coated membranes the permeance was almost constant with pressure change, which disproves the hypothesis that defects caused low He/N_2 selectivity.

Another possible hypothesis is that the unremoved surfactants in the mesopores can affect the selectivity. In this case, gas transport could be partly governed by a dense region in the membrane as well as the anticipated transport through porous media. To probe this, the membranes were calcined at 500 °C for 5 h after each coating. Fig. 4-5(c) shows the results for the ID-Calcin membranes. Strikingly, although these membranes exhibited higher permeance and selectivities than the ID-EtOH samples, they still showed an abrupt drop in selectivity after the three and four coating cycles.

For a complete removal of surfactants, both ethanol extraction and calcination were performed. Fig. 4-5(d) shows that the one-time coated ID-EtOH-Calcin membranes exhibit almost the same performance as the one-time coated ID-Calcin samples, while the selectivities of multicoated membranes range between 2.3 and 2.5. These selectivities are much higher than those of the other inside dip-coated samples, but lower than the ideal Knudsen selectivity (2.65). Nevertheless, defects do not seem to be the reason for this because the nitrogen permeance of the four-time coated ID-EtOH-Calcin membranes was almost constant with pressure as shown in Fig. 4-6(b). The selectivity deviation from the ideal value is often observed even for the defect-free membranes when the gas transport resistance of the support is too large to be neglected. Xomeritakis *et al.* [144] obtained a He / N_2 selectivity of 2.43 from their 2 nm

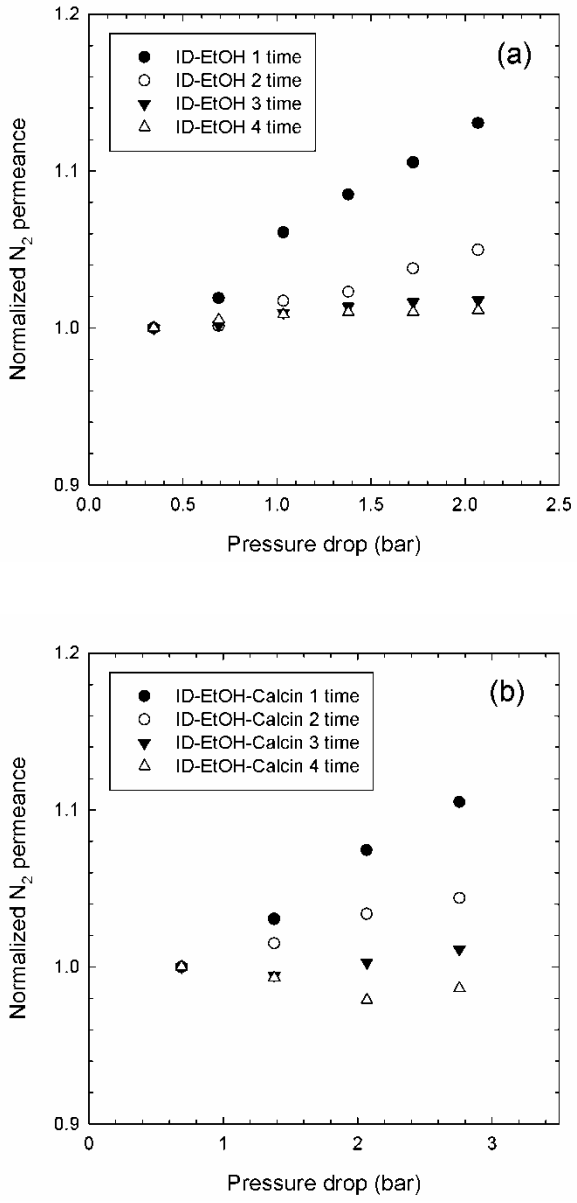

Fig. 4-6. Normalized nitrogen permeance as a function of pressure for (a) ID-EtOH membrane, and (b) ID-EtOH-Calcin membranes.

mesoporous silica-alumina membrane, which was ascribed to the effect of the support resistance. The ID-EtOH-Calcin membranes should also be considered to have strong resistance in the support layer. As stated earlier, MS-ceramic membranes have gained weight by 2.9 wt% (33 % of maximum silica loading) after the four coating cycles. This means that the thickness of the mesoporous silica layer should be at least 500 μm. However, the He permeance calculated from Eq. (4-1) assuming 500 μm thickness is 6×10^{-3} mol/(sec·m^2·bar), which is smaller by 30 times than the experimental result (0.174 ± 0.006 mol/(sec·m^2·bar)). Comparable permeance to the experimental value can be obtained when the thickness of the mesoporous layer is 10 – 30 μm. In fact, this is reasonable result considering the structure of Membralox® membrane: thickness of the active layer (0.2 μm pores) and support layer (10 μm pores) are about 40 μm and 1.5 mm, respectively. Actual thickness of the defect-free mesoporous layer, thus, may not exceed 40 μm since the film formation without defect in the coarse pores is very unlikely. Therefore, significant amounts of the mesoporous silica are likely to make new defective layers that have much smaller pore sizes than that of the coarse alumina support layer. This new-formed support layers will significantly increase the resistance, resulting in lower selectivity than the Knudsen prediction. A resistance in series approach may be used to estimate how support layer affects the permeance and selectivity [154, 158]. For example, if the pore size, the porosity/tortuosity ratio (ε/τ) and the thickness are assumed to be 2.7 nm, 0.06 (the product of (ε/τ) of OMS and alumina support) and 20 μm for the active layer, and 1.5 μm, 0.004 ($(1.5/10)^2 \cdot (\varepsilon/\tau)_{\text{alumina support}}$) and 500 μm for the support layer respectively, the pressure drop across the

support layer is each 1.9 psi for nitrogen and 3.3 psi for helium when a total pressure drop of 10 psi is applied (gas flow through the mesoporous silica phases in the support layer can be neglected since the contribution of this region is less than 1 % of the total flow through the support layer). This results in the He permeance of 0.17 mol/(sec·m^2·bar) and the He/N_2 selectivity of 2.35, quite comparable values to the experimental results (Appendix A).

Propane permeance experiments were also performed on the ID-EtOH-Calcin membranes to check for diffusion effects (Fig. 4-7). The one and two coating cycle membranes show a drop in their propane/nitrogen selectivity. However, the C_3H_8/N_2 selectivity abruptly increases with additional coating cycles. This tendency can be explained by the change of the gas transport mechanism: i.e. as the coating cycle is repeated, Knudsen contribution (C_3H_8/N_2 = 0.8) becomes more and more dominant compared to the Poiseuille (viscous) flow (C_3H_8/N_2 = 2.16 in ambient condition), and the surface diffusion is significantly enhanced with an increase of surface area. This result suggests that the thickness of the mesoporous silica layer affects the surface flow. Also, it should be noted that the four-time coated membranes that exhibited low He/N_2 selectivity showed C_3H_8/N_2 selectivities between 1.2 and 1.5, which implies that the high selectivity of the four-time coated ID-EtOH-Calcin membranes is not caused by the unremoved surfactant, but by clean silica pore surfaces.

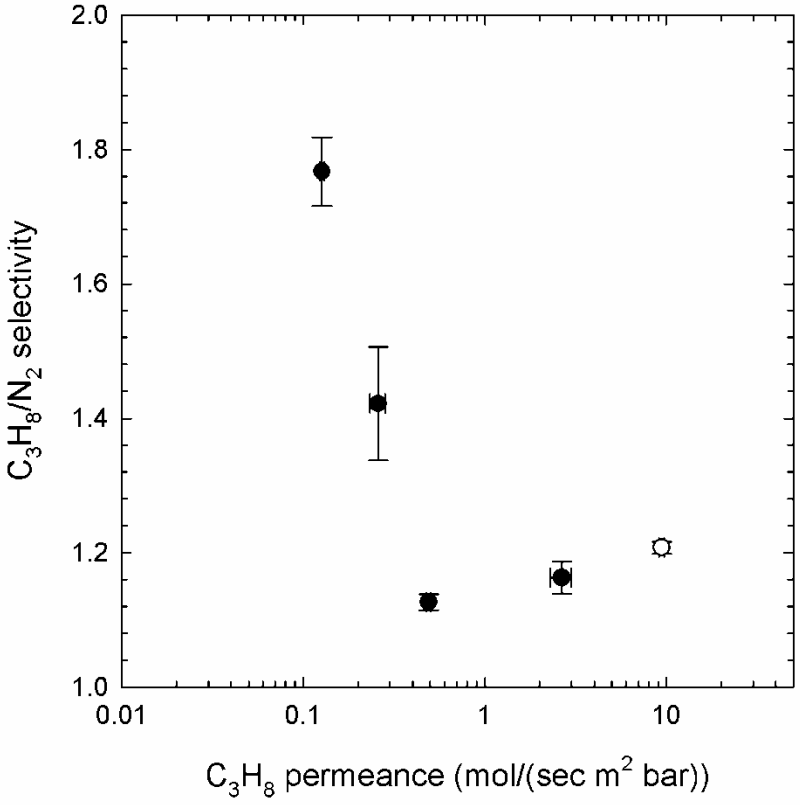

Fig. 4-7. Propane/nitrogen selectivity with propane permeance for ID-EtOH-Calcin membranes. Blank circle and filled circles from right to left represent bare, one-, two-, three- and four-time coated membranes, respectively.

4.4 Conclusions

Mesoporous silica (MS)-ceramic membranes have been synthesized using multiple cycle conventional dip-coating or inside dip-coating method. Although diffraction methods indicate the absence of long-range order, uniform mesopore phases could be observed by TEM and nitrogen adsorption. Membrane permeance test showed an interesting behavior depending on the coating and solvent-removing methods. The MS-ceramic membranes prepared by dip-coating exhibited a large variance in both permeance and selectivity as the coating cycle is repeated. As to the membranes synthesized by inside dip-coating, multiple coating cycles resulted in an unexpected low He/N_2 selectivity, which could be ascribed to the effect of the unremoved surfactants. Strikingly, this organic moiety could not be thoroughly removed even by calcination at 500 °C for 5 h, and it was demonstrated that after using combined methods of solvent extraction and calcination clean MS-ceramic membranes can be obtained. These membranes provided defect-free properties with moderately high permeance.

CHAPTER V

SURFACE-MODIFIED ANOPORE™ MEMBRANES FOR PROTEIN MICROFILTRATION *

5.1 Introduction

Anodized aluminum oxide (AAO) membranes are frequently used for many applications due to their cylindrical macropores that have a very narrow pore size distribution. Anopore™ alumina membranes are one class of commercially available and heavily studied AAO membranes [159, 160]. In the current work they should serve as an excellent membrane support for protein filtration, for they are expected to exhibit high reproducibility in flux behavior and thus in a sense are model ceramic membranes for studying protein fouling. In the current work the synthesis, characterization, and fouling behavior of a series of Anopore™-organic hybrid membranes are reported. It was anticipated that by integrating the uniform pore size of the underlying ceramic membrane with designed organic layers protein fouling could be ameliorated. This is in fact observed and the results point to the potential of designing hybrid membranes that could have potentially superior properties to either purely ceramic or purely polymeric membranes.

---

* Reprinted with permission from "The effect of surface modifications on protein microfiltration properties of Anopore (TM) membranes" by S. Yeu, J. D. Lunn, H. M. Rangel, and D. F. Shantz, J. Membr. Sci. 327 (2009) 108-117. © 2009 by Elsevier B.V.

Bowen and Gan [65] studied BSA filtration through aluminum oxide membranes with a mean pore size of 0.22 μm, and suggested that the pore constriction model explained the observed flux decline. This implies that the surface properties may play a critical role in reducing fouling. Given the relative complexity of the membranes investigated here, it was decided to follow simple modeling approaches, which nonetheless lead to reasonable physical insights about the system.

5.2 Experimental

Amine, Pluronic, and PEG functionalized membranes were synthesized respectively, and the detailed procedures are described in the section 2.3 and Fig. 2-4. Given the numerous functionalization schemes used Table 5-1 summarizes the different samples made and sample abbreviations that will be used throughout.

Characterization of the membranes and analysis of the organic moiety were performed by FE-SEM, XPS, IR and TGA. The particle size of BSA was measured using light scattering. More information about the analysis is given in section 2.6.

Fouling behavior was studied by protein filtration test (section 2.5.2). Flux decline during filtration monitored to determine the fouling model and fouling parameters. Normalized flux plots were calculated by differentiating the filtrate and normalizing them by the initial flux.

Table 5-1. Composite membrane samples and the abbreviations used in the text to denote them. Gx refers to a dendrimer of generation x.

Composite Membrane	**Abbreviation**
Amine functionalized alumina membrane	AAM
Amine functionalized silica-coated membrane	ASM
OTS-Pluronic coated membrane	PCM
Amine-PEG functionalized membrane	APM
Dendrimer (Gx) functionalized membrane	DGxM
PEG-Dendrimer (Gx) functionalized membrane	PDGxM

5.3 Results

The functionalized membranes showed more or less lower initial flux than bare membranes. While the initial flux of amine-functionalized membranes did not show significant changes, a large decrease of initial flux was observed in case of Pluronic and PEG-functionalized membranes. For completeness Table 5-2 shows the initial flux data for the various samples analyzed.

5.3.1 Amine-Functionalized Membranes

Fig. 5-1 shows FE-SEM images of the parent Anopore^{TM} membranes and a silica-coated amine-functionalized membrane. As can be seen from the images, the silica coating does not dramatically alter the pore size as the walls of the pores appear very similar, if not slightly thicker, than the walls of the parent membrane. Hydraulic permeability measurements indicate the mean pore size decreases from 242 to 236 nm upon silica coating. Fig. 5-2 shows the XPS data for the bare, amine-functionalized (AAM), and silica-coated amine functionalized Anopore^{TM} (ASM) membranes. The XPS data shows that, as expected, there is in an increase in the carbon, nitrogen, and silica present on the surface after membrane functionalization. The XPS data also indicates, at least qualitatively, that the amine-grafting step is more efficient after the membrane has been silica-coated. While it is tempting to draw quantitative conclusions from C/N ratios determined by XPS, in our hands this seems suspect. As an example we show data in Fig. 5-3 that both the bare membranes and silica - coated membranes have

Table 5-2. Initial fluxes for various samples determined in membrane testing.

Membrane sample	**Protein**	J_o **(m/h)**
Anopore	BSA	1.82
AAM	BSA	1.79
ASM	BSA	1.73
Anopore	LSZ	1.65
AAM	LSZ	1.77
ASM	LSZ	1.62
PCM (M:W 0:1)	BSA	1.38
APM (2mM)	BSA	1.16
PDG1M (1mM)	BSA	0.82
PDG1M (2mM)	BSA	0.94

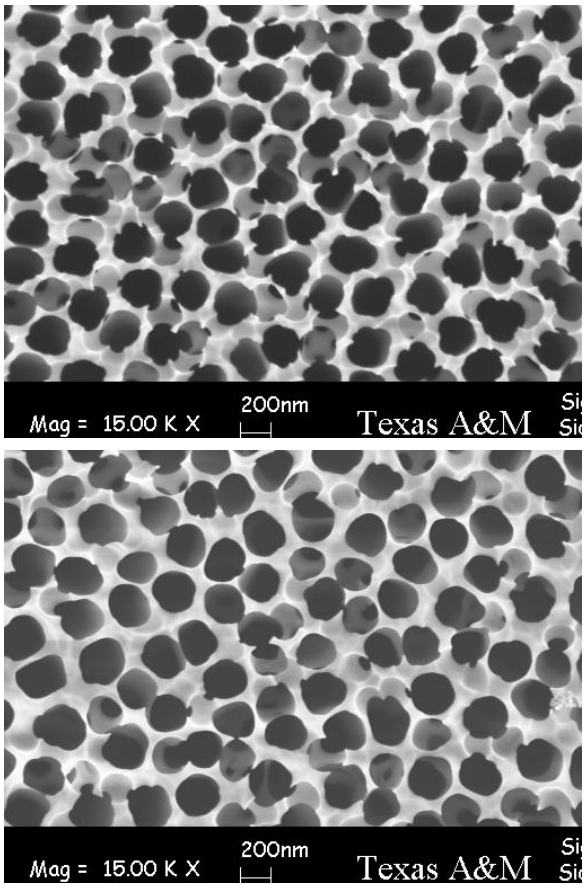

Fig. 5-1. FE-SEM images of (top) Anopore^{TM} and (bottom) silica-coated amine-functionalized Anopore^{TM} membranes.

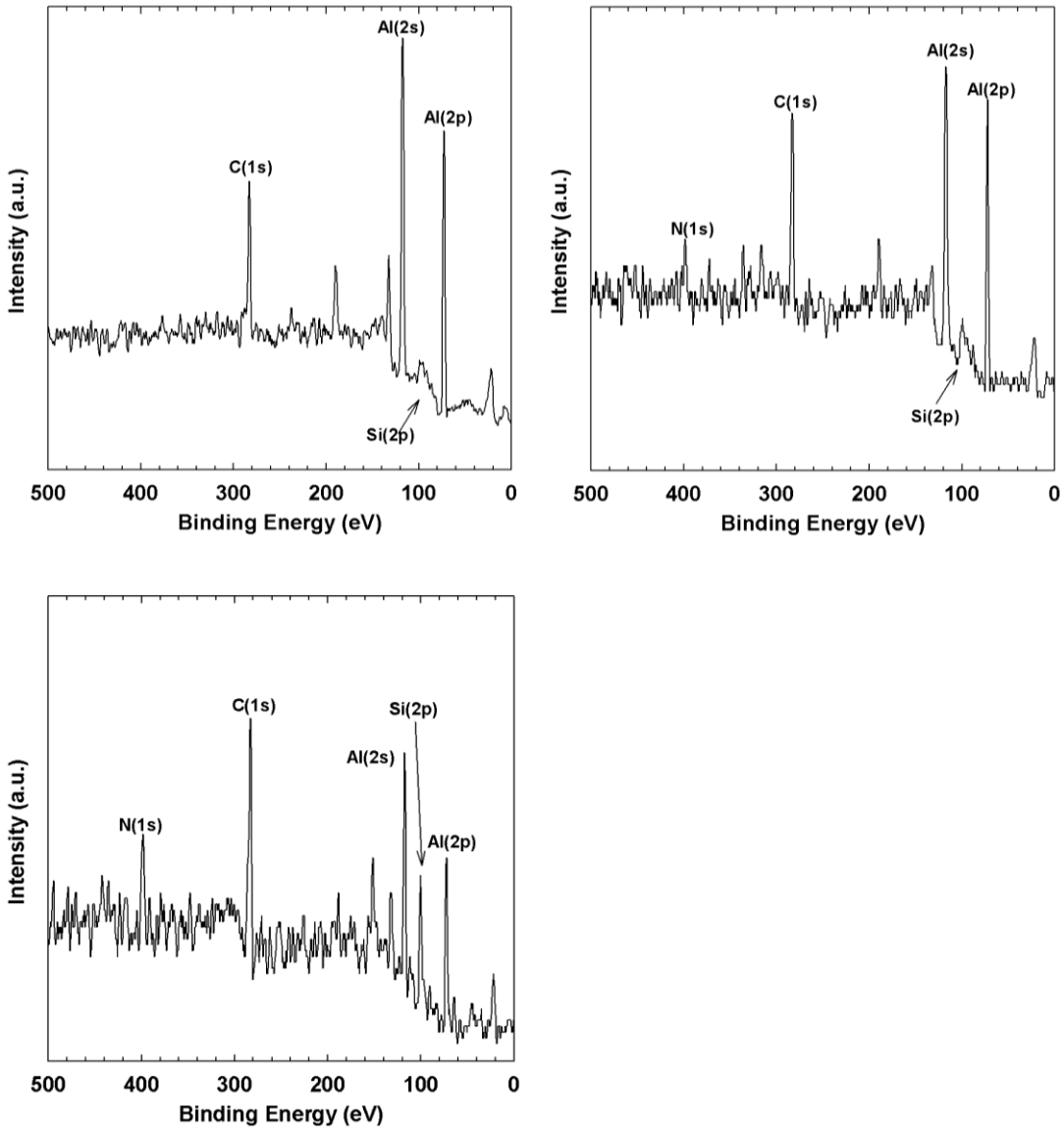

Fig. 5-2. X-ray photoelectron spectroscopy (XPS) results for (from top left and right to bottom) Anopore^{TM} membrane, amine-functionalized Anopore^{TM} membrane (AAM), and silica-coated amine-functionalized Anopore^{TM} membrane (ASM).

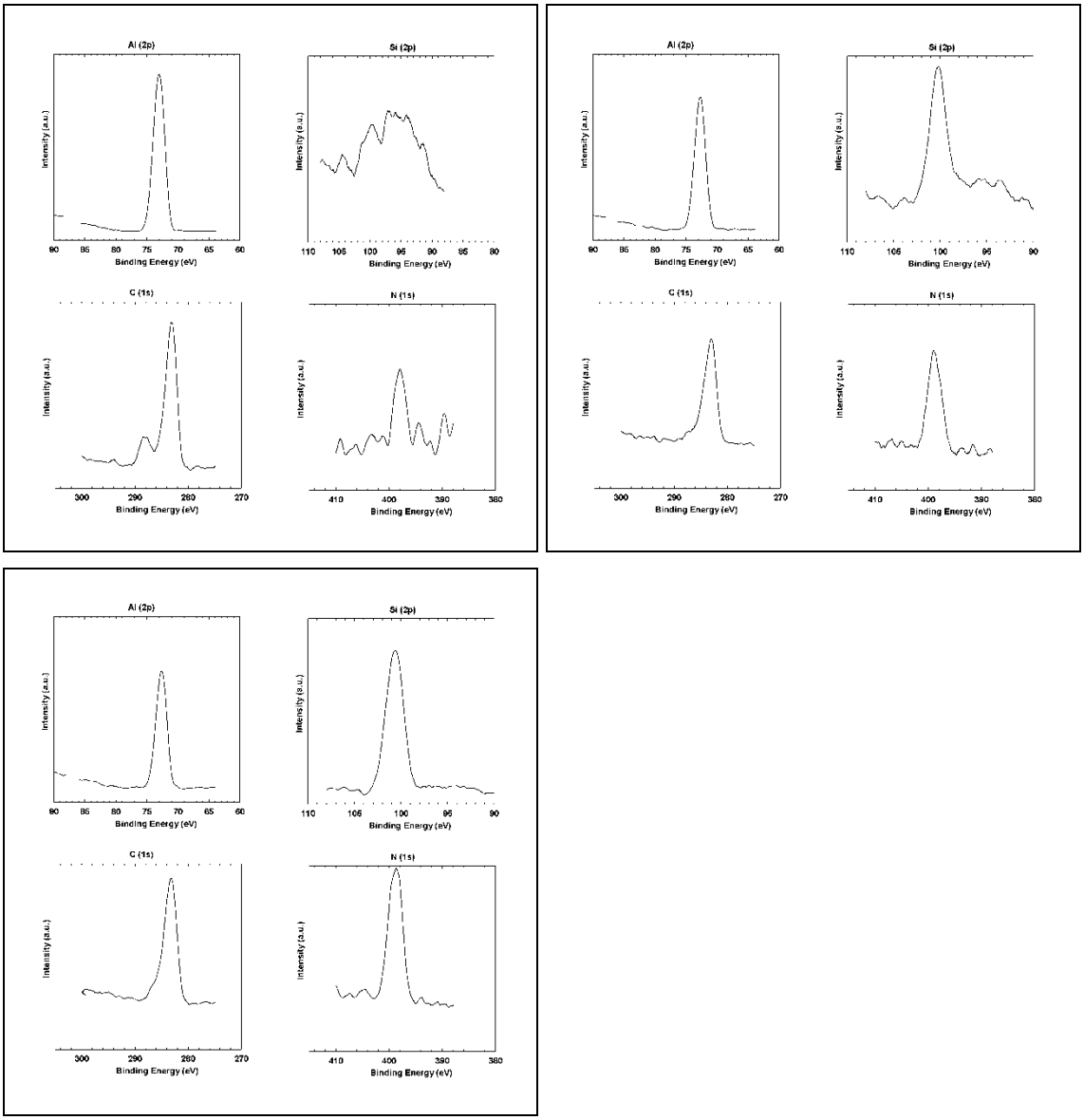

Fig. 5-3. High resolution XPS scans of (from top left and right to bottom) Anopore^{TM} membrane, amine-functionalized Anopore^{TM} membrane (AAM), and silica-coated amine-functionalized Anopore^{TM} membrane (ASM).

non-trivial amounts of residual carbon on them. Thus, attempting to draw quantitative conclusions from the C/N ratios seems unwarranted.

Fig. 5-4 shows the normalized flux data from microfiltration experiments of Bovine Serum Albumin (BSA) and Lysozyme (LSZ) over amine-functionalized membranes. Several conclusions can be drawn from this figure. The lysozyme flux for the bare membrane shows a more significant decline than BSA, which is reasonable considering low isoelectric point of Anopore^{TM} membranes (pH ~ 4) [42]. For the amine-functionalized alumina membranes (AAM) the flux data are nearly identical to those for the bare alumina. This is consistent with the XPS and IR results that indicate that the amine functionalization of the alumina surface is inefficient. By contrast clear differences can be observed between the bare Anopore^{TM} membrane and the membranes that were silica coated and then amine functionalized (ASM). For these samples the BSA flux decreases compared to the bare membrane and the LSZ flux increases compared to the bare membrane. This result is consistent with electrostatic effects, as the pI values of BSA and LSZ are 4.7 and 11.0 respectively [161]. Thus, even for this case of simple amine functionalization, the results indicate that significant changes in the flux behavior (+/- 30%) can be realized by modifying the surface chemistry of the alumina membrane.

IR spectroscopy was used to study the composite surface after the microfiltration measurements. Fig. 5-5 shows the IR spectra of the materials after microfiltration and is consistent with the flux data in Fig. 5-4. Consider the membranes used in the BSA microfiltration tests, which showed a decreased flux upon amine functionalization. The

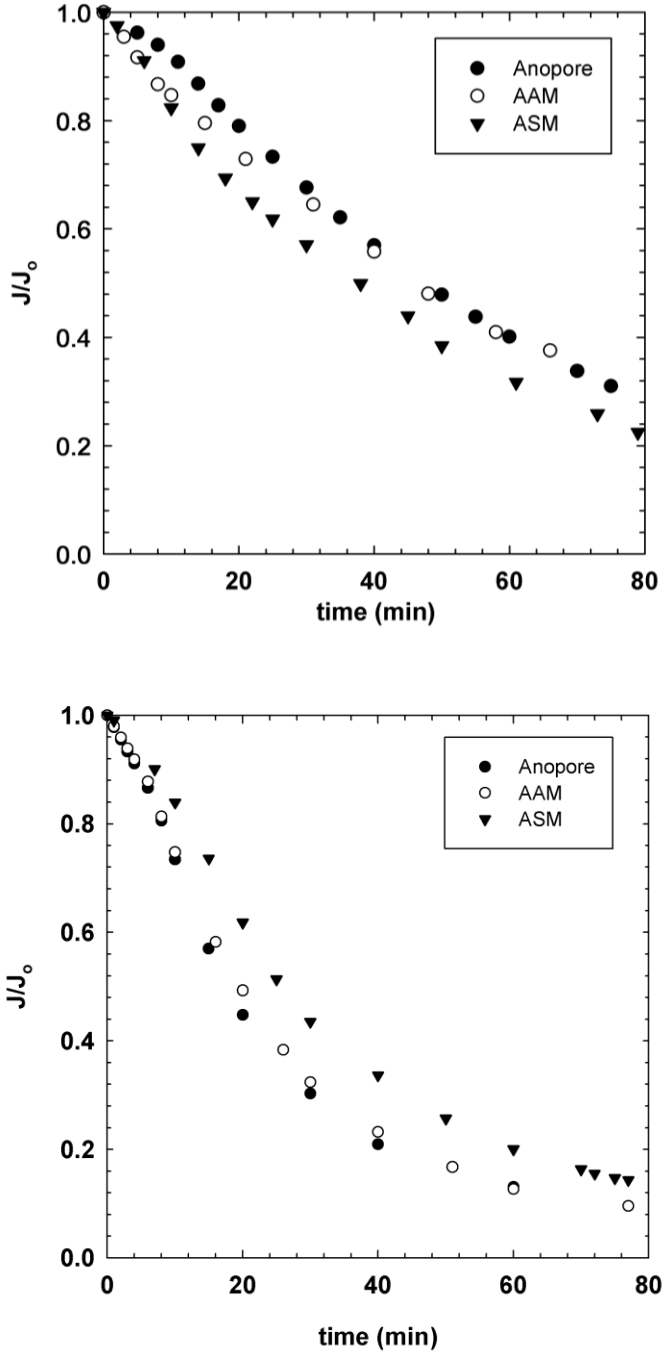

Fig. 5-4. Normalized filtrate flux versus filtration time for (top) BSA and (bottom) LSZ. Anopore^{TM}-ATS and Anopore^{TM}-SiO_2-ATS are amine-functionalized (AAM) and silica-coated amine-functionalized membranes (ASM), respectively.

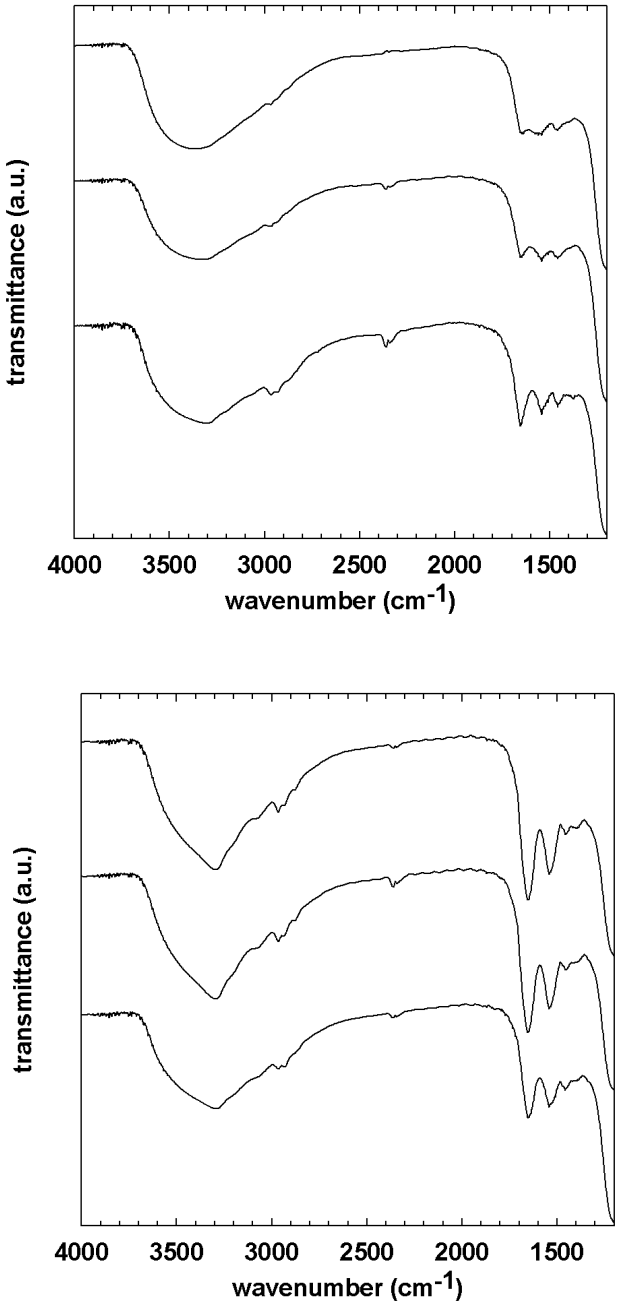

Fig. 5-5. IR spectra of membranes after microfiltration testing, (top) BSA and (bottom) LSZ. For both figures the spectra correspond (from top to bottom) to the bare membrane, the amine-functionalized membrane (AAM), and the silica-coated amine-functionalized membrane (ASM).

materials exhibit stronger absorption bands in the amide I (1665 cm^{-1}) and amide II (1550 and 1500 cm^{-1}) regions, and C-H and N-H stretching regions (~2980 and ~3300 cm^{-1}) as compared to the parent membranes [162]. This result is consistent with more protein deposited on the amine-functionalized silica coated membranes which is consistent with the flux data. By contrast, the silica-coated amine-functionalized membranes used in the LSZ microfiltration measurements have weaker absorption bands in the amide I and II regions, again consistent with the microfiltration measurements.

5.3.2 Pluronic-Functionalized Membranes

Membranes were also investigated wherein Pluronic F108 was deposited on the surface via hydrophobic interactions between the PPO block and octadecyl (OTS) groups grafted to the membrane surface (samples denoted as PCM). Fig. 5-6 shows the flux data for BSA for the F108-OTS-Pluronic functionalized nanocomposite membranes. The key conclusion is that the F108 modified membranes display reduced fouling as compared to the bare alumina membranes. This can be explained due to the PEO blocks reducing (though not eliminating) non-specific protein adsorption. However, perhaps surprisingly the flux data appear relatively insensitive to the solution deposition conditions; this could be indicating that the effective Pluronic adsorption is quite low. The effective pore size determined by permeation is 226 nm. This is discussed in more detail below (*vide infra*). Samples were also analyzed where two Pluronic dip coating cycles were performed; essentially no differences were seen in these materials based on IR and XPS.

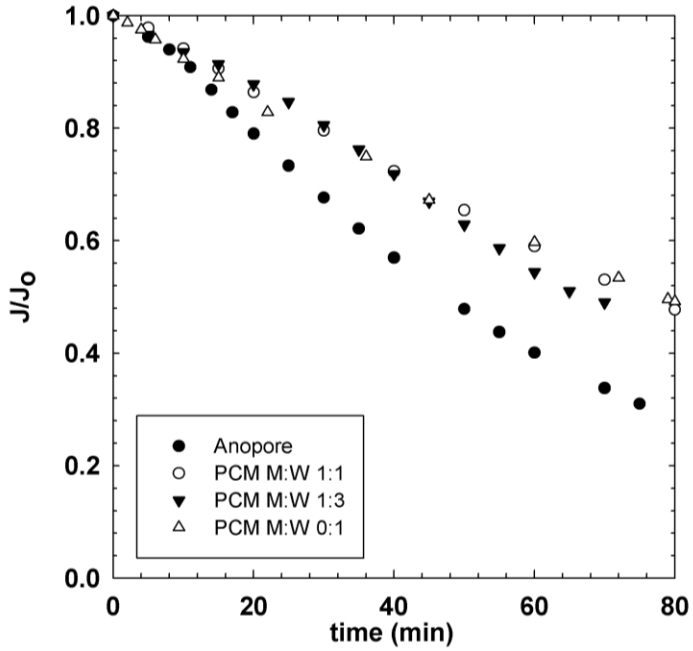

Fig. 5-6. Normalized filtrate flux as a function of filtration time for a series of F108-OTS Anopore^{TM} composite membranes (PCM) as well as the parent Anopore^{TM} parent membrane for comparison. The M:W ratio cited in the figure legend indicates the methanol:water ratio of the Pluronic dip coating solution.

An additional point of note is that when one tries to deposit Pluronic F108 from methanol rich mixtures (methanol:water > 1:1) the initial flow rates are very low compared to the other membranes. This can be understood by looking at the flow rate test results in Fig. 5-7. Fig. 5-7 shows the observed initial flow rates of water and ethanol through Anopore^{TM} and PCM membranes as a function of pressure. For the membrane where the Pluronic deposition was performed at a methanol:water ratio of 3:1, water could not penetrate at all through the OTS-modified membrane until 15 psi of pressure drop, whereas ethanol easily flowed through this membrane. This can be explained by the inability to deposit Pluronic on the OTS-functionalized membrane in methanol, which results in a highly hydrophobic (and hence poorly wetted) surface.

Further evidence for this is obtained from IR (Fig. 5-8) and TGA (Table 5-3) data of the samples. Regarding the IR data, by comparison with the parent Anopore^{TM} membrane, the presence of OTS is evident as OTS has two sharp C-H stretching bands at 2920 and 2850 cm^{-1}. The presence of F108 is manifested by the broadening of bands at 2900 cm^{-1}, due to the C-H stretching band of the Pluronic. This broadening decreases as the methanol:water ratio increases. The increase in absorption intensity between the two OTS peaks is consistent with an increase in the amount of deposited F108. The thermogravimetric analysis results shown in Fig. 5-9 and Table 5-3 are consistent with the interpretation of the IR data and the trends in the fouling data and initial flow rates. The data in Table 5-3 focus on the temperature range of 403 – 503 K since over 99% of F108 decomposes in this range. The membranes where Pluronic was deposited from methanol rich solutions (methanol: water of 1:1 or greater) show very similar weight loss

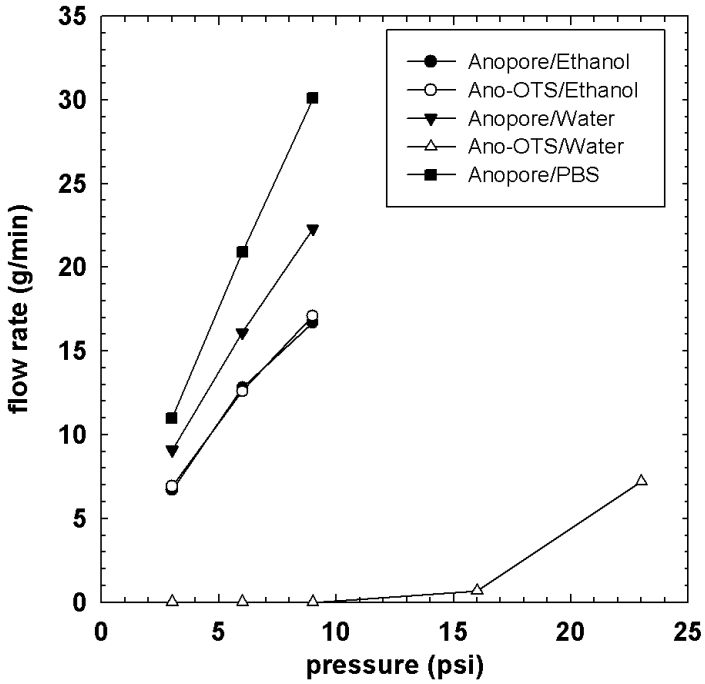

Fig. 5-7. Initial flow rate versus pressure for Anopore™ and OTS Pluronic-functionalized Anopore™ membranes (PCM).

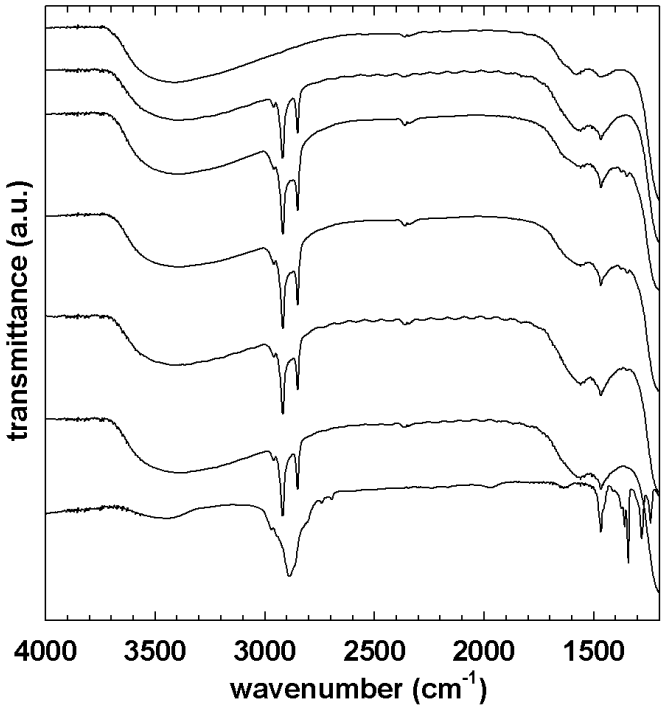

Fig. 5-8. IR spectra of the OTS-F108-Anopore™ composite membranes before microfiltration testing. From top to bottom: Anopore™ membrane, OTS-Anopore™ membrane, OTS-F108 composite membranes (PCM) prepared using methanol:water ratios of 0:1, 1:3, 1:1, 3:1, and pure Pluronic F108.

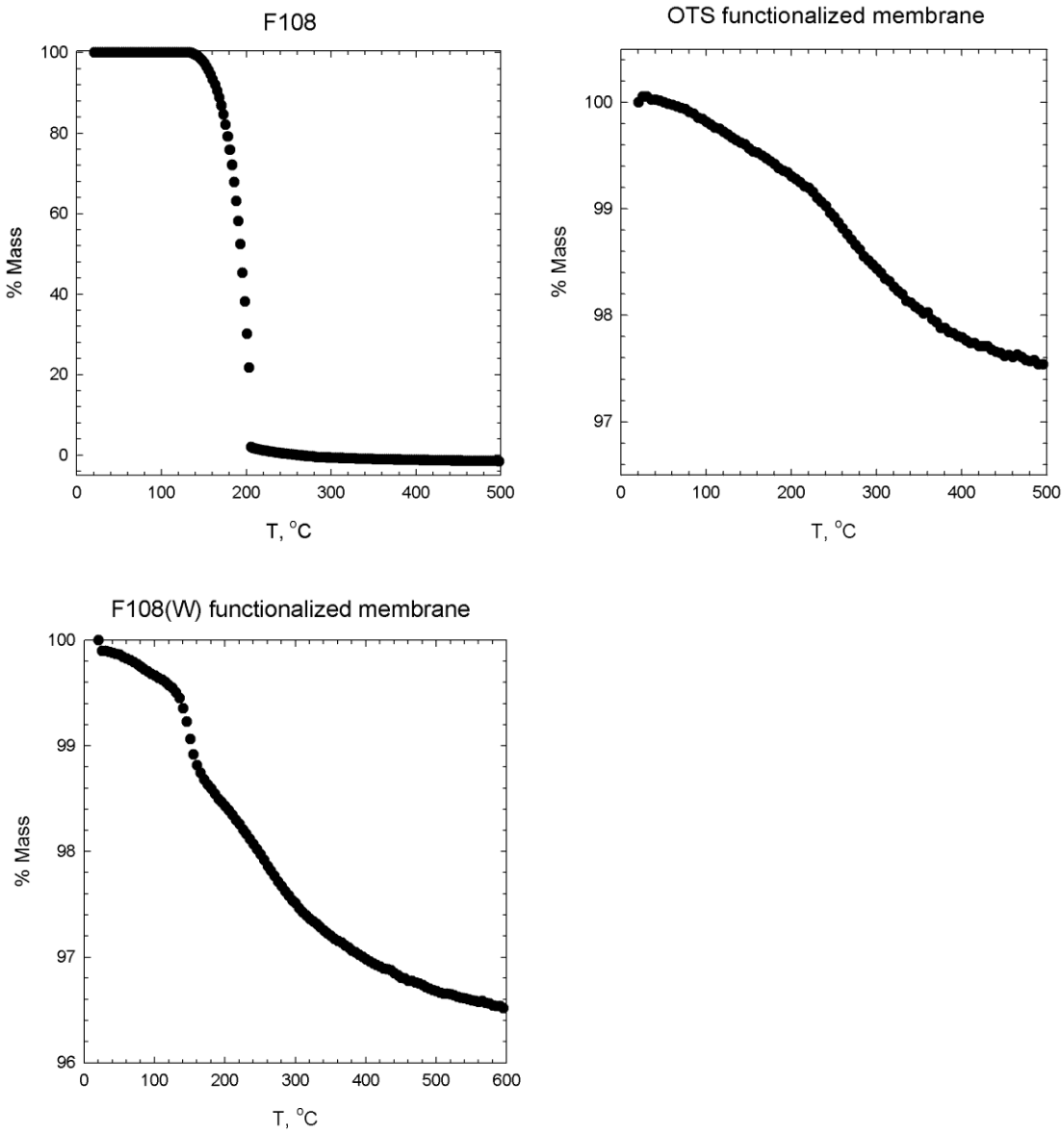

Fig. 5-9. TGA data for (from top left and right to bottom) Pluronic F108, OTS-Anopore^{TM} membrane, and OTS-F108 (W) Anopore^{TM} membrane.

Table 5-3. Summary of the TGA data over the temperature range of 403 – 503 K for the OTS-Pluronic / Anopore^{TM} nanocomposite membranes (PCM). Ratio in parentheses in the left column indicates the methanol:water ratio used in the Pluronic deposition step.

Membrane sample	Percent Weight Loss
OTS	0.58
PCM (1:0)	0.62
PCM (3:1)	0.61
PCM (1:1)	0.97
PCM (1:3)	1.22
PCM (0:1)	1.34

to the OTS-functionalized membranes without any Pluronic deposited on them. This similarity is consistent with the data in Fig. 5-7 that showed that these membranes had poor wettability. Perhaps most significant, however, is that an effective Pluronic loading of approximately 0.7 weight percent leads to a substantial decrease in fouling. Previous work has shown that the surface area of an Anopore^{TM} membrane with 200 nm pores is approximately 7.5 m^2/g [159]. This number, when coupled with the weight loss determined by TGA results in the estimate that on average there are approximately 1 mg/m^2 of Pluronic adsorbed on these membranes. This number is at the low end of the range reported in a study by Schroen and coworkers [163] which reports between 2 – 1.5 mg/m^2 of Pluronic F108 adsorbed on hydrophobic modified silica surfaces. Thus, while in the current work the surface is likely not at saturation coverage, a significant reduction in fouling is nonetheless observed. Finally, PCM samples were rinsed with 2 L of DI water and reanalyzed using IR and XPS. This data, as given in Fig. 5-10, shows no discernable differences in the samples before and after rinsing. Thus, at least by this test, the deposited Pluronic appears to remain on the membrane.

5.3.3 PEG-Functionalized Membranes

In an effort to increase the loading of EO groups PEG was covalently attached to the surface [58, 59, 164]. Two approaches were taken. The first was simply to expose a silica-coated amine functionalized membrane to an mPEG solution (APM). The second

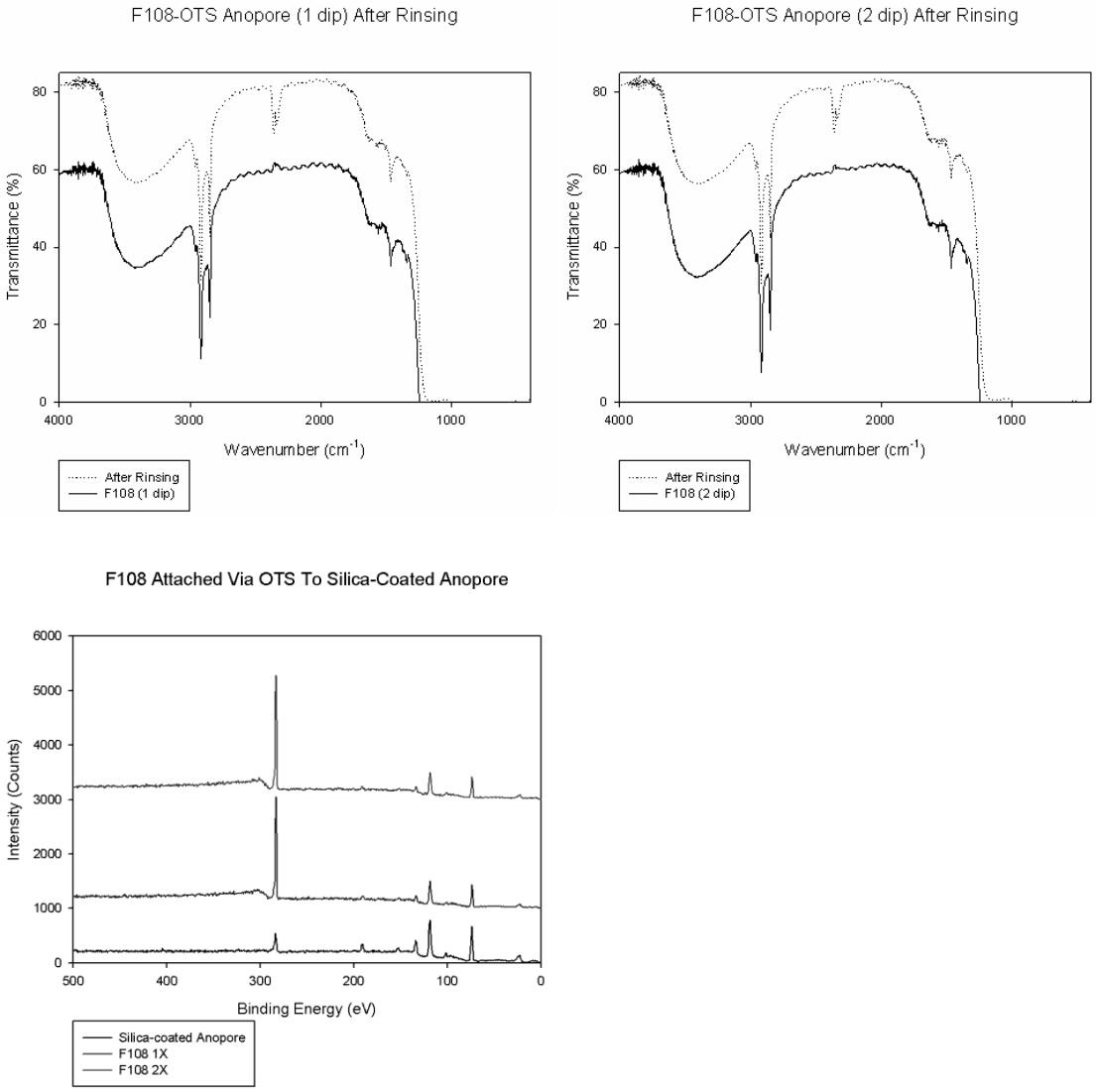

Fig. 5-10. Top - IR showing PCM samples before and after rinsing with 2 L of DI water (left) 1 time coated, and (right) 2 time coated. Bottom - XPS results of (from bottom to top) silica coated membrane, PCM one time dip coating and PCM two time dip coating.

was to grow melamine dendrons from the surface of a silica-coated amine-functionalized membrane and react mPEG with the peripheral amine groups of the dendron (see Fig. 2-4, PDGxM). Fig. 5-11 shows BSA filtration data for these membranes. As can be seen there is a significant decrease in membrane fouling for these materials as compared to the bare Anopore^{TM} membranes. Particularly for the membranes functionalized using 2 mM mPEG solutions, there is a significant improvement in the flux properties over the 80 minute period measured. The membranes functionalized with 2 mM PEG solutions exhibit less fouling than the best OTS-F108 composite membrane (PCM samples). The PDG1M (2 mM) membrane shows the greatest reduction in fouling. However, the APM membrane displayed less fouling than the PDG1M membrane with less (1 mM) mPEG even though the amounts of bound mPEG should be similar for the two membranes. One possible explanation is that some unreacted amines on the G1 dendron result in electrostatic interactions with the BSA leading to increased fouling. Permeability measurements indicate the effective pore sizes of these membranes are 218 nm (APM, 2 mM), 198 nm (PDG1M, 1 mM), and 206 nm (PDG1M, 2mM).

Fig. 5-12 shows the IR data for the pegylated samples. The IR data is consistent with PEG being successfully grafted onto the surface based on the C-H stretching bands at ~2900 cm^{-1}. For the PEG capped dendron samples (PDG1M), another feature is observed at ~1550 cm^{-1} due to the C-N stretches of the triazine ring. The increasing intensity of the bands at ~2900 cm^{-1} is qualitatively consistent with increased PEG on the surface and correlates well with the filtration data shown in Fig. 5-11.

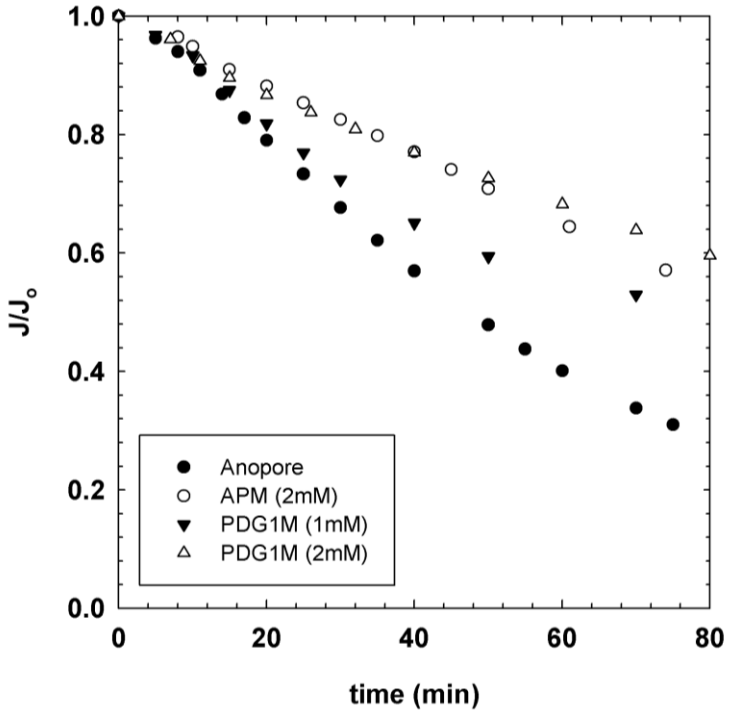

Fig. 5-11. Normalized filtrate flux as a function of filtration time for a series of pegylated Anopore™ composite membranes as well as the parent Anopore™ parent membrane for comparison.

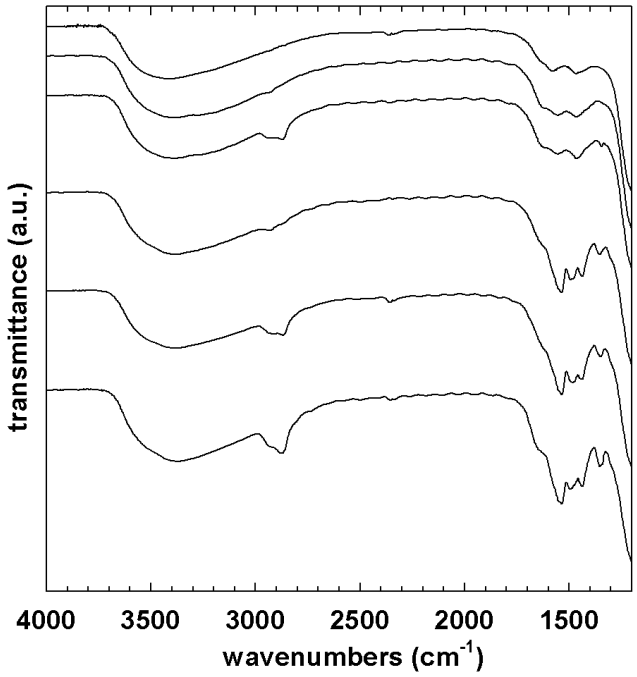

Fig. 5-12. IR spectra of PEG-functionalized membranes. From top to bottom Anopore™ membrane, ASM, APM, DG1M, PDG1M (1 mM), and PDG1M (2 mM).

5.3.4 Modeling of the Filtration Measurements

Model fitting was performed on flux data to understand which fouling mechanism is present in our microfiltration system. Fig. 5-13 shows the experimental data and fitting (solid lines) of BSA filtration through the bare Anopore^{TM} membranes using the equations for the four models in Table 1-1. The results indicate that the pore constriction model fits the data most satisfactorily (R^2 = 0.997) over the range of data obtained. An explanation for this was found from the BSA particle size measurements using dynamic light scattering before and after the filtration test (Fig. 5-14). BSA solutions exhibited distinct bimodal particle size distributions both before and after the filtration, which shows the presence of BSA monomer and aggregates. While in our measurements the particle sizes of monomeric BSA were constant (6 – 13 nm), BSA aggregates after filtration showed significant reduction in size (20 – 40 nm) compared with the aggregate size of 35 – 80 nm before filtration, and this pattern was reproducible. This result is not in agreement with the previous reports from Zydney's lab [39, 55]. Although they also obtained bimodal particle size distribution of BSA using light scattering, two studies reported different aggregate sizes (200 – 400 nm [55] and 100 – 1000 nm [39]) with much higher intensity of aggregates than our data. This could be because aggregation formation of BSA is susceptible to severe mixing condition, since, in this study, BSA was dissolved in PBS very gently without vortex. Two observations can be made from the DLS results. First, protein aggregates larger than the pore size of the membranes were not observed before filtration although clearly aggregates are present. This observation explains the absence of complete pore blocking. Second, the

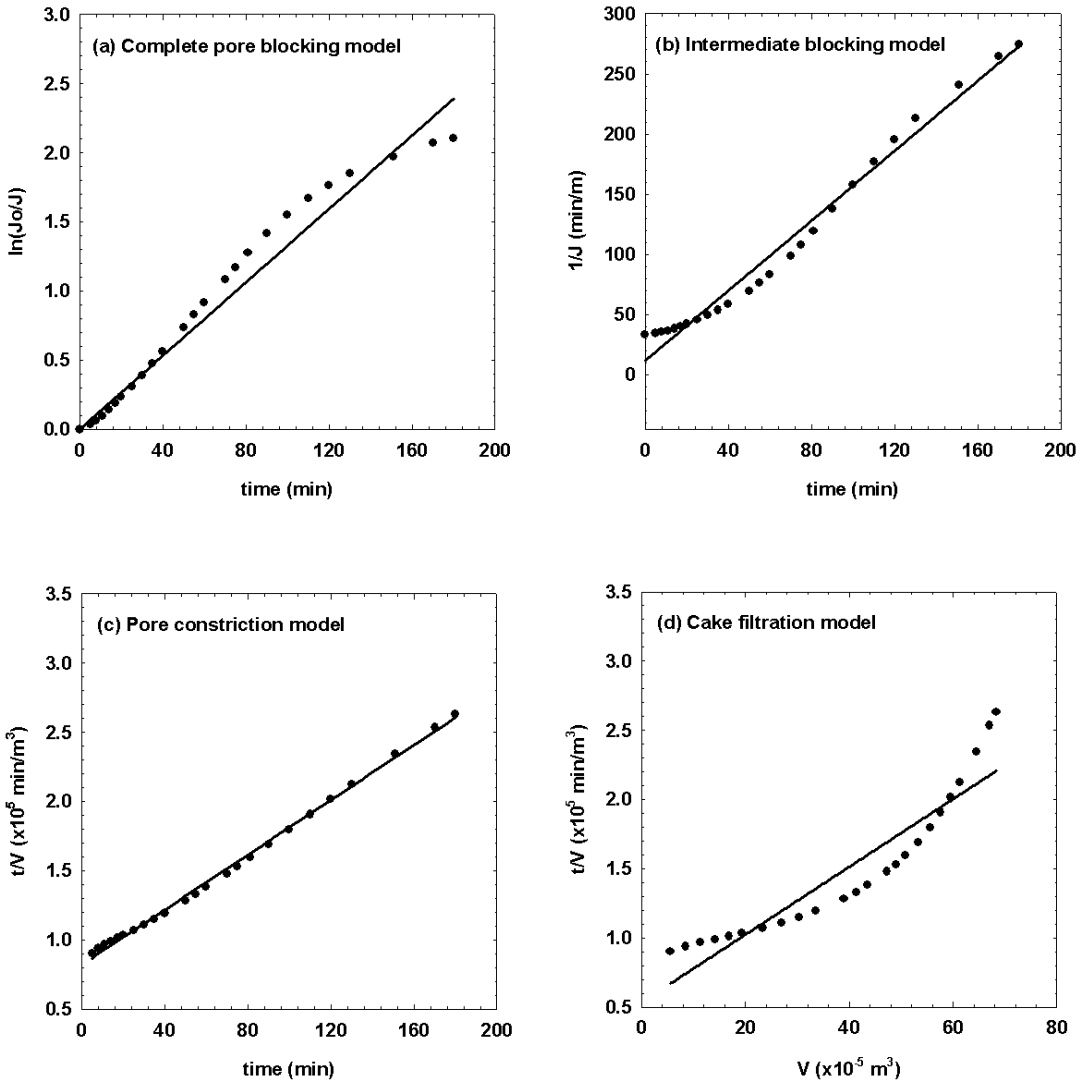

Fig. 5-13. BSA filtration data and fouling model fitting (solid lines) for Anopore^{TM} membranes.

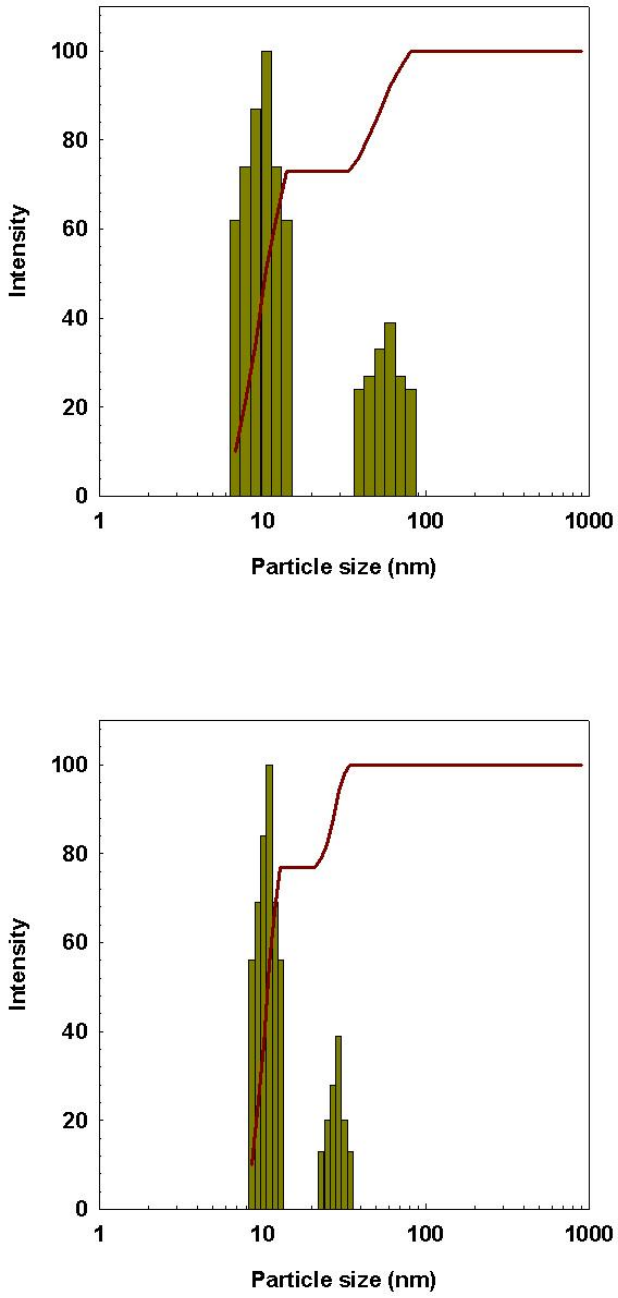

Fig. 5-14. BSA particle size distribution, (top) before and (bottom) after the filtration test.

aggregate sizes observed after filtration indicate the removal of large particles by adsorption on the pore surface and the generation of new protein aggregates from monomers and/or aggregates under an increased friction in the pores.

Model fitting on lysozyme filtration data also showed that the pore constriction model is the most appropriate one (R^2 = 0.999) that can account for the flux decline in spite of the presence of large aggregates, and it turned out that the flux data on amine functionalized and pegylated membranes were also well fitted to the pore constriction model (R^2 = 0.993 ~ 0.999), as shown in Fig. 5-15. Although there may be a transition in fouling models occurring for lysozyme filtration, the pore constriction model was employed to make quantitative comparisons.

For the pore constriction model a linear relationship [46, 65] can be derived from Darcy's law with the assumption that the rate of change in pore volume is proportional to the convection rate of protein particles:

$$\frac{t}{V} = \left(\frac{C_s}{AN_o \pi r_o^2 \delta_m} \right) t + \frac{1}{Q_o} \tag{5-1}$$

where C_s is the pore constriction constant, or the foulant volume deposited on the pore walls per unit filtrate volume, A is the front surface area of the membrane, N_o is the number of pores per membrane surface area, r_o is the pore radius of the clean membrane, δ_m is the membrane thickness, and Q_o is the initial filtrate flow rate. From FE-SEM images of the membranes N_o was estimated as 1.15×10^{13} m^{-2}, consistent with the result

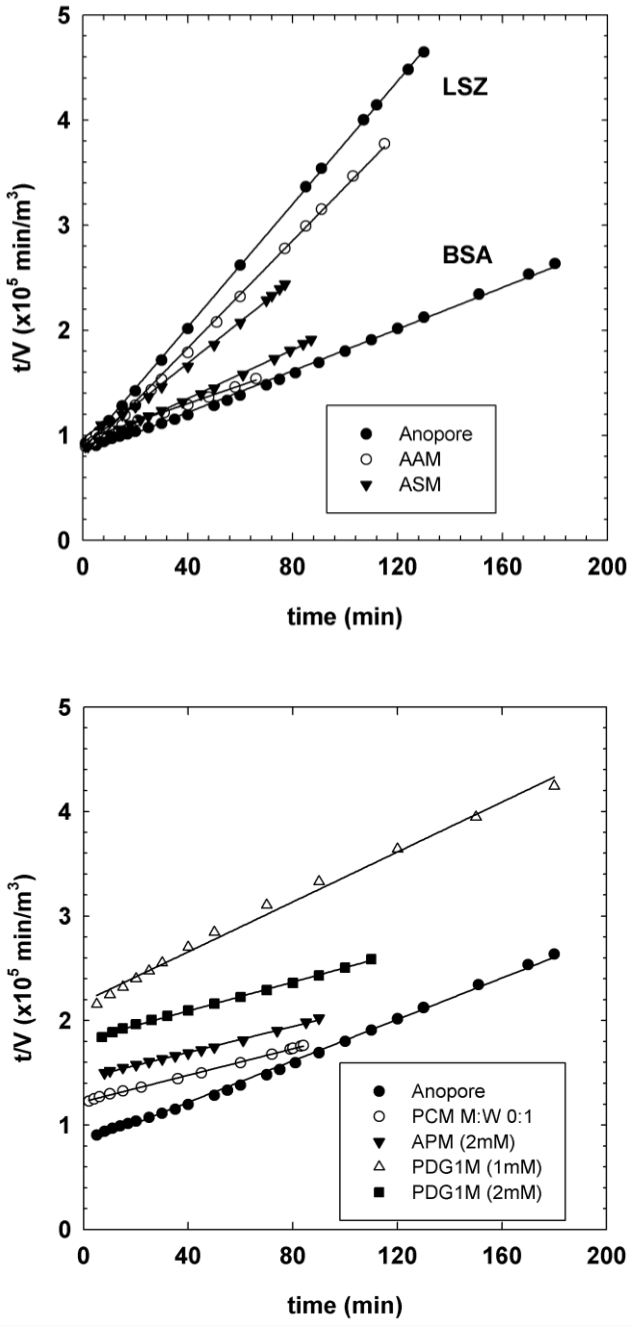

Fig. 5-15. Pore construction model fitting (solid lines) to (top) BSA and LSZ filtration data for amine functionalized membranes and (bottom) BSA filtration data for pegylated membranes.

previously reported (1.23×10^{13} m^{-2}) [159]. r_o was calculated by the Hagen-Poiseuille equation:

$$Q_o = \frac{AN_o \pi r_o^4 \Delta P}{8\mu\delta_m} \tag{5-2}$$

where ΔP is the transmembrane pressure and μ is the solution viscosity. The pore constriction constants (C_s) obtained by linear regression using Eq. (5-1) and (5-2) are given in Table 5-4. The results in Table 5-4 quantitatively show the effect of surface modification of Anopore^{TM} membranes on fouling. For amine functionalized membranes BSA adsorption on the pores looks less sensitive to the change in electrostatic interaction than lysozyme. This difference could be due to the low adsorption of BSA on silica surfaces [165]. For pegylated samples C_s significantly decreased compared with the bare Anopore^{TM} membrane, consistent with the idea that by modifying inorganic surfaces inorganic based membranes can broaden their potential for bioseparations.

5.4 Conclusions

The results described above demonstrate the potential of nanocomposite membranes for microfiltration. Using a variety of straightforward chemistries, it is possible to significantly reduce the fouling of ceramics substrates. Experiments wherein primary amines are grafted to the surface illustrate that electrostatic effects can be used to moderate fouling. The samples wherein the membranes are rendered hydrophobic and

Table 5-4. Pore constriction constants (C_s) from linear regression of filtration data for the bare, amine functionalized, and pegylated membranes.

Membrane sample	Protein	*Cs* ($\times 10^{-6}$ m^3/m^3)
Anopore™	BSA	12.64 ± 0.13
AAM	BSA	12.33 ± 0.25
ASM	BSA	14.94 ± 0.13
Anopore™	LSZ	35.42 ± 0.12
AAM	LSZ	32.16 ± 0.25
ASM	LSZ	23.83 ± 0.36
PCM (M:W 0:1)	BSA	7.02 ± 0.07
APM (2mM)	BSA	6.30 ± 0.10
PDG1M (1mM)	BSA	9.93 ± 0.25
PDG1M (2mM)	BSA	6.35 ± 0.07

subsequently exposed to Pluronic F108 show a significant reduction in fouling, even though the deposition of Pluronic on the surface is likely well below saturation coverage. Finally, the best results are obtained for samples wherein PEG is grafted to the surface. Modeling results indicate that the fouling can be explained by the pore constriction model. The modeling results also indicate protein adsorption on the pores depending on surface chemistries significantly changed the flux behavior. On whole the results show that functionalizing a ceramic membrane with an organic overlayer has the potential to provide membranes that possess both a uniform pore size distribution and surface chemistry that will reduce non-specific adsorption of proteins leading to superior materials for bioseparations.

CHAPTER VI

UV-REGENERATABLE HYDROPHILIC MEMBRANES FOR PROTEIN MICROFILTRATION

6.1 Introduction

Membrane fouling and the subsequent need for membrane regeneration have been of great interest in protein purification. However, to our knowledge, there has been no report on protein filtration employing TiO_2 membranes in order to utilize photocatalytic activity and superhydrophilicity even though it is very well known that the protein fouling can be significantly mitigated on hydrophilic surfaces. This could be because proteins may experience photodecomposition on the photocatalyst membrane under UV illumination. In fact, in most of the works given in section 1.6, UV is irradiated during reaction or filtration to use both photocatalytic activity and superhydrophilicity simultaneously. In protein filtration, however, UV illumination on TiO_2 surface should be avoided during filtration to prevent the denaturation of proteins. Thus, TiO_2 membranes may be effectively used for this purpose if superhydrophilicity is maintained without UV irradiation for a long time enough to obtain persistent anti-fouling effect. Another advantage of using photocatalytic membranes lies in the potential ability to regenerate them. Since membrane fouling is at some level inevitable, the feasibility of membrane regeneration is crucial in consideration of industrial acceptance. Current regeneration procedures often include backflushing, which showed

its ability to maintain flux in some filtration systems [166]. But, the effectiveness of this method was reported to vary depending on the membrane pore size and the solution to be filtered [167]. The most effective way to restore the flux is to clean the membranes in harsh acidic or basic conditions [167, 168]. Nevertheless, this chemical cleaning is not desirable in terms of the membrane durability and environmental aspects. Alternatively, photocatalytic degradation coupled with the self-cleaning effect of TiO_2 may be used to remove foulants from the membranes. This method can offer a simple and efficient way to regenerate the membranes without employing aggressive cleaning conditions. Therefore, synthesis of a membrane with durable hydrophilicity and strong photocatalytic activity is essential for successful protein filtration and membrane regeneration.

Several papers reported that addition of 10 – 30 mol% SiO_2 to TiO_2 film resulted in a significant increase in durability of superhydrophilicity in the dark [98, 169] as well as shorter time to recover superhydrophilicity by UV illumination than pure TiO_2 film [94], which may be ascribed to higher surface hydroxyl density of the mixed oxides [170]. Moreover, incorporation of SiO_2 is known to enhance photocatalytic activity of TiO_2 in oxidation reactions possibly due to new Brønsted acid sites generated by Ti-O-Si bridges [170, 171]. In this respect, TiO_2-SiO_2 mixed oxides seem to be a highly potential material for protein filtration membranes.

Therefore, in this chapter TiO_2 and TiO_2-SiO_2 membranes were studied to develop novel nanocomposite membranes that exhibit low fouling and can be easily regenerated. Also, a simple and universal plot was developed to see the deviations of the

experimental results from the classical fouling models at a glance. This is the first dimensionless plot, to our knowledge, that offers information about fouling behavior regardless of the fouling parameters.

6.2 Experimental

Membrane synthesis procedures were described in section 2.4. The TiO_2 coated Anopore^{TM} membranes synthesized by dip-coating and spin-coating are denoted as TA-D and TA-S, and TA-DS and TSA-DS are for the TiO_2 and TiO_2-SiO_2 membranes by both dip-coating and spin-coating, respectively. The fouled membranes were regenerated by irradiating UV (UVP, 254 nm, 1120 μW/cm^2 at 3 in.) for 12 h in DI water. During regeneration the water was gently stirred using an impeller and oxygen was bubbled to enhance photocatalysis.

Protein filtration test was performed using lysozyme (LSZ) as shown in section 2.5.2. Unless otherwise noted (Fig. 6-1), all the filtration tests were performed in the dark on the membranes that had been irradiated by UV for 3 h in DI water. Dynamic light scattering was used to measure the particle sizes of proteins, and UV-vis spectrophotometer was performed to analyze the optical absorption property of the photocatalysts on Anopore^{TM} (section 2.6).

6.3 Development of Dimensionless Plot

Although the membrane system is simple, membrane fouling is often difficult to interpret because various kinds of fouling occur simultaneously. Thus, identifying the dominant fouling mechanism is essential for understanding and quantitative analysis of the fouling. A lot of work has been performed to qualitatively and quantitatively determine fouling behavior (section 1.3.1). Typical methods to determine the fouling model include the plot of the general governing equations (Eq. (1-38) and (1-39)) and the linear relationship of each model to determine the dominant mechanism (Table 1-1). However, there has been no report on dimensionless approach that enables one to compare the fouling models in a plot. Here, we have developed a simple dimensionless plot for the classical fouling models.

The dimensionless fouling number was defined as the normalized value:

$$N_F \equiv \frac{V}{Q_0 t} = \frac{1}{t}\int_0^t \frac{Q}{Q_0} dt \tag{6-1}$$

where V is the filtrate volume, t is the filtration time, and Q_0 is the initial volumetric flow rate. Since the normalized volumetric flow rates or fluxes ($J_n = J/J_0$) are given in Eq. (1-30), (1-34) and (1-36) for the complete pore blocking, the pore constriction (standard), and the cake filtration models respectively, Eq. (6-1) can be integrated in each case. Then, all the unknown fouling parameters can be eliminated and N_F may be expressed as a function of J_n for the three classical models:

$$N_{F,b} = \frac{J_n - 1}{\ln J_n} \tag{6-2}$$

$$N_{F,s} = \sqrt{J_n} \tag{6-3}$$

$$N_{F,c} = \frac{2J_n}{1 + J_n} \tag{6-4}$$

where $N_{F,b}$ is the dimensionless fouling number for the complete pore blocking, $N_{F,s}$ is for the pore constriction, and $N_{F,c}$ is for the cake filtration model. Therefore, a comprehensive dimensionless plot can be constructed by N_F as a function of the normalized flux, J_n. Experimental N_F values are easily obtained from the definition in Eq. (6-1). This method may reduce the errors that can occur when using the general governing equation (Eq. (1-37)) due to no need for the evaluation of second derivatives.

6.4 Results

Fig. 6-1 shows the normalized flux data from microfiltration experiments of lysozyme over bare Anopore^{TM}, TiO_2 and TiO_2-SiO_2 coated membranes. While as-synthesized TA-DS membrane exhibited a slightly better flux behavior than Anopore^{TM} membrane, UV-irradiated membrane showed much less fouling (Fig. 6-1(a)), suggesting that UV has induced the membrane surface to be more hydrophilic. Fig. 6-1(b) shows a comparison of the flux decline for the UV-irradiated photocatalytic membranes, where it can be seen that the coating method and the composition of metal oxides affected filtration results. Table 6-1 shows the hydraulic permeabilities and the pore diameters of

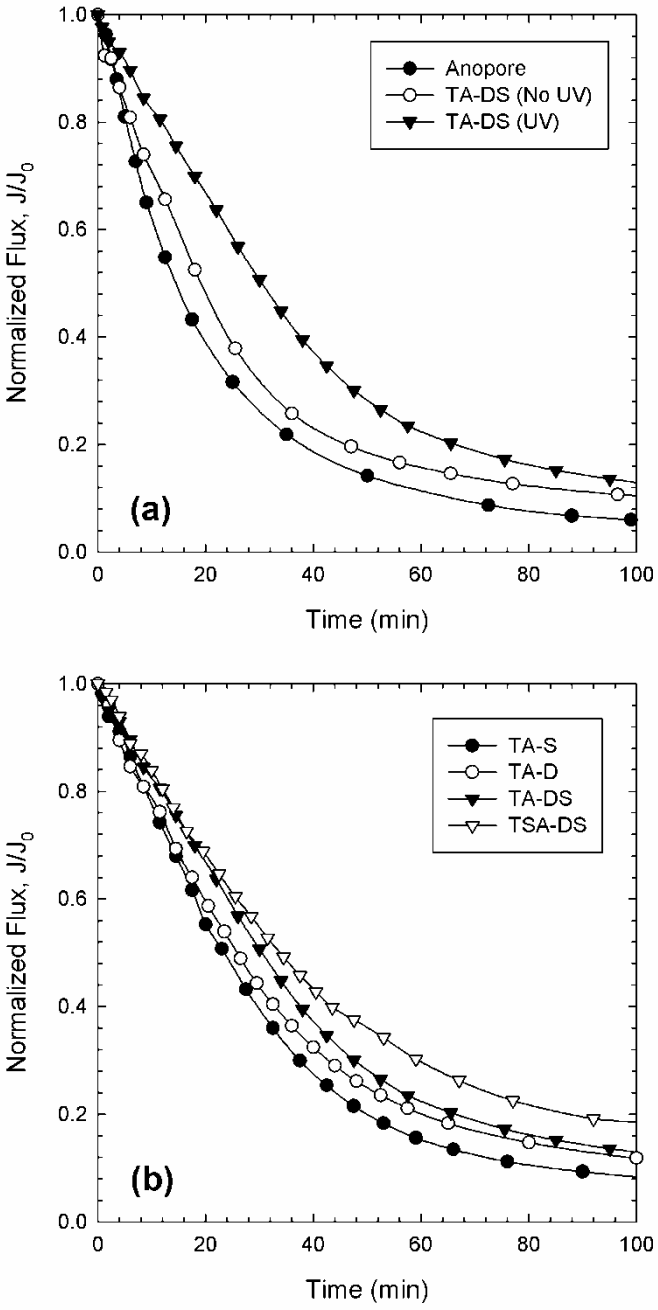

Fig. 6-1. Normalized LSZ filtrate flux as a function of filtration time for (a) UV-irradiated, as-synthesized TiO_2 membranes and bare Anopore^{TM} for comparison, and (b) a series of UV-irradiated photocatalytic membranes (lines are a guide to the eye).

Table 6-1. Hydraulic permeabilities (L_p) and pore diameters (d_p) for various samples.

Membrane sample	L_p (× 10^{-12} m)	d_p (nm)
Anopore	16.9	244.7
TA-S	11.2	221.1
TA-D	10.1	215.4
TA-DS	8.0	203.3
TSA-DS	8.4	205.3

the membranes, which were each calculated from Eqs. (1-27) and (5-2) based on PBS filtration test. From these data, if the metal-oxide coating is assumed to be uniform on the pore surfaces, the coating thickness on TA-S, TA-D, TA-DS and TSA-DS samples is calculated to be 11.8, 14.7, 20.7 and 19.7 nm, respectively. Thus it seems that the fouling is mitigated as the coating layer becomes thick and defectless by changing the coating method. The least fouling was achieved on the TSA-DS membrane that has the similar thickness as the TA-DS sample, which is consistent with the reports that the addition of SiO_2 to TiO_2 enhances hydrophilicity of the films [98, 169, 172].

The diffuse reflectance UV-vis spectra of the TiO_2 and TiO_2-SiO_2 coated membranes are shown in Fig. 6-2(a). The Kubelka-Munk function ($F(R)$) is defined as [173]:

$$F(R) \equiv \frac{K}{S} = \frac{(1-R)^2}{2R} \tag{6-5}$$

where K is the K-M absorption coefficient, S is the K-M scattering coefficient, and R is the reflectance ratio of the sample to reference ($R_{sample}/R_{reference}$). $R_{reference}$ is the reflectance of the bare Anopore^{TM} membrane in this study. Fig. 6-2(a) shows that the TiO_2-SiO_2 coated membrane has lower absorption than TiO_2 coated membrane in the wavelength range from 200 to 350 nm. The band gap (E_g) and the absorption coefficient (α) of an indirect semiconductor near the absorption threshold can be related by [174]:

$$\alpha h\nu = C_1(h\nu - E_g)^2 \tag{6-6}$$

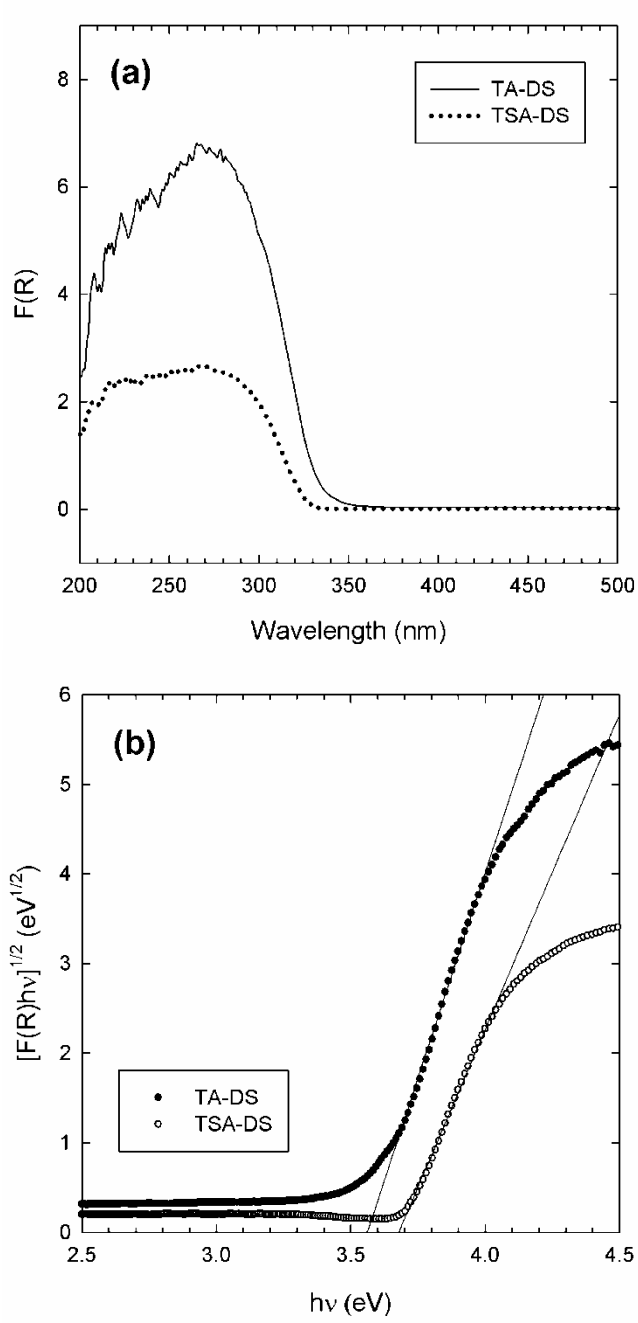

Fig. 6-2. (a) UV-vis absorption spectra of TiO_2 and TiO_2/SiO_2 coated membranes, and (b) the plot of $[F(R)h\nu]^{1/2}$ as a function of photon energy (F(R) is the Kubelka-Munk function).

where hv is the photon energy and C_1 is the constant. Since the K-M absorption coefficient K becomes 2α assuming the ideal scattering, the band gap can be extrapolated from the plotting of $[F(R)hv]^{1/2}$ against the photon energy, as shown in Fig. 6-2(b). From the intercept, the band gap of the TA-DS membrane is calculated to be 3.56 eV, which is larger than that of the typical anatase TiO_2 (3.1 – 3.4 eV [174, 175]). In fact, the absorption edge of TiO_2 is known to have a wide variation depending on the synthesis parameters such as temperature [176] and the doping of impurities [177]. For example, lower annealing temperature causes smaller particle size and poorer crystallinity, which in turn results in blue shift of the absorption edge due to the quantum size effect [174, 176, 178]. King *et al.* [179] have observed that the band gap shifts from 3.4 to 3.7 eV as the film thickness of TiO_2 changes from 15 to 4.5 nm in a work that precisely controlled the film thickness employing atomic layer deposition. Thus larger band gap of the TA-DS membrane is thought to be caused by smaller TiO_2 grain sizes, considering low annealing temperature and thin coating layers in this study. As for the TSA-DS membrane the band gap becomes 3.68 eV, even larger than that of the TA-DS sample. Blue shifts of band gap by adding SiO_2 have also been observed in the previous works [172, 175], which may be attributed to a suppressive effect of SiO_2 on the TiO_2 particle growth [169, 170, 172]. It is worthy of note that pure SiO_2 exhibits no absorption in the wavelength range between 200 and 500 nm [175].

As to crystallinity, X-ray diffraction was performed on the membranes but distinct peaks were not observed. This could be due to the low annealing temperature that was employed in our study to avoid the destruction of the polypropylene ring around

alumina membrane. The filtration test cannot be done without this polymer ring. Moreover, several works reported that the XRD peaks did not appear on the anatase TiO_2 thin films below a certain number of coatings [180-182]. For example, Choi *et al*. [181] observed the XRD peaks after at least seven coatings, in which the layer thickness was estimated to be *ca*. 0.7 μm.

Fig. 6-3 shows typical particle size distributions of lysozyme before and after the filtration test, and after the cleaning. It was shown that the large lysozyme aggregates have been removed after filtration, with formation of some small aggregates during filtration. Once the fouled membranes were regenerated by UV irradiation after the filtration test, the light scattering was performed on the cleaning solution to check the sizes of the lysozyme particles removed from the membrane (Fig. 6-3(c)). This data indicates that most of the foulants are heavily aggregated with sizes that are larger than the pore size of the membrane.

To evaluate the self-cleaning ability of the membranes, membrane regeneration tests were performed. As indicated by Guan [98], self-cleaning is considered to occur via both photocatalysis of the contaminants and recovery of hydrophilicity. However, it is not clear which mechanism plays a more crucial role in membrane regeneration. So the effect of UV irradiation and hydrophilic surface on a removal of foulants was investigated for the TA-DS membrane. First, the membrane pre-irradiated by UV (TA-DS (UV) in Fig. 6-1(a)) was regenerated by soaking in water for 12 h with a gentle stirring but without UV irradiation. The PBS flux was measured again, showing that the membrane hardly recovered the flux. Subsequently, the membrane was regenerated

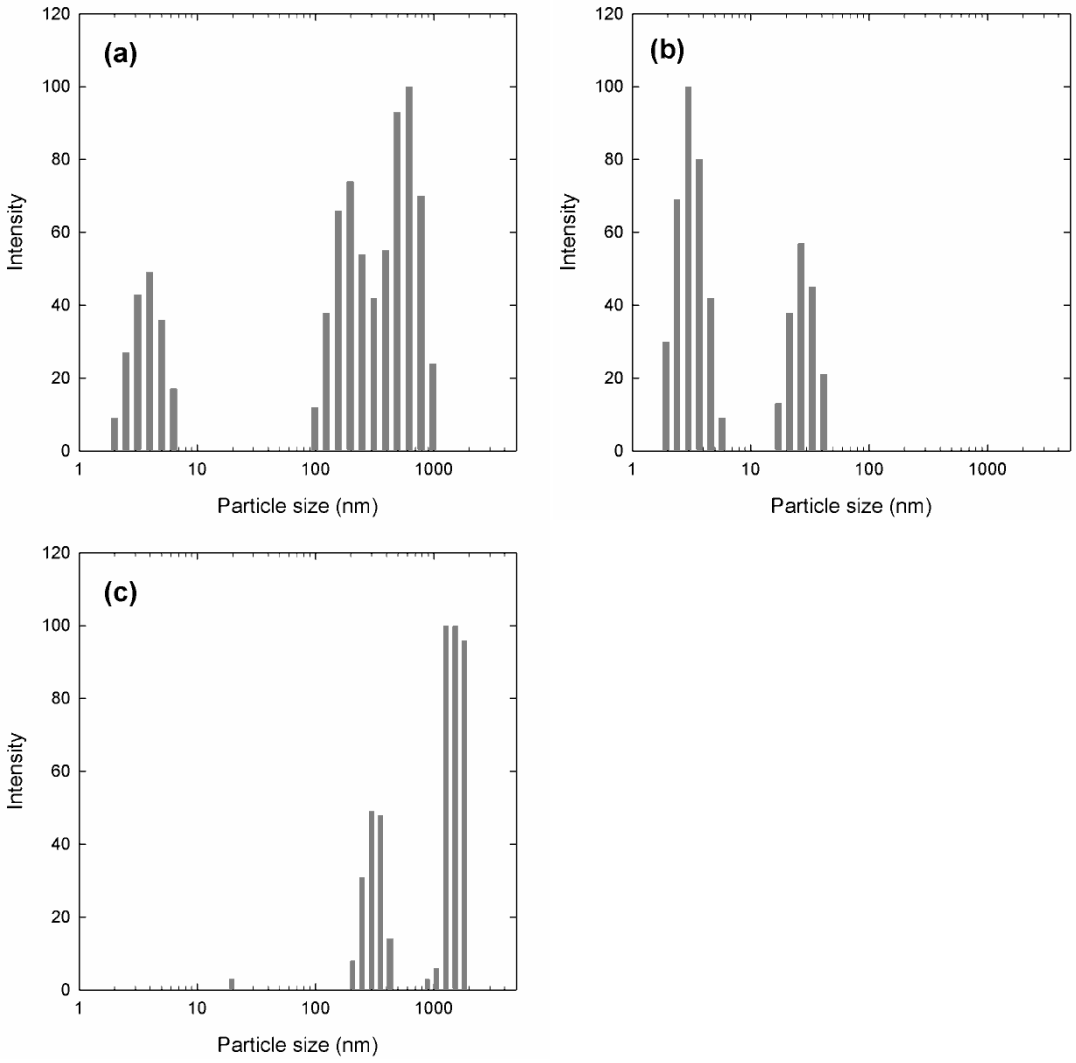

Fig. 6-3. LSZ particle size distribution (a) before, (b) after filtration, and (c) in the cleaning solution.

under UV irradiation and recovered about 75 % of the initial flux thereafter. On the other hand, the TA-DS (No UV) sample (Fig. 6-1(a)) showed about 30 % recovery of the initial flux by UV-regeneration, which implies that the foulants are more strongly deposited on the less hydrophilic surface. Therefore, it can be concluded that UV irradiation is essential for removing foulants and the efficiency becomes much higher on more hydrophilic surface.

Fig. 6-4(a) shows the recycling test results for the TSA-DS membrane. The recycled membrane, after the UV-regeneration, exhibited 90 % of the initial flux in the second test, which efficiency was higher than that for the TA-DS membrane. But in the third test the membrane showed the initial flux that is corresponding to only 35 % of the first test. To understand these results, flux behavior was analyzed using the general governing equation (Eq. (1-37)). Fig. 6-4(b) shows that the slopes are different from each test: i.e. 2.03 ± 0.11, 1.24 ± 0.05, and 0.43 ± 0.08 for the first, second, and third test, respectively. Considering each fouling model characterizes the slope as 2.0 for complete pore blocking, 1.5 for pore constriction, and 0 for cake filtration, the dominant fouling model appears to change as the filtration test is repeated. The dimensionless plot shows these results more clearly, as shown in Fig. 6-5. For both TSA-DS and TA-DS membranes, the pore constriction model looks dominant over the second filtration test whereas the flux decline of the first test initially follows the complete pore blocking model and thereafter the pore constriction and/or cake filtration model. Therefore, it is likely that an imperfect removal of the foulants in the pores caused a severe internal

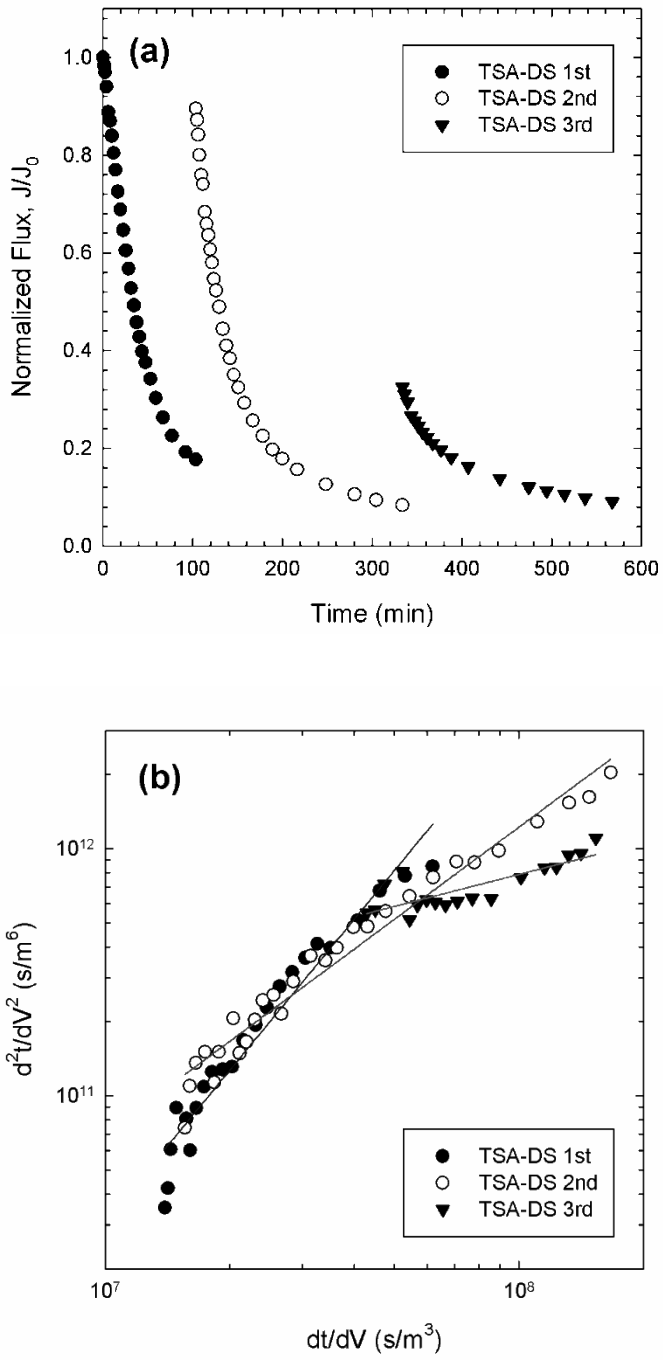

Fig. 6-4. (a) Membrane recycling test and (b) flux decline analysis for iterative LSZ filtration test of TSA-DS membrane.

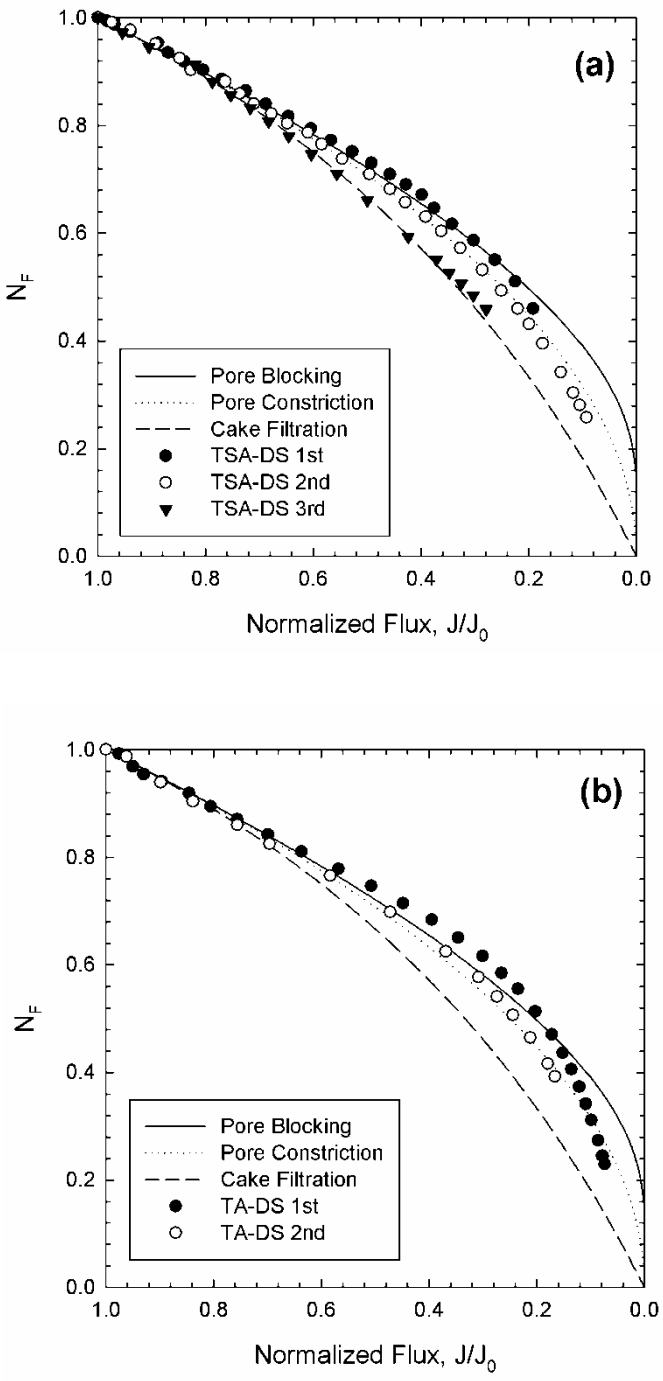

Fig. 6-5. Dimensionless flux-decline analysis for iterative LSZ filtration test of (a) TSA-DS membrane, and (b) TA-DS membrane.

fouling during second filtration test, and then, this in turn resulted in cake filtration in the third filtration test.

Several possibilities can be considered to explain a decreased efficiency. First, it is possible that the defects in the coating layers have been formed by film cracking during the drying and annealing steps [183]. Second, the photocatalytic activity may not be high enough to remove all the foulants. It is generally accepted that anatase shows higher photocatalytic activity than amorphous or rutile TiO_2 [95, 184]. Also, the photocatalytic activity shows a steep decline with decrease of film thickness below about 300 – 400 nm [185]. Thus, since our membranes are likely to have amorphous thin coating layers, the photocatalytic activity of the TA-DS and TSA-DS membranes could be relatively low. Finally, more hydrophilic surface may be necessary to increase the recycling efficiency. The regeneration test results described above suggest that the more hydrophilic the surface, the higher the regeneration efficiency. To meet these challenges, the optimum synthesis condition and procedure that can achieve both high photocatalytic activity and superhydrophilicity should be explored.

6.5 Conclusions

UV-regeneratable hydrophilic membranes have been synthesized by depositing TiO_2 or TiO_2-SiO_2 thin films on Anopore^{TM} support. Although no crystalline structure was observed, significantly reduced fouling has been achieved in lysozyme filtration test. The TiO_2-SiO_2 membrane showed better performance than TiO_2 membranes

regarding both flux decline and regeneration efficiency, supporting the results that the addition of SiO_2 enhances photocatalytic activity as well as hydrophilicity. It also has been shown that the band gap of the coating layers was larger than the typical TiO_2 particles, which could be ascribed to the small grain sizes and low thickness of the films.

In recycling tests that have employed UV-regeneration, while TiO_2-SiO_2 membrane exhibited very high recovery of the initial flux after the first regeneration, much lower flux was observed after the second regeneration, which could be due to a decrease of hydrophilicity by the unremoved foulants along with a relatively low photocatalytic activity. Also, it has been demonstrated that the dimensionless plot developed in this work can be a useful tool for comparison of the flux behavior in terms of the fouling models.

CHAPTER VII

FUTURE WORK AND CONCLUSIONS

7.1 Gas Transport Mechanism

In chapter III, it was shown that the residual solvent exerted strong influence on the permeance and selectivity of dendrimer-ceramic nanocomposite membranes. However, it is not quite clear how the residual solvent enhanced the propane/nitrogen selectivity. One possibility is that the gases transported through the solvent layers, which is plausible considering that the solubility-selectivity of propane/nitrogen reaches about 86 in THF solution. But this does not mean that other possibilities can be excluded. For example, surface diffusion also can be a good candidate that can explain high selectivities of the membranes. Moreover, the stable permeance results with time may be more clearly understood by the existence of surface diffusion. Therefore, it seems that more studies should be done on the gas transport mechanism through the dendrimer-ceramic membranes. Depending on the results, it may lead to the synthesis of very unusual membrane since exceptionally high selectivities have not been observed based on the surface diffusion mechanism with a few exceptions such as selective surface flow membranes [186, 187]. This is because at large pore sizes the Knudsen contribution is very large, and when the pore sizes become small or the pressure is high capillary condensation occurs. Thus, if the presence of organic moiety can reduce the Knudsen diffusion and capillary condensation simultaneously, the effect of surface

diffusion will be significant. In this respect, the dendrimers could be a quite suitable scaffold to functionalize the inorganic surfaces if they can secure a great deal of free volume near surface compared to when functionalizing the surface using flexible and linear hydrocarbons.

Therefore, to explore the possibility of surface diffusion, here is given the surface diffusion modeling on the preliminary results. Fig. 7-1 shows the normalized propane permeance as a function of pressure for G1-, G2-, and G3-C12 membranes that were shown in chapter III. As can be seen, the permeance shows different trends with pressure in the membranes as the dendrimer generation and, more importantly, the selectivity increase. In fact, similar trends already have been observed in the previous works in which inorganic membranes were functionalized by oligomeric hydrocarbons [123, 127]. In an effort to explain these results, a surface diffusion model has been proposed in Appendix B. This model assumed that the adsorbed molecules exhibit the viscous flow and that both monolayer and multilayer adsorptions were considered. As given in Figs. B-2, B-3, and B-4, the modeling results showed very different trends with increasing pressures by changing the parameters. Interestingly the model predicts an abrupt increase of the permeance with pressure when a great deal of multilayer adsorption (BET) is assumed (Fig. B-2), which is consistent with the results for the bare and G1-C12 membranes (Figs. 3-1 and 7-1). On the other hand, as the monolayer adsorption becomes dominant, a steep increase in permeance is not observed any more, and the permeance even decreases when highly favorable adsorption occurs (Figs. B-3 and B-4). This trend is well agreed with the G3-C12 results as shown in Fig. 7-1.

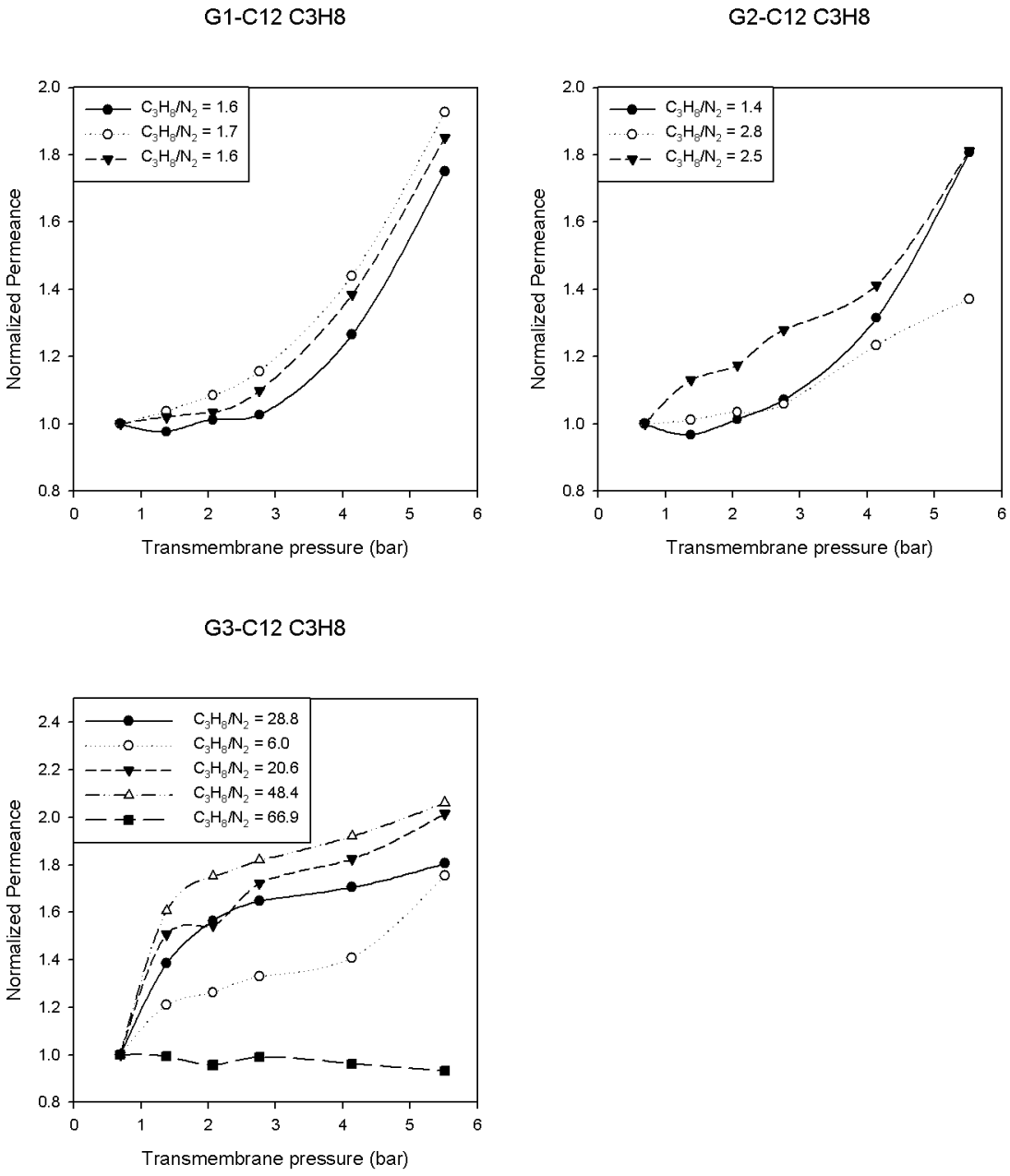

Fig. 7-1. Normalized propane permeance as a function of pressure for G1-, G2-, and G3-C12 membranes. The propane/nitrogen selectivities are the data measured at 20 psi.

Fig. 7-2 shows some model fittings using Eq. (B-6). This model fitting was performed to see how the parameters affect the permeance when the other parameters are fixed. First, the effect of α on the permeance was shown in Fig. 7-2(a). If the other parameters (*A*, *K*, and *c*) were assumed constant, α is fitted to be 0.14, 0.73 and 0.98 for the G1-, G2-, and G3-C12 membranes, respectively (R^2 = 0.9973). The fitting results of *A*, *K*, and *c* are each 1.22 mol/(m^2 sec), 0.12 bar^{-1}, and 11.8. It must be noted that Knudsen contribution was considered in case of the G1- and G2-C12 membranes for more accurate model fitting. The Knudsen contribution in propane permeance can be easily calculated from the nitrogen permeance and the Knudsen selectivity. Fig. 7-2(b) shows the model fitting for the G3-C12 membranes, assuming α =1 (i.e. only monolayer adsorption occurs). Then, *A* is fitted to be 0.47 ± 0.03 mol/(m^2 sec), and *K* is 0.46 ± 0.03, 0.23 ± 0.01, 0.21 ± 0.01, and 0.14 ± 0.01 bar^{-1} from top to bottom (R^2 = 0.9921). This result implies that as the binding energy of adsorption increases, the selectivity can be significantly enhanced. Thus, the effect of the residual solvent on high propane/nitrogen selectivities of the G3-C12 membranes may be reasonably explained by this surface diffusion model if the residual solvent enhances the solubility of propane on the surface. However, it seems that comprehensive conclusions on the effect of the residual solvent should be reached with more study on modeling and experimental evidence.

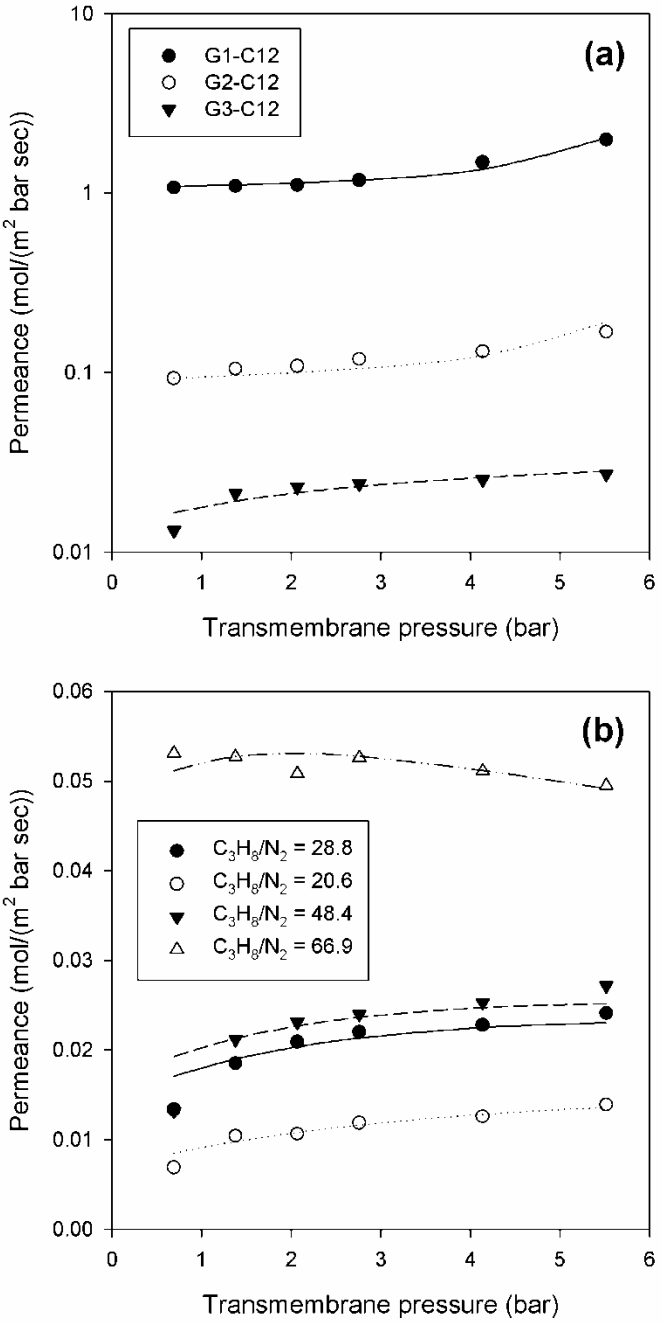

Fig. 7-2. Experimental results of propane permeance and model fittings for (a) the membranes with different dendrimer generations, and (b) G3-C12 membranes.

7.2 UV-regeneratable Superhydrophilic Membranes

Although it has been demonstrated in chapter VI that photocatalytic membranes can be effectively used for protein purification, the satisfactory and stable regeneration efficiency has yet to be obtained. This challenge may be met by improving photocatalytic activity and hydrophilicity of the membranes. In chapter VI, it seems that high TiO_2 crystallinity has not been obtained due to a restriction on annealing temperature. Thus, alternative ways to form anatase phase at low annealing temperature have to be explored.

Many works have demonstrated that the anatase crystalline phases can be formed even at low temperatures by changing precursor chemicals and/or synthesis procedures. One of them is using titanium tetrafluoride (TiF_4) as a titanium source [102, 188]. This method enables one to prepare anatase TiO_2 films even at room temperature, but the formation of hydrofluoric acid (HF) during reaction may be an obstacle to synthesis of TiO_2-SiO_2 membranes since SiO_2 is soluble in HF. Using acetic acid and tetrabutyl titanate is another method to obtain anatase TiO_2 particles at low annealing temperature [189, 190]. Acetic acid is thought to chelate to the Ti ions and to accelerate the formation of an anatase gel network. Li *et al.* [189] have shown that the choice of solvent could be very important. They argued that diethyl ether anhydrous caused rapid hydrolyzation so that more Ti^{3+} defect sites (oxygen vacancies) were generated. The oxygen vacancies are considered as the nucleation sites that can facilitate the phase transition of amorphous to anatase phase [191]. Hydrothermal annealing is also a very simple route to low temperature synthesis of crystalline [192, 193]. Yanagisawa *et al.*

[194] proposed that water acts as catalyst for anatase crystallization by bridging TiO^6 octahedra in amorphous phase. Typically in this method anatase phase can be obtained by keeping the precursor solution and water in an autoclave at 100 – 200 °C for several hours. However, it turned out from our experiment that this method cannot be used for Anopore^{TM} support because the hydrothermal treatment results in the phase transformation of alumina into boehmite (AlOOH), a very fragile material. Alternatively, it may be worth trying water vapor exposure for milder conditions [195]. Another interesting approach is a microwave treatment of the precursor solution [180], where it was proposed that a microwave irradiation enhances the growth of TiO_2 colloids. Similarly, UV-assisted sol-gel method was developed [191, 196]. In these works, it was proposed that UV irradiation using high pressure mercury lamp lowered anatase-forming annealing temperature by inducing oxygen vacancies on TiO_2 colloids.

To synthesize a photocatalytic membrane, the previous reports mentioned above can be directly used or combined. However, some modifications may be necessary to apply the above methods for membrane synthesis since most of these works have been performed to synthesize TiO_2 particles rather than thin films.

7.3 Conclusions

This dissertation has explored the synthesis and application of the nanocomposite membranes for gas separation and protein microfiltration, employing diverse hybridization on alumina supports. In an effort to overcome the shortcomings of

polymeric and inorganic membranes, organic-inorganic hybrid membranes have been synthesized in chapters III and V. Chapter III looked at the effect of the melamine-based dendrimers in ceramic supports on reverse-selective gas separation. It has been shown that the free volume can be controlled by dendrimer generations, which significantly affected the propane/nitrogen selectivity. For some G3-C12 membranes the extraordinarily high selectivities were obtained, but with a large variance. This result was ascribed to the presence of the residual solvent that affects the solubility of hydrocarbon species. Nevertheless, the adsorbed solvent turned out to be stable enough not to cause abrupt change in selectivity and permeance during the permeation test. In chapter V, various organic chemistries have been investigated to reduce the fouling during protein filtration. The electrostatic and hydrophilic properties provided for the membranes by functionalizing an alumina membrane with an organic overlayer, has been shown to have a strong influence on flux behavior. Therefore, this approach can offer a viable route to the synthesis of a membrane that has a high separation factor as well as low fouling.

Also, inorganic nanocomposite membranes have been fabricated to enlarge the arena of inorganic membrane. Chapter IV has studied the surfactant-templated mesoporous silica-ceramic nanocomposite membranes with the aim of preparing a uniform pored and defectless mesoporous membrane. It was shown that the defects substantially decreased through iterative synthesis of mesoporous silica in the ceramic macropores. But, at the same time, surfactant removal became more difficult as the coating cycle repeated, which was overcome by combining solvent extraction and

calcination. A study on UV-regeneratable hydrophilic membranes in chapter VI opened the way for an application of photocatalyt for bioseparations. Although this work showed the preliminary results, it demonstrated the potential of TiO_2-SiO_2/alumina nanocomposite membranes that not only can significantly reduce fouling, but can be regenerated by simple UV irradiation without using harsh cleaning solution.

Simple modeling was performed in an effort to explain the data more clearly. For example, the quantitative analyses of the membrane performance based on the classical models were provided in chapters IV and V for supporting the results. In chapter VI, a dimensionless plot has been developed in aid of comparing the data with the fouling models.

On whole, this dissertation offers diverse information which shows that by judiciously functionalizing the supports the nanocomposite membranes can be closer to the practical use for complex separations.

REFERENCES

[1] T.M. Przybycien, N.S. Pujar, L.M. Steele, Alternative bioseparation operations: Life beyond packed-bed chromatography, Current Opinion in Biotechnology 15 (2004) 469-478.

[2] M. Mulder, Basic Principles of Membrane Technology, Dordrecht: Kluwer Academic Publishers, 1996.

[3] W.J. Koros, Evolving beyond the thermal age of separation processes: Membranes can lead the way, AIChE Journal 50 (2004) 2326-2334.

[4] E.N. Lightfoot, J.S. Moscariello, Bioseparations, Biotechnology and Bioengineering 87 (2004) 259-273.

[5] R. van Reis, A. Zydney, Membrane separations in biotechnology, Current Opinion in Biotechnology 12 (2001) 208-211.

[6] A. Mehta, A.L. Zydney, Permeability and selectivity analysis for ultrafiltration membranes, Journal of Membrane Science 249 (2005) 245-249.

[7] W.S.W. Ho, K.K. Sirkar, Membrane Handbook, New York: Van Nostrand Reinhold, 1992.

[8] R.W. Baker, Future directions of membrane gas separation technology, Industrial & Engineering Chemistry Research 41 (2002) 1393-1411.

[9] T.C. Merkel, B.D. Freeman, R.J. Spontak, Z. He, I. Pinnau, P. Meakin, A.J. Hill, Ultrapermeable, reverse-selective nanocomposite membranes, Science 296 (2002) 519-522.

[10] H.B. Park, C.H. Jung, Y.M. Lee, A.J. Hill, S.J. Pas, S.T. Mudie, E. Van Wagner, B.D. Freeman, D.J. Cookson, Polymers with cavities tuned for fast selective transport of small molecules and ions, Science 318 (2007) 254-258.

[11] Z.P. Lai, G. Bonilla, I. Diaz, J.G. Nery, K. Sujaoti, M.A. Amat, E. Kokkoli, O. Terasaki, R.W. Thompson, M. Tsapatsis, D.G. Vlachos, Microstructural optimization of a zeolite membrane for organic vapor separation, Science 300 (2003) 456-460.

[12] G. Xomeritakis, N.G. Liu, Z. Chen, Y.B. Jiang, R. Kohn, P.E. Johnson, C.Y. Tsai, P.B. Shah, S. Khalil, S. Singh, C.J. Brinker, Anodic alumina supported

dual-layer microporous silica membranes, Journal of Membrane Science 287 (2007) 157-161.

[13] M.D. Jia, K.V. Peinemann, R.D. Behling, Preparation and characterization of thin-film zeolite PDMS composite membranes, Journal of Membrane Science 73 (1992) 119-128.

[14] W.J. Koros, R. Mahajan, Pushing the limits on possibilities for large scale gas separation: which strategies?, Journal of Membrane Science 175 (2000) 181-196.

[15] R.E. Kesting, A.K. Fritzsche, Polymeric Gas Separation Membranes, New York: John Wiley & Sons, Inc., 1993.

[16] R.S.A. Delange, K. Keizer, A.J. Burggraaf, Analysis and theory of gas-transport in microporous sol-gel derived ceramic membranes, Journal of Membrane Science 104 (1995) 81-100.

[17] R.J.R. Uhlhorn, K. Keizer, A.J. Burggraaf, Gas and surface-diffusion in modified gamma-alumina systems, Journal of Membrane Science 46 (1989) 225-241.

[18] L.S. Darken, Diffusion, mobility and their interrelation through free energy in binary metallic systems, Transactions of the American Institute of Mining and Metallurgical Engineers 175 (1948) 184-201.

[19] J.R. Xiao, J. Wei, Diffusion mechanism of hydrocarbons in zeolites. 1. Theory, Chemical Engineering Science 47 (1992) 1123-1141.

[20] K.C. McCarley, J.D. Way, Development of a model surface flow membrane by modification of porous [gamma]-alumina with octadecyltrichlorosilane, Separation and Purification Technology 25 (2001) 195-210.

[21] A.J. Burggraaf, Single gas permeation of thin zeolite (MFI) membranes: Theory and analysis of experimental observations, Journal of Membrane Science 155 (1999) 45-65.

[22] R.J.R. Uhlhorn, K. Keizer, A.J. Burggraaf, Gas-transport and separation with ceramic membranes. 1. Multilayer diffusion and capillary condensation, Journal of Membrane Science 66 (1992) 259-269.

[23] W.J. Koros, G.K. Fleming, Membrane-based gas separation, Journal of Membrane Science 83 (1993) 1-80.

[24] S.M. Jordan, W.J. Koros, Permeability of pure and mixed gases in silicone-rubber at elevated pressures, Journal of Polymer Science Part B-Polymer Physics 28 (1990) 795-809.

[25] L.M. Robeson, The upper bound revisited, Journal of Membrane Science 320 (2008) 390-400.

[26] R.W. Baker, N. Yoshioka, J.M. Mohr, A.J. Khan, Separation of organic vapors from air, Journal of Membrane Science 31 (1987) 259-271.

[27] M.B. Rao, S. Sircar, Nanoporous carbon membranes for separation of gas-mixtures by selective surface flow, Journal of Membrane Science 85 (1993) 253-264.

[28] B. Freeman, I. Pinnau, Separation of gases using solubility-selective polymers, Trends in Polymer Science 5 (1997) 167-173.

[29] J. Schultz, K.V. Peinemann, Membranes for separation of higher hydrocarbons from methane, Journal of Membrane Science 110 (1996) 37-45.

[30] L.M. Robeson, Correlation of separation factor versus permeability for polymeric membranes, Journal of Membrane Science 62 (1991) 165-185.

[31] X.F. Zeng, E. Ruckenstein, Membrane chromatography: Preparation and applications to protein separation, Biotechnology Progress 15 (1999) 1003-1019.

[32] D.B. Burns, A.L. Zydney, Effect of solution pH on protein transport through ultrafiltration membranes, Biotechnology and Bioengineering 64 (1999) 27-37.

[33] M.F. Ebersold, A.L. Zydney, The effect of membrane properties on the separation of protein charge variants using ultrafiltration, Journal of Membrane Science 243 (2004) 379-388.

[34] R. Ghosh, Q.Y. Li, Z.F. Cui, Fractionation of BSA and lysozyme using ultrafiltration: Effect of gas sparging, AIChE Journal 44 (1998) 61-67.

[35] R. Ghosh, Novel cascade ultrafiltration configuration for continuous, high-resolution protein-protein fractionation: A simulation study, Journal of Membrane Science 226 (2003) 85-99.

[36] R. Ghosh, Y.H. Wan, Z.F. Cui, G. Hale, Parameter scanning ultrafiltration - Rapid optimisation of protein separation, Biotechnology and Bioengineering 81 (2003) 673-682.

[37] R. van Reis, S. Gadam, L.N. Frautschy, S. Orlando, E.M. Goodrich, S. Saksena, R. Kuriyel, C.M. Simpson, S. Pearl, A.L. Zydney, High performance tangential flow filtration, Biotechnology and Bioengineering 56 (1997) 71-82.

[38] C.C. Ho, A.L. Zydney, A combined pore blockage and cake filtration model for protein fouling during microfiltration, Journal of Colloid and Interface Science 232 (2000) 389-399.

[39] L. Palacio, C.C. Ho, A.L. Zydney, Application of a pore-blockage - cake-filtration model to protein fouling during microfiltration, Biotechnology and Bioengineering 79 (2002) 260-270.

[40] L. Palacio, C.C. Ho, P. Pradanos, A. Hernandez, A.L. Zydney, Fouling with protein mixtures in microfiltration: BSA-lysozyme and BSA-pepsin, Journal of Membrane Science 222 (2003) 41-51.

[41] K. Nakamura, K. Matsumoto, Protein adsorption properties on a microfiltration membrane: A comparison between static and dynamic adsorption methods, Journal of Membrane Science 285 (2006) 126-136.

[42] A. Martin, R. Martinez, J.J. Calvo, P. Pradanos, L. Palacio, A. Hernandez, Protein adsorption onto an inorganic microfiltration membrane: Solute-solid interactions and surface coverage, Journal of Membrane Science 207 (2002) 199-207.

[43] K. Sakaguchi, M. Matsui, F. Mizukami, Applications of zeolite inorganic composites in biotechnology: Current state and perspectives, Applied Microbiology and Biotechnology 67 (2005) 306-311.

[44] S. Mochizuki, A.L. Zydney, Theoretical analysis of pore size distribution effects on membrane transport, Journal of Membrane Science 82 (1993) 211-227.

[45] J. Hermia, Constant pressure blocking filtration laws - Application to power-law non-newtonian fluids, Transactions of the Institution of Chemical Engineers 60 (1982) 183-187.

[46] E.M. Tracey, R.H. Davis, Protein fouling of track-etched polycarbonate microfiltration membranes, Journal of Colloid and Interface Science 167 (1994) 104-116.

[47] Y. Ye, P. Le Clech, V. Chen, A.G. Fane, B. Jefferson, Fouling mechanisms of alginate solutions as model extracellular polymeric substances, Desalination 175 (2005) 7-20.

[48] J. Mueller, R.H. Davis, Protein fouling of surface-modified polymeric microfiltration membranes, Journal of Membrane Science 116 (1996) 47-60.

[49] V.E. Gonsalves, A critical investigation on the viscose filtration process, Recueil Des Travaux Chimiques Des Pays-Bas-Journal of the Royal Netherlands Chemical Society 69 (1950) 873-903.

[50] W.R. Bowen, J.I. Calvo, A. Hernandez, Steps of membrane blocking in flux decline during protein microfiltration, Journal of Membrane Science 101 (1995) 153-165.

[51] C. Duclos-Orsello, W.Y. Li, C.C. Ho, A three mechanism model to describe fouling of microfiltration membranes, Journal of Membrane Science 280 (2006) 856-866.

[52] P. Wang, K.L. Tan, E.T. Kang, K.G. Neoh, Antifouling poly(vinylidene fluoride) microporous membranes prepared via plasma-induced surface grafting of poly(ethylene glycol), Journal of Adhesion Science and Technology 16 (2002) 111-127.

[53] S. Salgin, S. Takac, T.H. Ozdamar, A parametric study on protein-membrane-ionic environment interactions for membrane fouling, Separation Science and Technology 40 (2005) 1191-1212.

[54] Y.Q. Wang, T. Wang, Y.L. Su, F.B. Peng, H. Wu, Z.Y. Jiang, Remarkable reduction of irreversible fouling and improvement of the permeation properties of poly(ether sulfone) ultrafiltration membranes by blending with Pluronic F127, Langmuir 21 (2005) 11856-11862.

[55] C.C. Ho, A.L. Zydney, Effect of membrane morphology on the initial rate of protein fouling during microfiltration, Journal of Membrane Science 155 (1999) 261-275.

[56] M. Ulbricht, H. Matuschewski, A. Oechel, H.G. Hicke, Photo-induced graft polymerization surface modifications for the preparation of hydrophilic and low-protein-adsorbing ultrafiltration membranes, Journal of Membrane Science 115 (1996) 31-47.

[57] G.L. Kenausis, J. Voros, D.L. Elbert, N.P. Huang, R. Hofer, L. Ruiz-Taylor, M. Textor, J.A. Hubbell, N.D. Spencer, Poly(L-lysine)-g-poly(ethylene glycol) layers on metal oxide surfaces: Attachment mechanism and effects of polymer architecture on resistance to protein adsorption, Journal of Physical Chemistry B 104 (2000) 3298-3309.

[58] K.C. Popat, G. Mor, C. Grimes, T.A. Desai, Poly(ethylene glycol) grafted nanoporous alumina membranes, Journal of Membrane Science 243 (2004) 97-106.

[59] K.C. Popat, G. Mor, C.A. Grimes, T.A. Desai, Surface modification of nanoporous alumina surfaces with poly(ethylene glycol), Langmuir 20 (2004) 8035-8041.

[60] F. Cecchet, B. De Meersman, S. Demoustier-Champagne, B. Nysten, A.M. Jonas, One step growth of protein antifouling surfaces: Monolayers of poly(ethylene oxide) (PEO) derivatives on oxidized and hydrogen-passivated silicon surfaces, Langmuir 22 (2006) 1173-1181.

[61] N.P. Huang, R. Michel, J. Voros, M. Textor, R. Hofer, A. Rossi, D.L. Elbert, J.A. Hubbell, N.D. Spencer, Poly(L-lysine)-g-poly(ethylene glycol) layers on metal oxide surfaces: Surface-analytical characterization and resistance to serum and fibrinogen adsorption, Langmuir 17 (2001) 489-498.

[62] S. Tosatti, S.M. De Paul, A. Askendal, S. VandeVondele, J.A. Hubbell, P. Tengvall, M. Textor, Peptide functionalized poly(L-lysine)-g-poly(ethylene glycol) on titanium: Resistance to protein adsorption in full heparinized human blood plasma, Biomaterials 24 (2003) 4949-4958.

[63] P. Pradanos, A. Hernandez, J.I. Calvo, F. Tejerina, Mechanisms of protein fouling in cross-flow UF through an asymmetric inorganic membrane, Journal of Membrane Science 114 (1996) 115-126.

[64] P. Pradanos, J.I. Arribas, A. Hernandez, Retention of proteins in cross-flow UF through asymmetric inorganic membranes, AIChE Journal 40 (1994) 1901-1910.

[65] W.R. Bowen, Q. Gan, Properties of microfiltration membranes - Flux loss during constant pressure permeation of bovine serum-albumin, Biotechnology and Bioengineering 38 (1991) 688-696.

[66] O.A. Matthews, A.N. Shipway, J.F. Stoddart, Dendrimers - Branching out from curiosities into new technologies, Progress in Polymer Science 23 (1998) 1-56.

[67] W. Zhang, E.E. Simanek, Dendrimers based on melamine: Divergent and orthogonal, convergent syntheses of a G3 dendrimer, Organic Letters 2 (2000) 843-845.

[68] E.E. Simanek, S.O. Gonzalez, Dendrimers: Branching out of polymer chemistry, Journal of Chemical Education 79 (2002) 1222-1231.

[69] M.E. Davis, Ordered porous materials for emerging applications, Nature 417 (2002) 813-821.

[70] C.T. Kresge, M.E. Leonowicz, W.J. Roth, J.C. Vartuli, J.S. Beck, Ordered mesoporous molecular-sieves synthesized by a liquid-crystal template mechanism, Nature 359 (1992) 710-712.

[71] D.Y. Zhao, J.L. Feng, Q.S. Huo, N. Melosh, G.H. Fredrickson, B.F. Chmelka, G.D. Stucky, Triblock copolymer syntheses of mesoporous silica with periodic 50 to 300 angstrom pores, Science 279 (1998) 548-552.

[72] F. Kleitz, S.H. Choi, R. Ryoo, Cubic Ia3d large mesoporous silica: Synthesis and replication to platinum nanowires, carbon nanorods and carbon nanotubes, Chemical Communications (2003) 2136-2137.

[73] U. Ciesla, F. Schuth, Ordered mesoporous materials, Microporous and Mesoporous Materials 27 (1999) 131-149.

[74] S. Ruthstein, J. Schmidt, E. Kesselman, R. Popovitz-Biro, L. Omer, V. Frydman, Y. Talmon, D. Goldfarb, Molecular level processes and nanostructure evolution during the formation of the cubic mesoporous material KIT-6, Chemistry of Materials 20 (2008) 2779-2792.

[75] Q.S. Huo, R. Leon, P.M. Petroff, G.D. Stucky, Mesostructure design with gemini surfactants - supercage formation in a 3-dimensional hexagonal array, Science 268 (1995) 1324-1327.

[76] C.Z. Yu, J. Fan, B.Z. Tian, D.Y. Zhao, Morphology development of mesoporous materials: A colloidal phase separation mechanism, Chemistry of Materials 16 (2004) 889-898.

[77] A. Firouzi, D. Kumar, L.M. Bull, T. Besier, P. Sieger, Q. Huo, S.A. Walker, J.A. Zasadzinski, C. Glinka, J. Nicol, D.I. Margolese, G.D. Stucky, B.F. Chmelka, Cooperative organization of inorganic-surfactant and biomimetic assemblies, Science 267 (1995) 1138-1143.

[78] K. Flodstrom, H. Wennerstrom, C.V. Teixeira, H. Amenitsch, M. Linden, V. Alfredsson, Time-resolved in situ studies of the formation of cubic mesoporous silica formed with triblock copolymers, Langmuir 20 (2004) 10311-10316.

[79] M. Ogawa, N. Masukawa, Preparation of transparent thin films of lamellar, hexagonal and cubic silica-surfactant mesostructured materials by rapid solvent evaporation methods, Microporous and Mesoporous Materials 38 (2000) 35-41.

[80] D. Grosso, F. Cagnol, G. Soler-Illia, E.L. Crepaldi, H. Amenitsch, A. Brunet-Bruneau, A. Bourgeois, C. Sanchez, Fundamentals of mesostructuring through evaporation-induced self-assembly, Advanced Functional Materials 14 (2004) 309-322.

[81] M.P. Tate, B.W. Eggiman, J.D. Kowalski, H.W. Hillhouse, Order and orientation control of mesoporous silica films on conducting gold substrates formed by dip-coating and self-assembly: A grazing angle of incidence small-angle X-ray scattering and field emission scanning electron microscopy study, Langmuir 21 (2005) 10112-10118.

[82] B.A. McCool, N. Hill, J. DiCarlo, W.J. DeSisto, Synthesis and characterization of mesoporous silica membranes via dip-coating and hydrothermal deposition techniques, Journal of Membrane Science 218 (2003) 55-67.

[83] A. Yamaguchi, F. Uejo, T. Yoda, T. Uchida, Y. Tanamura, T. Yamashita, N. Teramae, Self-assembly of a silica-surfactant nanocomposite in a porous alumina membrane, Nature Materials 3 (2004) 337-341.

[84] S.J. Yoo, D.M. Ford, D.F. Shantz, Synthesis and characterization of uniform alumina-mesoporous silica hybrid membranes, Langmuir 22 (2006) 1839-1845.

[85] H. Kominami, S. Murakami, J. Kato, Y. Kera, B. Ohtani, Correlation between some physical properties of titanium dioxide particles and their photocatalytic activity for some probe reactions in aqueous systems, Journal of Physical Chemistry B 106 (2002) 10501-10507.

[86] S. Ciston, R.M. Lueptow, K.A. Gray, Bacterial attachment on reactive ceramic ultrafiltration membranes, Journal of Membrane Science 320 (2008) 101-107.

[87] B. Oregan, M. Gratzel, A low-cost, high-efficiency solar-cell based on dye-sensitized colloidal TiO_2 films, Nature 353 (1991) 737-740.

[88] Y.C. Kim, K.H. Lee, S. Sasaki, K. Hashimoto, K. Ikebukuro, I. Karube, Photocatalytic sensor for chemical oxygen demand determination based on oxygen electrode, Analytical Chemistry 72 (2000) 3379-3382.

[89] W.Y. Dong, Y.J. Sun, C.W. Lee, W.M. Hua, X.C. Lu, Y.F. Shi, S.C. Zhang, J.M. Chen, D.Y. Zhao, Controllable and repeatable synthesis of thermally stable anatase nanocrystal-silica composites with highly ordered hexagonal mesostructures, Journal of the American Chemical Society 129 (2007) 13894-13904.

[90] M.R. Hoffmann, S.T. Martin, W.Y. Choi, D.W. Bahnemann, Environmental applications of semiconductor photocatalysis, Chemical Reviews 95 (1995) 69-96.

[91] C. Aprile, A. Corma, H. Garcia, Enhancement of the photocatalytic activity of TiO_2 through spatial structuring and particle size control: From subnanometric to

submillimetric length scale, Physical Chemistry Chemical Physics 10 (2008) 769-783.

[92] T. Kawahara, Y. Konishi, H. Tada, N. Tohge, J. Nishii, S. Ito, A patterned TiO_2(anatase)/TiO_2(rutile) bilayer-type photocatalyst: Effect of the anatase/rutile junction on the photocatalytic activity, Angewandte Chemie 114 (2002) 2935-2937.

[93] P. Yang, M. Yang, S.L. Zou, J.Y. Xie, W.T. Yang, Positive and negative TiO_2 micropatterns on organic polymer substrates, Journal of the American Chemical Society 129 (2007) 1541-1552.

[94] M. Maeda, S. Yamasaki, Effect of silica addition on crystallinity and photo-induced hydrophilicity of titania-silica mixed films prepared by sol-gel process, Thin Solid Films 483 (2005) 102-106.

[95] K. Tanaka, M.F.V. Capule, T. Hisanaga, Effect of crystallinity of TiO_2 on its photocatalytic action, Chemical Physics Letters 187 (1991) 73-76.

[96] R. Wang, K. Hashimoto, A. Fujishima, M. Chikuni, E. Kojima, A. Kitamura, M. Shimohigoshi, T. Watanabe, Light-induced amphiphilic surfaces, Nature 388 (1997) 431-432.

[97] R. Wang, K. Hashimoto, A. Fujishima, M. Chikuni, E. Kojima, A. Kitamura, M. Shimohigoshi, T. Watanabe, Photogeneration of highly amphiphilic TiO_2 surfaces, Advanced Materials 10 (1998) 135-138.

[98] K.H. Guan, Relationship between photocatalytic activity, hydrophilicity and self-cleaning effect of TiO_2/SiO_2 films, Surface & Coatings Technology 191 (2005) 155-160.

[99] F.C. Cebeci, Z.Z. Wu, L. Zhai, R.E. Cohen, M.F. Rubner, Nanoporosity-driven superhydrophilicity: A means to create multifunctional antifogging coatings, Langmuir 22 (2006) 2856-2862.

[100] A. Rahimpour, S.S. Madaeni, A.H. Taheri, Y. Mansourpanah, Coupling TiO_2 nanoparticles with UV irradiation for modification of polyethersulfone ultrafiltration membranes, Journal of Membrane Science 313 (2008) 158-169.

[101] H. Choi, A.C. Sofranko, D.D. Dionysiou, Nanocrystalline TiO_2 photocatalytic membranes with a hierarchical mesoporous multilayer structure: Synthesis, characterization, and multifunction, Advanced Functional Materials 16 (2006) 1067-1074.

[102] X.W. Zhang, A.J. Du, P. Lee, D.D. Sun, J.O. Leckie, Grafted multifunctional titanium dioxide nanotube membrane: Separation and photodegradation of aquatic pollutant, Applied Catalysis B-Environmental 84 (2008) 262-267.

[103] S.S. Madaeni, N. Ghaemi, Characterization of self-cleaning RO membranes coated with TiO_2 particles under UV irradiation, Journal of Membrane Science 303 (2007) 221-233.

[104] G.R. Gallaher, P.K.T. Liu, Characterization of ceramic membranes. 1. Thermal and hydrothermal stabilities of commercial 40 Angstrom membranes, Journal of Membrane Science 92 (1994) 29-44.

[105] A. Javaid, D.A. Krapchetov, D.M. Ford, Solubility-based gas separation with oligomer-modified inorganic membranes - Part III. Effects of synthesis conditions, Journal of Membrane Science 246 (2005) 181-191.

[106] E.J. Acosta, C.S. Carr, E.E. Simanek, D.F. Shantz, Engineering nanospaces: Iterative synthesis of melamine-based dendrimers on amine-functionalized SBA-15 leading to complex hybrids with controllable chemistry and porosity, Advanced Materials 16 (2004) 985-989.

[107] S. Yoo, J.D. Lunn, S. Gonzalez, J.A. Ristich, E.E. Simanek, D.F. Shantz, Engineering nanospaces: OMS/dendrimer hybrids possessing controllable chemistry and porosity, Chemistry of Materials 18 (2006) 2935-2942.

[108] R.C. Hayward, P.C.A. Alberius, E.J. Kramer, B.F. Chmelka, Thin films of bicontinuous cubic mesostructured silica templated by a nonionic surfactant, Langmuir 20 (2004) 5998-6004.

[109] W.R. Thompson, J.E. Pemberton, Characterizatoin of octadecylsilane and stearic acid layers on Al_2O_3 surfaces by Raman spectroscopy, Langmuir 11 (1995) 1720-1725.

[110] C.R. Martin, Nanomaterials - A membrane-based synthetic approach, Nature 266 (1994) 1961-1966.

[111] C. Leger, H.D. Lira, R. Paterson, Preparation and properties of surface modified ceramic membranes. 3. Gas permeation of 5 nm alumina membranes modified by trichloro-octadecylsilane, Journal of Membrane Science 120 (1996) 187-195.

[112] C. Leger, H.D. Lira, R. Paterson, Preparation and properties of surface modified ceramic membranes. 2. Gas and liquid permeabilities of 5 nm alumina membranes modified by a monolayer of bound polydimethylsiloxane (PDMS) silicone oil, Journal of Membrane Science 120 (1996) 135-146.

[113] S.J. Gregg, K.S.W. Sing, Adsorption, Surface area, and Porosity, London: Academic Press, 1982.

[114] E.P. Barrett, L.G. Joyner, P.P. Halenda, The determination of pore volume and area distributions in porous substances. 1. Computations from nitrogen isotherms, Journal of the American Chemical Society 73 (1951) 373-380.

[115] M. Kruk, M. Jaroniec, A. Sayari, Application of large pore MCM-41 molecular sieves to improve pore size analysis using nitrogen adsorption measurements, Langmuir 13 (1997) 6267-6273.

[116] M.V. Chandak, Y.S. Lin, W. Ji, R.J. Higgins, Sorption and diffusion of VOCs in DAY zeolite and silicalite-filled PDMS membranes, Journal of Membrane Science 133 (1997) 231-243.

[117] Q. Hu, E. Marand, S. Dhingra, D. Fritsch, J. Wen, G. Wilkes, Poly(amide-imide)/TiO_2 nano-composite gas separation membranes: Fabrication and characterization, Journal of Membrane Science 135 (1997) 65-79.

[118] C. Joly, S. Goizet, J.C. Schrotter, J. Sanchez, M. Escoubes, Sol-gel polyimide-silica composite membrane: Gas transport properties, Journal of Membrane Science 130 (1997) 63-74.

[119] M. Moaddeb, W.J. Koros, Gas transport properties of thin polymeric membranes in the presence of silicon dioxide particles, Journal of Membrane Science 125 (1997) 143-163.

[120] M. Smaihi, T. Jermoumi, J. Marignan, R.D. Noble, Organic-inorganic gas separation membranes: Preparation and characterization, Journal of Membrane Science 116 (1996) 211-220.

[121] W.I. Sohn, D.H. Ryu, S.J. Oh, J.K. Koo, A study on the development of composite membranes for the separation of organic vapors, Journal of Membrane Science 175 (2000) 163-170.

[122] I.F.J. Vankelecom, C. Dotremont, M. Morobe, J.B. Uytterhoeven, C. Vandecasteele, Zeolite-filled PDMS membranes. 1. Sorption of halogenated hydrocarbons, Journal of Physical Chemistry B 101 (1997) 2154-2159.

[123] A. Javaid, D.M. Ford, Solubility-based gas separation with oligomer-modified inorganic membranes - Part II. Mixed gas permeation of 5 nm alumina membranes modified with octadecyltrichlorosilane, Journal of Membrane Science 215 (2003) 157-168.

[124] A. Javaid, S.O. Gonzalez, E.E. Simanek, D.M. Ford, Nanocomposite membranes of chemisorbed and physisorbed molecules on porous alumina for environmentally important separations, Journal of Membrane Science 275 (2006) 255-260.

[125] A. Javaid, M.P. Hughey, V. Varutbangkul, D.M. Ford, Solubility-based gas separation with oligomer-modified inorganic membranes, Journal of Membrane Science 187 (2001) 141-150.

[126] J. Randon, R. Paterson, Preliminary studies on the potential for gas separation by mesoporous ceramic oxide membranes surface modified by alkyl phosphonic acids, Journal of Membrane Science 134 (1997) 219-223.

[127] R.P. Singh, P. Jha, K. Kalpakci, J.D. Way, Dual-surface-modified reverse-selective membranes, Industrial & Engineering Chemistry Research 46 (2007) 7246-7252.

[128] R.P. Singh, J.D. Way, S.F. Dec, Silane modified inorganic membranes: Effects of silane surface structure, Journal of Membrane Science 259 (2005) 34-46.

[129] R.P. Singh, J.D. Way, K.C. McCarley, Development of a model surface flow membrane by modification of porous vycor glass with a fluorosilane, Industrial & Engineering Chemistry Research 43 (2004) 3033-3040.

[130] S.B. Lee, D.T. Mitchell, L. Trofin, T.K. Nevanen, H. Soderlund, C.R. Martin, Antibody-based bio-nanotube membranes for enantiomeric drug separations, Science 296 (2002) 2198-2200.

[131] T. Aydogmus, D.A. Ford, Molecular simulation of permeation through alkyl-functionalized mesoporous ceramic membranes, Journal of Membrane Science 314 (2008) 173-182.

[132] S.A. Stern, V.A. Shah, V.J. Hardy, Structure-permeability relationship in silicon polymers, Journal of Polymer Science Part B-Polymer Physics 25 (1987) 1263.

[133] B.E. Poling, J.M. Prausnitz, J.P. O'Connell, The Properties of Gases and Liquids. 5th ed, New York: McGraw-Hill, 2001.

[134] B.D. Freeman, Basis of permeability/selectivity tradeoff relations in polymeric gas separation membranes, Macromolecules 32 (1999) 375-380.

[135] J. Brandrup, E.H. Immergut, Polymer Handbook. 3rd ed, New York: Wiley, 1989.

[136] F. Gibanel, M.C. Lopez, F.M. Royo, J. Santafe, J.S. Urieta, Solubility of nonpolar gases in tetrahydrofuran at 0 to 30-degrees-c and 101.33 kpa partial-pressure of gas, Journal of Solution Chemistry 22 (1993) 211-217.

[137] H. Hippler, J. Troe, H.J. Wendelken, Collisional deactivation of vibrationally highly excited polyatomic-molecules. 2. Direct observations for excited toluene, Journal of Chemical Physics 78 (1983) 6709-6717.

[138] J.E. Jolley, J.H. Hildebrand, Solubility, entropy and partial molal volumes in solutions of gases in non-polar solvents, Journal of the American Chemical Society 80 (1958) 1050-1054.

[139] R.J.R. Uhlhorn, M. Veld, K. Keizer, A.J. Burggraaf, High permselectivities of microporous silica-modified gamma-alumina membranes, Journal of Materials Science Letters 8 (1989) 1135-1138.

[140] N. Nishiyama, K. Ueyama, M. Matsukata, Gas permeation through zeolite-alumina composite membranes, AIChE Journal 43 (1997) 2724-2730.

[141] V. Richard, E. Favre, D. Tondeur, A. Nijmeijer, Experimental study of hydrogen, carbon dioxide and nitrogen permeation through a microporous silica membrane, Chemical Engineering Journal 84 (2001) 593-598.

[142] B.D. Reid, A. Ruiz-Trevino, I.H. Musselman, K.J. Balkus, J.P. Ferraris, Gas permeability properties of polysulfone membranes containing the mesoporous molecular sieve MCM-41, Chemistry of Materials 13 (2001) 2366-2373.

[143] N. Nishiyama, D.H. Park, A. Koide, Y. Egashira, K. Ueyama, A mesoporous silica (MCM-48) membrane: preparation and characterization, Journal of Membrane Science 182 (2001) 235-244.

[144] G. Xomeritakis, C.M. Braunbarth, B. Smarsly, N. Liu, R. Kohn, Z. Klipowicz, C.J. Brinker, Aerosol-assisted deposition of surfactant-templated mesoporous silica membranes on porous ceramic supports, Microporous and Mesoporous Materials 66 (2003) 91-101.

[145] Y.Y. Wu, G.S. Cheng, K. Katsov, S.W. Sides, J.F. Wang, J. Tang, G.H. Fredrickson, M. Moskovits, G.D. Stucky, Composite mesostructures by nano-confinement, Nature Materials 3 (2004) 816-822.

[146] N.R.B. Coleman, G.S. Attard, Ordered mesoporous silicas prepared from both micellar solutions and liquid crystal phases, Microporous and Mesoporous Materials 44 (2001) 73-80.

[147] M.C. Burleigh, M.A. Markowitz, M.S. Spector, B.P. Gaber, Nanoporous organosilicas: Periodic materials synthesized with surfactant templates in acidic media, Journal of Physical Chemistry B 106 (2002) 9712-9716.

[148] S. Lim, H. Yoshitake, T. Tatsumi, Synthesis of cubic Ia(3)over-bard-like mesostructured silica at low temperature using an oligomeric nonionic surfactant, Chemistry Letters 34 (2005) 1434-1435.

[149] B. Platschek, N. Petkov, D. Himsl, S. Zimdars, Z. Li, R. Kohn, T. Bein, Vertical columnar block-copolymer-templated mesoporous silica via confined phase transformation, Journal of the American Chemical Society 130 (2008) 17362-17371.

[150] J.H. Lei, D. Liu, L.P. Guo, X.M. Yan, H. Tong, Fabrication and characterization of hexagonal mesoporous silica monolith via post-synthesized hydrothermal process, Journal of Sol-Gel Science and Technology 39 (2006) 169-174.

[151] D.Y. Zhao, Q.S. Huo, J.L. Feng, B.F. Chmelka, G.D. Stucky, Nonionic triblock and star diblock copolymer and oligomeric surfactant syntheses of highly ordered, hydrothermally stable, mesoporous silica structures, Journal of the American Chemical Society 120 (1998) 6024-6036.

[152] A.Y. Ku, S.T. Taylor, S.M. Loureiro, Mesoporous silica composites containing multiple regions with distinct pore size and complex pore organization, Journal of the American Chemical Society 127 (2005) 6934-6935.

[153] K.Y. Huang, Z.P. He, K.J. Chao, Mesoporous silica films - Characterization and reduction of their water uptake, Thin Solid Films 495 (2006) 197-204.

[154] U. Beuscher, C.H. Gooding, Characterization of the porous support layer of composite gas permeation membranes, Journal of Membrane Science 132 (1997) 213-227.

[155] M.S. Strano, H.C. Foley, Modeling ideal selectivity variation in nanoporous membranes, Chemical Engineering Science 58 (2003) 2745-2758.

[156] P.C. Carman, Flow of Gases through Porous Media, London: Academic press, 1956.

[157] K. Keizer, R.J.R. Uhlhorn, R.J. Vanvuren, A.J. Burggraaf, Gas separation mechanisms in microporous modified gamma-Al_2O_3 membranes, Journal of Membrane Science 39 (1988) 285-300.

[158] Y. Chen, T. Miyano, A. Fouda, T. Matsuura, Preparation and gas permeation properties of silicone-coated dry polyethersulfone membranes, Journal of Membrane Science 48 (1990) 203-219.

[159] G.P. Crawford, L.M. Steele, R. Ondris-Crawford, G.S. Iannacchione, C.J. Yeager, J.W. Doane, D. Finotello, Characterization of the cylindrical cavities of Anopore and Nucleopore membranes, Journal of Chemical Physics 96 (1992) 7788-7796.

[160] A. Hernandez, J.I. Calvo, P. Pradanos, L. Palacio, M.L. Rodriguez, J.A. de Saja, Surface structure of microporous membranes by computerized SEM image analysis applied to Anopore filters, Journal of Membrane Science 137 (1997) 89-97.

[161] S.T. Kelly, A.L. Zydney, Protein fouling during microfiltration: Comparative behavior of different model proteins, Biotechnology and Bioengineering 55 (1997) 91-100.

[162] J. Grdadolnik, Y. Marechal, Bovine serum albumin observed by infrared spectrometry. II. Hydration mechanisms and interaction configurations of embedded H_2O molecules, Biopolymers 62 (2001) 54-67.

[163] C.G.P.H. Schroen, M.A. Cohen Stuart, K. van der Voort Maarschalk, A. van der Padt, K. van't Reit, Influence of preadsorbed block copolymers on protein adsorption: Surface properties, layer thickness, and surface coverage, Langmuir 11 (1995) 3068-3074.

[164] S.W. Lee, H. Shang, R.T. Haasch, V. Petrova, G.U. Lee, Transport and functional behavior of poly(ethylene glycol)-modified nanoporous alumina membranes, Nanotechnology 16 (2005) 1335-1340.

[165] K. Rezwan, L.P. Meier, L.J. Gauckler, Lysozyme and bovine serum albumin adsorption on uncoated silica and AlOOH-coated silica particles: The influence of positively and negatively charged oxide surface coatings, Biomaterials 26 (2005) 4351-4357.

[166] N. Mugnier, J.A. Howell, M. Ruf, Optimisation of a back-flush sequence for zeolite microfiltration, Journal of Membrane Science 175 (2000) 149-161.

[167] Y.J. Zhao, J. Zhong, H. Li, N.P. Xu, J. Shi, Fouling and regeneration of ceramic microfiltration membranes in processing acid wastewater containing fine TiO_2 particles, Journal of Membrane Science 208 (2002) 331-341.

[168] M. Bartlett, M.R. Bird, J.A. Howell, An experimental-study for the development of a qualitative membrane cleaning model, Journal of Membrane Science 105 (1995) 147-157.

[169] M. Machida, K. Norimoto, T. Watanabe, K. Hashimoto, A. Fujishima, The effect of SiO_2 addition in super-hydrophilic property of TiO_2 photocatalyst, Journal of Materials Science 34 (1999) 2569-2574.

[170] X.T. Gao, I.E. Wachs, Titania-silica as catalysts: Molecular structural characteristics and physico-chemical properties, Catalysis Today 51 (1999) 233-254.

[171] T. Kataoka, J.A. Dumesic, Acidity of unsupported and silica-supported vanadia, molybdena, and titania as studied by pyridine adsorption, Journal of Catalysis 112 (1988) 66-79.

[172] K.S. Guan, B.J. Lu, Y.S. Yin, Enhanced effect and mechanism of SiO_2 addition in super-hydrophilic property of TiO_2 films, Surface & Coatings Technology 173 (2003) 219-223.

[173] P. Kubelka, F.Z. Munk, An article on optics of paint layers, Tech. Physik. 12 (1931) 593-604.

[174] H. Lin, C.P. Huang, W. Li, C. Ni, S.I. Shah, Y.H. Tseng, Size dependency of nanocrystalline TiO_2 on its optical property and photocatalytic reactivity exemplified by 2-chlorophenol, Applied Catalysis B-Environmental 68 (2006) 1-11.

[175] J. Aguado, R. van Grieken, M.J. Lopez-Munoz, J. Marugan, A comprehensive study of the synthesis, characterization and activity of TiO_2 and mixed TiO_2/SiO_2 photocatalysts, Applied Catalysis A-General 312 (2006) 202-212.

[176] J.C. Yu, X.C. Wang, X.Z. Fu, Pore-wall chemistry and photocatalytic activity of mesoporous titania molecular sieve films, Chemistry of Materials 16 (2004) 1523-1530.

[177] R. Asahi, T. Morikawa, T. Ohwaki, K. Aoki, Y. Taga, Visible-light photocatalysis in nitrogen-doped titanium oxides, Science 293 (2001) 269-271.

[178] Y. Zhao, C.Z. Li, X.H. Liu, F. Gu, H.B. Jiang, W. Shao, L. Zhang, Y. He, Synthesis and optical properties of TiO_2 nanoparticles, Materials Letters 61 (2007) 79-83.

[179] D.M. King, X.H. Du, A.S. Cavanagh, A. Weimer, Quantum confinement in amorphous TiO_2 films studied via atomic layer deposition, Nanotechnology 19 (2008).

[180] A.M. Peiro, J. Peral, C. Domingo, X. Domenech, J.A. Ayllon, Low-temperature deposition of TiO_2 thin films with photocatalytic activity from colloidal anatase aqueous solutions, Chemistry of Materials 13 (2001) 2567-2573.

[181] H. Choi, E. Stathatos, D.D. Dionysiou, Sol-gel preparation of mesoporous photocatalytic TiO_2 films and TiO_2/Al_2O_3 composite membranes for environmental applications, Applied Catalysis B-Environmental 63 (2006) 60-67.

[182] K. Kato, A. Tsuzuki, H. Taoda, Y. Torii, T. Kato, Y. Butsugan, Crystal-structures of TiO_2 thin coatings prepared from the alkoxide solution via the dip-coating technique affecting the photocatalytic decomposition of aqueous acetic-acid, Journal of Materials Science 29 (1994) 5911-5915.

[183] M. Bockmeyer, P. Lobmann, Crack formation in TiO_2 films prepared by sol-gel processing: Quantification and characterization, Thin Solid Films 515 (2007) 5212-5219.

[184] H.J. Nam, T. Amemiya, M. Murabayashi, K. Toh, Photocatalytic activity of sol-gel TiO_2 thin films on various kinds of glass substrates: The effects of Na+ and primary particle size, Journal of Physical Chemistry B 108 (2004) 8254-8259.

[185] K. Eufinger, D. Poelman, H. Poelman, R. De Gryse, G.B. Marin, Photocatalytic activity of dc magnetron sputter deposited amorphous TiO_2 thin films, Applied Surface Science 254 (2007) 148-152.

[186] S. Sircar, M.B. Rao, C.M.A. Thaeron, Selective surface flow membrane for gas separation, Separation Science and Technology 34 (1999) 2081-2093.

[187] G.S. Armatas, M.G. Kanatzidis, Mesoporous germanium-rich chalcogenido frameworks with highly polarizable surfaces and relevance to gas separation, Nature Materials 8 (2009) 217-222.

[188] K. Shimizu, H. Imai, H. Hirashima, K. Tsukuma, Low-temperature synthesis of anatase thin films on glass and organic substrates by direct deposition from aqueous solutions, Thin Solid Films 351 (1999) 220-224.

[189] S.F. Li, G.L. Ye, G.Q. Chen, Low-temperature preparation and characterization of nanocrystalline anatase TiO_2, Journal of Physical Chemistry C 113 (2009) 4031-4037.

[190] D. Jiang, Y. Xu, B. Hou, D. Wu, Y.H. Sun, A simple non-aqueous route to anatase TiO_2, European Journal of Inorganic Chemistry (2008) 1236-1240.

[191] H.M. Liu, W.S. Yang, Y. Ma, Y. Cao, J.N. Yao, J. Zhang, T.D. Hu, Synthesis and characterization of titania prepared by using a photoassisted sol-gel method, Langmuir 19 (2003) 3001-3005.

[192] J.G. Yu, G.H. Wang, B. Cheng, M.H. Zhou, Effects of hydrothermal temperature and time on the photocatalytic activity and microstructures of bimodal mesoporous TiO_2 powders, Applied Catalysis B-Environmental 69 (2007) 171-180.

[193] G. Wang, Hydrothermal synthesis and photocatalytic activity of nanocrystalline TiO_2 powders in ethanol-water mixed solutions, Journal of Molecular Catalysis A-Chemical 274 (2007) 185-191.

[194] K. Yanagisawa, J. Ovenstone, Crystallization of anatase from amorphous titania using the hydrothermal technique: Effects of starting material and temperature, Journal of Physical Chemistry B 103 (1999) 7781-7787.

[195] H. Imai, H. Morimoto, A. Tominaga, H. Hirashima, Structural changes in sol-gel derived SiO_2 and TiO_2 films by exposure to water vapor, Journal of Sol-Gel Science and Technology 10 (1997) 45-54.

[196] Z.S. Guan, X.T. Zhang, Y. Ma, Y.A. Cao, J.N. Yao, Photocatalytic activity of TiO_2 prepared at low temperature by a photo-assisted sol-gel method, Journal of Materials Research 16 (2001) 907-909.

[197] E.R. Gilliland, R.F. Baddour, J.L. Russell, Rates of flow through microporous solids, AIChE Journal 4 (1958) 90-96.

[198] Y.D. Chen, R.T. Yang, Surface-diffusion of multilayer adsorbed species, AIChE Journal 39 (1993) 599-606.

APPENDIX A

A GAS TRANSPORT MODEL FOR ACTIVE-SUPPORT LAYERS

In general, porous membranes have double layers that consist of active and support layers, as shown in Fig. A-1. Thus, a gas transport model for double-layered membrane has been developed based on a resistance in series model.

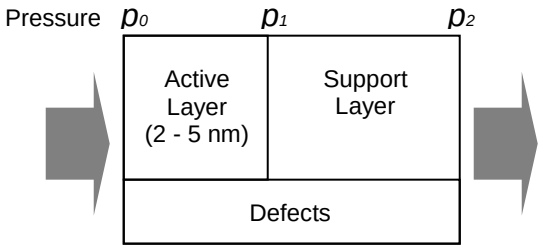

Fig. A-1. Schematic of gas permeation model for double-layered membrane.

In this model, the total permeance (P_T) may be given as the sum of the permeance through the membrane (active + support layer) (P_m) and defects (P_d), as described in chapter IV:

$$P_T = (1-\alpha)P_m + \alpha P_d \tag{4-2}$$

where α is the defect ratio (defect area/membrane area).

Gas transport through pores can occur by viscous flow, Knudsen diffusion, and surface diffusion, but in this model surface diffusion is not considered since it depends

on adsorption isotherm of a gas. Then permeance of a gas in a layer may be given by Eq. (4-1):

$$P_m = s_1\left(\frac{4}{3}\right)\left(\frac{\varepsilon}{\tau}\right)\frac{r}{l}\sqrt{\frac{8}{\pi RT}}\frac{1}{\sqrt{M}} + \frac{1}{s_2}\left(\frac{\varepsilon}{\tau}\right)\left(\frac{r^2}{RTl}\right)\frac{1}{\eta} < p >= \frac{K}{\sqrt{M}} + \frac{B}{\eta} < p > \quad (4\text{-}1)$$

where ε is the porosity, τ is the tortuosity, r is the mean hydraulic pore radius, l is the thickness, M is the molecular weight of a gas, η is the gas viscosity, $<p>$ is the mean pressure inside the membrane, and s_1 and s_2 are the shape factors.

The support layer and defects have both Knudsen and viscous contributions while the active layer can be reasonably assumed to have only Knudsen diffusion contribution due to its small pore sizes. Thus the fluxes in active layer (J_1), support layer (J_2), and defects (J_d) may be given by Eqs. (A-1), (A-2), and (A-3):

$$J_1 = \frac{K_1}{\sqrt{M}}\Delta p_1 \quad (A\text{-}1)$$

$$J_2 = \left[\frac{K_2}{\sqrt{M}} + \frac{B_2}{\eta} < p >\right]\Delta p_2 \quad (A\text{-}2)$$

$$J_d = \left[\frac{K_d}{\sqrt{M}} + \frac{B_d}{\eta} < p >\right]\Delta p \quad (A\text{-}3)$$

where $\Delta p_1 = p_0 - p_1$, $\Delta p_2 = p_1 - p_2$, and $\Delta p = \Delta p_1 + \Delta p_2 = p_0 - p_2$.

If the membrane has tubular morphology, the flux through each layer is not constant and may be corrected by considering the difference of the surface area between the layers:

$$J_m = J_1 \frac{d_{\ln 1}}{d_{\ln}} = J_2 \frac{d_{\ln 2}}{d_{\ln}} \tag{A-4}$$

where d_{ln}, d_{ln1}, and d_{ln2} are logarithmic mean diameters of the membrane layers.

The pressure at the interface between active and support layers (p_1) can be calculated using Eqs. (A-1), (A-2), and (A-4), to give Eq. (A-5):

$$p_1 = \frac{\sqrt{\left(\left(\frac{d_{\ln 1}}{d_{\ln 2}}\right)K_1 + K_2\right)^2 + 2B_2\left(\frac{\sqrt{M}}{\eta}\right)C} - \left(\left(\frac{d_{\ln 1}}{d_{\ln 2}}\right)K_1 + K_2\right)}{B_2\left(\frac{\sqrt{M}}{\eta}\right)} \tag{A-5}$$

where $C = \left(\frac{d_{\ln 1}}{d_{\ln 2}}\right)K_1 p_0 + K_2 p_2 + \frac{B_2}{2}\left(\frac{\sqrt{M}}{\eta}\right)p_2^2$. Eq. (A-5) shows the dependency of p_1 on the molecular weight and the viscosity of a gas, which implies that Δp_1 and Δp_2 will vary depending on the gas species.

Now, the permeance through the active and the support layers is given by Eq. (A-6), and finally the total permeance can be modeled using Eq. (4-2):

$$P_m = \frac{J_m}{\Delta p} = \left(\frac{d_{\ln 1}}{d_{\ln}}\right)\frac{J_1}{\Delta p} = \left(\frac{d_{\ln 1}}{d_{\ln}}\right)\frac{K_1}{\sqrt{M}}\left[\frac{\Delta p_1}{\Delta p}\right] \tag{A-6}$$

APPENDIX B

A SURFACE DIFFUSION MODEL FOR PROPANE THROUGH POLYDISPERSE PORES

A simple surface diffusion model has been developed for propane transport through the Gn-C12 membranes. This model was derived based on a work of Gilliland et al. [197], where it was assumed that the highly adsorbable gases form the films on the surface and that the transport of these adsorbed films are subject to the spreading pressure and the shear stress between the surface and the flowing films. Then, Eq. (B-1) is obtained for the surface diffusion coefficient in this case, which is different from the Darken's equation (Eq. (1-10)):

$$D_s = D_c q \frac{d \ln p}{d \ln q} \tag{B-1}$$

where D_s is the Fickian surface diffusivity, D_c is the corrected diffusivity, q is the amount of gas adsorbed per unit sorbent, and p is the pressure. The term $d \ln p/d \ln q$ can be obtained from the adsorption isotherm.

The BET and Langmuir adsorption isotherms are commonly used for surface diffusion modeling [20, 198]. In fact, the Langmuir isotherm that assumes the monolayer adsorption can be extended to the BET isotherm when a multilayer adsorption is considered. Thus the membranes that have a broad pore size distribution may have both of the isotherms depending on the pore sizes and the adsorbate species.

For example, diverse surface diffusion mechanisms may be exerted, caused by the difference in organic loading and pore sizes in dendrimer attached membranes, as shown in Fig. B-1.

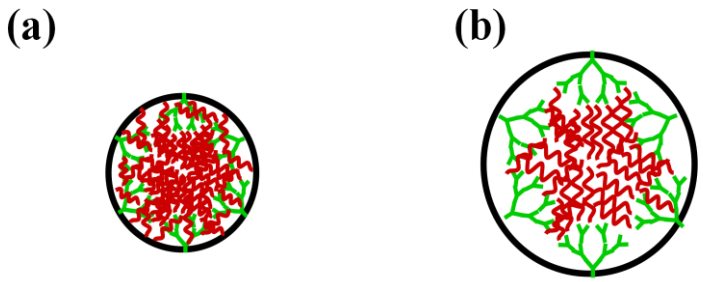

Fig. B-1. (a) Densely and (b) loosely packed pores of dendrimer-C12 membrane.

Thus, if both of the isotherms are considered in Eq. (B-1), the flux by surface diffusion is:

$$J_s = -D_s \frac{dq}{dz} = -(1-\varepsilon_o) D_c \left[q_1 \frac{d \ln p_1}{d \ln q_1} \frac{dq_1}{dz} + q_2 \frac{d \ln p_2}{d \ln q_2} \frac{dq_2}{dz} \right]$$
$$= -(1-\varepsilon_o) D_c \left[\left(\frac{q_1^2}{p_1} \right) \frac{dp_1}{dz} + \left(\frac{q_2^2}{p_2} \right) \frac{dp_2}{dz} \right] \quad \text{(B-2)}$$

$$\frac{q_1}{q_{s1}} = \frac{Kp_1}{1+Kp_1} \quad \text{(B-3)}$$

$$\frac{q_2}{q_{s2}} = \frac{cx}{(1-x)(1+(c-1)x)}, \quad \left(x = \frac{p_2}{p_s} \right) \quad \text{(B-4)}$$

where ε_0 is the porosity, K is the Langmuir sorption constant, c is the BET constant, q_s is the total amount adsorbed in monolayer at saturation, and p_s is the saturation pressure. If q_1 (Langmuir) and q_2 (BET) in Eq. (B-2) are substituted from Eqs. (B-3) and (B-4):

$$J_s = -(1-\varepsilon_o)D_c\left[q_{1s}^2\left(\frac{K^2 p_1}{(1+Kp_1)^2}\right)\frac{dp_1}{dz} + q_{s2}^2\left(\frac{c^2 x}{(1-x)^2(1+(c-1)x)^2}\right)\frac{dx}{dz}\right] \quad \text{(B-5)}$$

Then, the permeance by surface diffusion is given by:

$$P_s = A\left[\alpha^2 L_K(p) + (1-\alpha)^2 B_c(x)\right] \quad \text{(B-6)}$$

where $A = (1-\varepsilon_o)\dfrac{D_c q_s^2}{L}$,

$$L_K(p) = \ln\left(\frac{1+Kp_o}{1+Kp_L}\right)\Big/\Delta p - \frac{K}{(1+Kp_0)(1+Kp_L)}, \text{ and}$$

$$B_c(x) = \left[\frac{c-2}{c}\ln\left(\frac{(1-x_L)(1+(c-1)x_o)}{(1+(c-1)x_L)(1-x_o)}\right) - \left(\frac{2+(c-2)x_L}{(1-x_L)(1+(c-1)x_L)} - \frac{2+(c-2)x_o}{(1-x_o)(1+(c-1)x_o)}\right)\right]\Big/\Delta p$$

where α is q_{1s}/q_s, p_0 is the feed pressure, p_L is the permeate pressure, and x_0 and x_L are p/p_s at the feed and the permeate side, respectively.

Figs. B-2, B-3, and B-4 show the modeling results how the permeance changes with the parameters. As α changes from 0 to 1, the contribution of the Langmuir adsorption to the permeance increases.

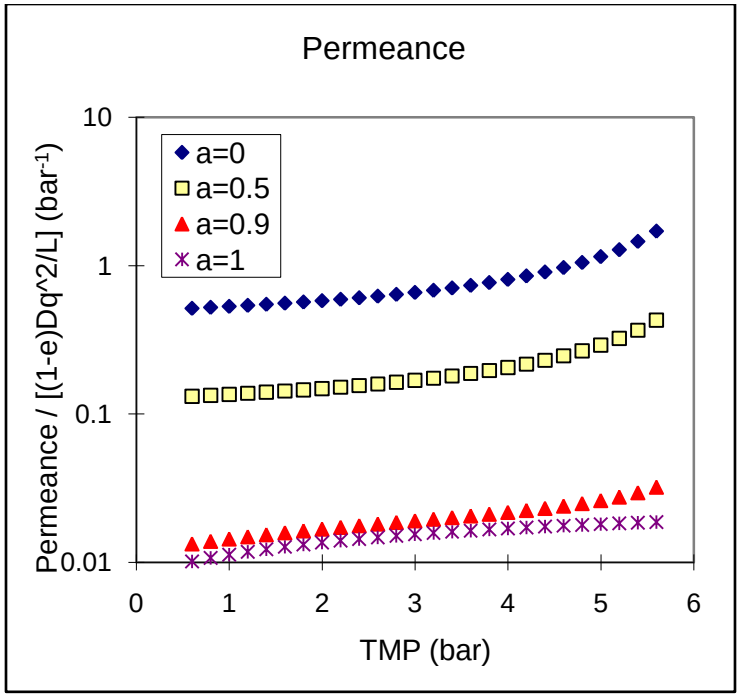

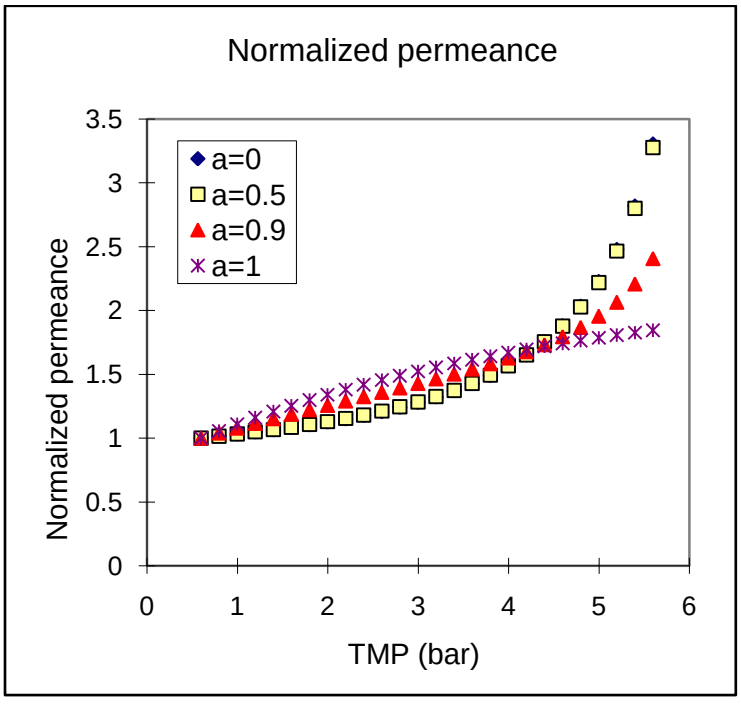

Fig. B-2. Modeling results when K = 0.1 bar^{-1} and c = 10.

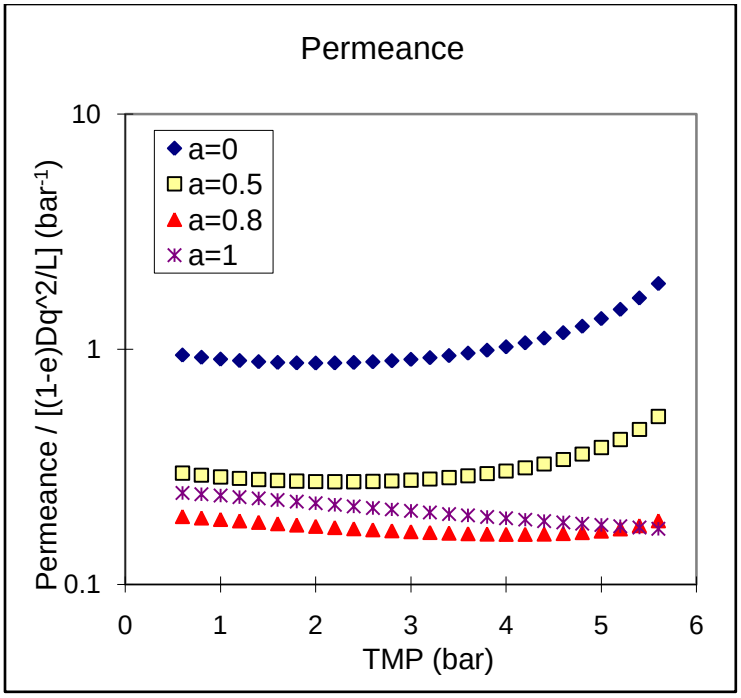

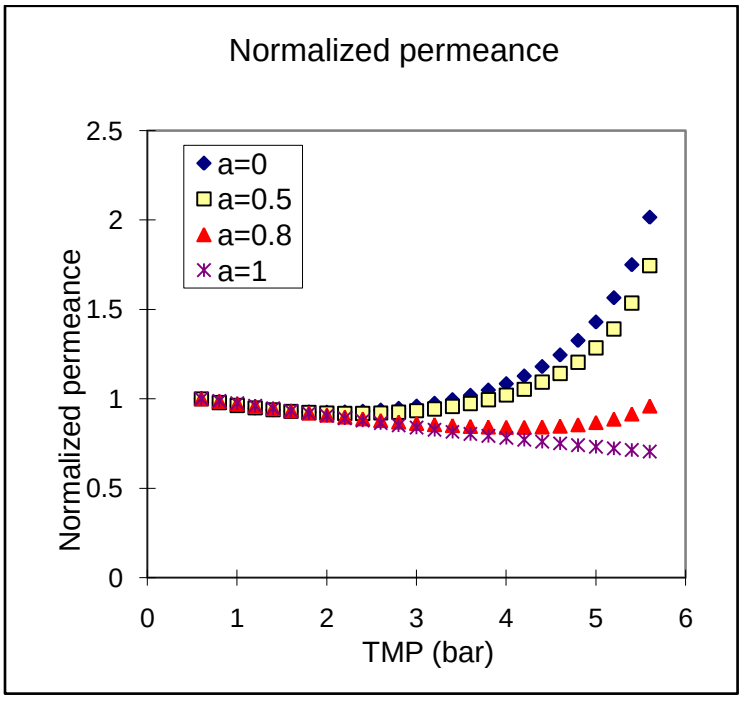

Fig. B-3. Modeling results when K = 1 bar^{-1} and c = 50.

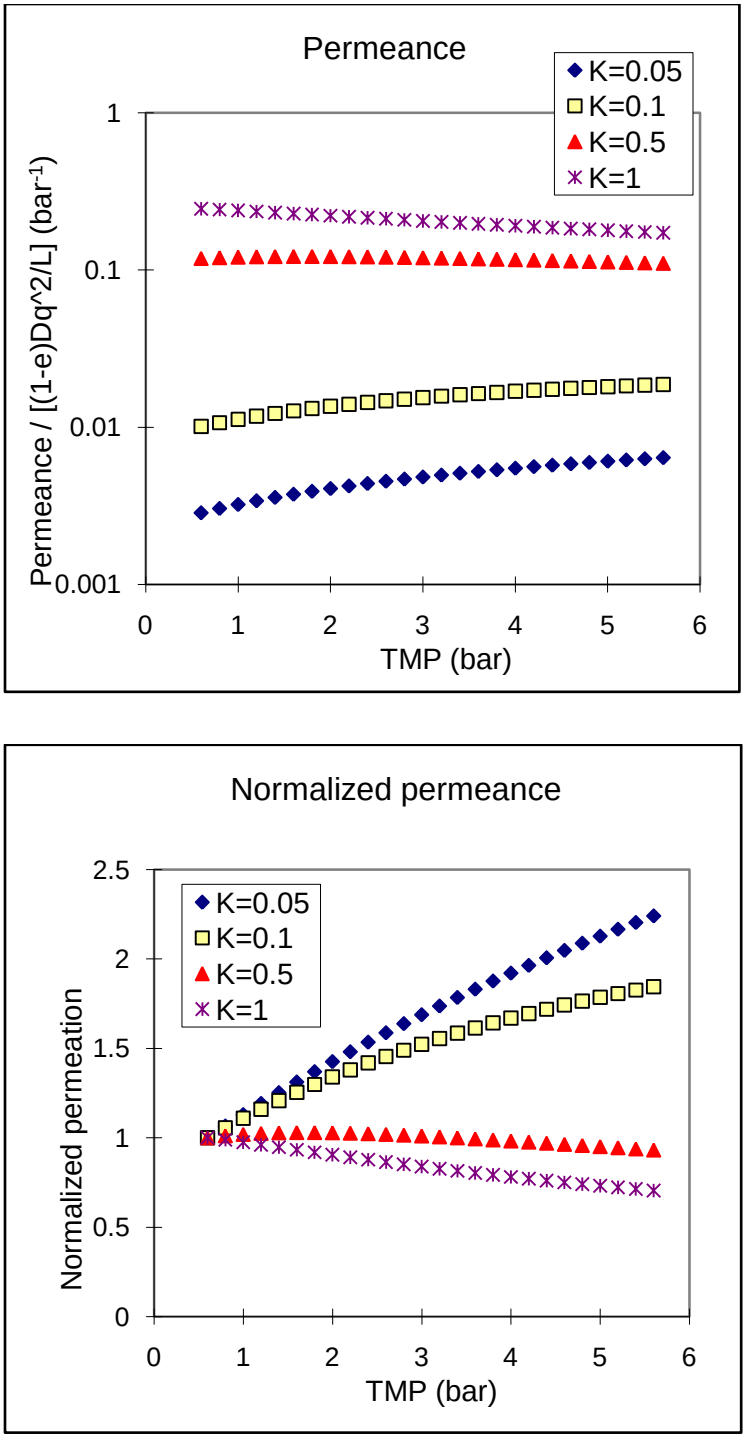

Fig. B-4. Modeling results when α = 1 (Langmuir isotherm only).

VITA

Seung Uk Yeu was born in Seoul, Korea. He received his B.S. and M.S. in Chemical Technology (currently Department of Chemical and Biological Engineering) from Seoul National University, Seoul, Korea in 1994 and in 1996, respectively. After graduation, he worked for LG Chem for eight years as a researcher. In 2004, he joined Texas A&M University to complete his doctoral studies and received his Ph.D. in Chemical Engineering in August 2009.

He can be contacted at:

LG Chem Research Park
#104-1 Munji-dong, Yuseong-gu
Daejeon 305-380
South Korea
e-mail: swyeob@lgchem.com